Nuclear equation of state at finite temperature and proton fraction based on chiral effective field theory

Nukleare Zustandsgleichung bei endlicher Temperatur und Proton-Anteil basierend auf chiraler effektiver Feldtheorie

Zur Erlangung des Grades eines Doktors der Naturwissenschaften (Dr.rer.nat.)
Dissertation von Jonas Keller
Tag der Einreichung: 16.10.2023, Tag der Prüfung: 27.11.2023

1. Gutachten: Prof. Achim Schwenk, Ph.D.
2. Gutachten: Prof. Dr. Almudena Arcones

Technische Universität Darmstadt
Fachbereich Physik
Institut für Kernphysik

Darmstadt 2023

Nuclear equation of state at finite temperature and proton fraction based on chiral effective field theory

Nukleare Zustandsgleichung bei endlicher Temperatur und Proton-Anteil basierend auf chiraler effektiver Feldtheorie

Doctoral thesis by Jonas Keller

Date of submission: 16.10.2023
Date of thesis defense: 27.11.2023
Publication on TUprints: 2024
URN: urn:nbn:de:tuda-tuprints-282026

Darmstadt, Technische Universität Darmstadt

Abstract

This thesis investigates the nuclear equation of state (EOS) using interactions among neutrons and protons based on chiral effective field theory (EFT). While nuclear matter is well studied microscopically at zero temperature for pure neutron matter and symmetric nuclear matter (with equal amounts of neutrons and protons), the general case is less explored. We present many-body calculations of the EOS for arbitrary temperatures and arbitrary neutron-proton asymmetries.

We first give a general overview of nuclear interactions and then introduce many-body perturbation theory (MBPT) as the method used in this thesis to determine the EOS, e.g., the pressure as function of the energy density, temperature, and proton fraction, from chiral two- and three-nucleon interactions up to next-to-next-to-next-to-leading order. Furthermore, we introduce Gaussian processes as a tool to interpolate calculated EOS data points and to determine thermodynamic derivatives.

As a starting point we calculate the EOS of neutron matter at finite temperatures with a particular focus on understanding thermal effects. The impact of nuclear interactions is studied systematically by considering different chiral two- and three-nucleon interactions. We then generalize these results to arbitrary proton fraction. For astrophysical applications the composition and pressure in beta equilibrium is determined based on the full asymmetry dependence of the EOS. Moreover, we explore the speed of sound and symmetry energy at finite temperature. For all results, theoretical uncertainty estimates based on the EFT expansion are provided.

Three further applications of these new calculations are presented. We determine the liquid-gas phase transition of symmetric nuclear matter and provide the critical temperature and density together with the phase diagram. Second, the phase coexistence at low proton concentrations is investigated at zero temperature with a focus on the possibility of proton drip. Finally, we explore the impact of muons on the composition in beta equilibrium and provide results for the speed of sound together with EFT and MBPT uncertainty estimates.

Zusammenfassung

Diese Thesis untersucht die nukleare Zustandsgleichung (EOS), wobei die Wechselwirkungen zwischen Neutronen und Protonen auf chiraler effektiver Feldtheorie (EFT) basieren. Obwohl Kernmaterie bei verschwindender Temperature und für reine Neutronenmaterie oder symmetrische Materie (mit gleicher Menge von Neutronen und Protonen) mikroskopisch gut untersucht wurde, ist der allgemeine Fall weniger erforscht. Wir zeigen Vielteilchenrechnungen der EOS für beliebige Temperaturen und beliebige Neutron-Proton-Asymmetrien.

Zuerst geben wir einen Überblick über die nuklearen Wechselwirkungen und führen dann Vielteilchenströrungstheorie (MBPT) als die Methode ein, die zur bestimmung der EOS, z.B. Druck als Funktion der Energiedichte, Temperature und Protonanteil, in dieser Thesis auf Basis von chiralen Zwei- und Dreikernwechselwirkungen bei next-to-next-to-next-to-leading order verwendet wird. Weiterhin stellen wir Gauß-Prozesse vor, die zum interpolieren von berechneten EOS Datenpunkten und zum bestimmen von thermodynamischen Ableitungen verwendet werden können.

Als erstes berechnen wir die EOS von Neutronenmaterie bei endlichen Temperaturen mit dem Schwepunkt thermische Effekte zu verstehen. Der Einfluss der Kernwechselwirkungen wird durch verwenden verschiedener chiraler Zwei- und Dreikernwechselwirkungen systematisch untersucht. Diese Ergebnisse werden dann für beliebige Protonenanteile verallgemeinert. Für astrophysikalische Anwendungen wird die Zusammensetzungen und der Druck im Beta-Gleichgewicht, basierend auf der vollen Asymmetrieabhängigkeit der EOS, bestimmt. Weiterhin erforschen wir die Schallgeschwindigkeit und Symmetrieenergie bei endlichen Temperaturen. Für alle Ergebnisse werden theoretische Ferhlerabschätzungen, basierend auf der EFT Entwicklung, angegeben.

Drei weitere Anwendungen dieser neuen Berechnungen werden vorgestellt. Wir bestimmen den Flüssigkeits-Gas Phasenübergang von symmetrischer Materie und geben die kritische Temperatur und kritische Dichte zusammen mit dem Phasendiagram an. Zweitens, untersuchen wir das Phasengleichgewicht bei niedrigen Protonanteilen bei verschwindender Temperatur, wobei ein Schwepunkt darauf liegt, ob Protondrip möglich ist. Schließlich untersuchen wir den Einfluss von Muonen auf die Zusammensetzung im Beta-Gleichgewicht und geben Ergebnisse für die Schallgeschwindigkeit zusammen mit EFT und MBPT Fehlerabschätzungen an.

Publications

Some results of this thesis have already been published in the following papers:

- J. Keller, C. Wellenhofer, K. Hebeler, and A. Schwenk, Phys. Rev. C **103**, 055806 (2021).
- J. Keller, K. Hebeler, and A. Schwenk, Phys. Rev. Lett. **130**, 072701 (2023).

The text and figures of these publications are contained in this thesis.

Contents

List of Figures

List of Tables

1 Introduction

1.1 Nuclear equation of state

Parts of this chapter have already been published in Ref. [1]. The nuclear equation of state (EOS) plays a central role for the physics of nuclei and dense matter in neutron stars, supernovae, and mergers [2–6]. The EOS governs the properties of matter through the relation of different thermodynamic state variables, e.g. pressure as function of energy density, temperature, and composition [7, 8]. For densities around nuclear saturation density $n_0 = 0.16\,\mathrm{fm}^{-3}$, the nuclear EOS investigated in this thesis, considers an idealized system that has neutrons and protons as degree of freedom in the thermodynamic limit. In particular there are no surface effects and no Coulomb interactions and thus no bound nuclei considered.

When working at fixed temperature, neutron density, and proton density the relevant thermodynamic potential is the Helmholtz free energy per particle (or volume)

$$\frac{F}{A}(T, n_n, n_p)\,, \tag{1.1}$$

where T is the temperature, n_n the neutron density, and n_p the proton density. Often it is more convenient to parameterize the EOS in terms of the total (baryonic) density $n = n_n + n_p$ and the proton fraction $x = n_p/n$. Therefore, we use

$$\frac{F}{A}(x, T, n)\,, \tag{1.2}$$

for the rest of this thesis. Other thermodynamic quantities can easily be derived from there, e.g., [7]

$$P = n^2 \frac{\partial}{\partial n}\frac{F}{A}\,, \tag{1.3}$$

$$\frac{S}{A} = -\frac{\partial}{\partial T}\frac{F}{A}\,, \tag{1.4}$$

$$\frac{E}{A} = \frac{F}{A} + T\frac{S}{A}\,, \tag{1.5}$$

$$\mu_i = \frac{F}{A} + n\frac{\partial}{\partial n}\frac{F}{A} + (\delta_{i,p} - x)\,\frac{\partial}{\partial x}\frac{F}{A}\,, \tag{1.6}$$

where P is the pressure, S/A the entropy per particle, E/A the internal energy per particle, and μ_i the chemical potential of neutrons ($i = n$) and protons ($i = p$). Figure 1.1 shows an overview of the EOS at $T = 0$ as a function of density and for various proton fractions. Note that at $T = 0$, the free energy and internal energy are identical, i.e., $F/A(x, T = 0, n) = E/A(x, T = 0, n)$, see

Eq. (1.5).

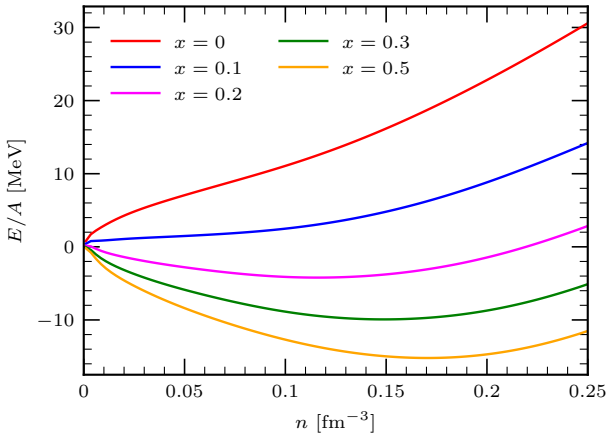

Figure 1.1: Overview of the $T = 0$ energy per particle as a functions of density. Different colors show different proton fractions from neutron matter $x = 0$ to symmetric nuclear matter $x = 0.5$. The lines are taken from the EOS based on chiral two- and three-nucleon interactions presented in Chapter 6.

Because of the approximate isospin symmetry of nuclear interactions, the EOS is often expanded in terms of the asymmetry parameter $\beta = (n_n - n_p)/(n_n + n_p) = 1 - 2x$ around a system with equally many neutrons and protons $x = 0.5$ [9]:

$$F(T, x, n) = a_0(T, n) + a_2(T, n)(1 - 2x)^2 + a_4(T, n)(1 - 2x)^4 + \dots , \tag{1.7}$$

where the coefficient functions $a_i(T, n)$ describe the asymmetry dependence. The expansion is typically truncated beyond the quadratic term (see e.g. Ref. [9]), such that the free energy can be written as

$$F(T, x, n) = F_{\mathrm{SNM}}(T, n) + F_{\mathrm{sym}}(T, n)(1 - 2x)^2 , \tag{1.8}$$

$$F_{\mathrm{sym}}(T, n) = F_{\mathrm{PNM}}(T, n) - F_{\mathrm{SNM}}(T, n) , \tag{1.9}$$

in terms of two special cases, pure neutron matter $F_{\mathrm{PNM}}(T, n)$ with $x = 0$ and symmetric nuclear matter $F_{\mathrm{SNM}}(T, n)$ with $x = 0.5$. Here $F_{\mathrm{sym}}(T, n)$ is the so called (free) symmetry energy. An analysis of the expansion and higher order contributions based on microscopic calculations can be found in Refs. [10, 11].

In this thesis we determine the EOS starting from nuclear interactions that are derived from chiral effective field theory as introduced in Chapter 2. From the Hamiltonian we calculate the EOS by using a perturbative expansion of the grand-canonical potential, see Chapter 3. The special case of pure neutron matter is considered in Chapter 5 and the general case for arbitrary proton fraction, without employing the approximation of Eq. (1.8), in Chapter 6.

1.2 Constraints on the nuclear EOS

Various experimental and theoretical constraints exist for the nuclear EOS. Here we only highlight two examples, further details can be found in, e.g., Refs. [12–14]. To characterize the zero-temperature nuclear EOS, it can be expanded around the empirical saturation density $n_0 = 0.16\,\mathrm{fm}^{-3}$ in terms of $\bar{n} = (n - n_0)/(3n_0)$ and in the asymmetry parameter $\beta = 1 - 2x$

$$\frac{E}{A}(n,x) = B + \frac{1}{2}K\bar{n}^2 + \left(S_v + L\bar{n} + \frac{1}{2}K_{\mathrm{sym}}\bar{n}^2\right)(1-2x)^2 + \dots\,, \tag{1.10}$$

where B is the binding energy, K the incompressibility, S_v the symmetry energy at saturation density, L the slope parameter, and K_{sym} the symmetry incompressibility [12, 15]. These parameters can be constrained experimentally and theoretically, see, e.g., Refs. [12, 15] for an overview. Figure 1.2 shows compilations of constraints on S_v and L from various experiments together with theoretical predictions. The microscopic calculations indicated by the regions H, G, and GP-B are consistent with experimental constraints.

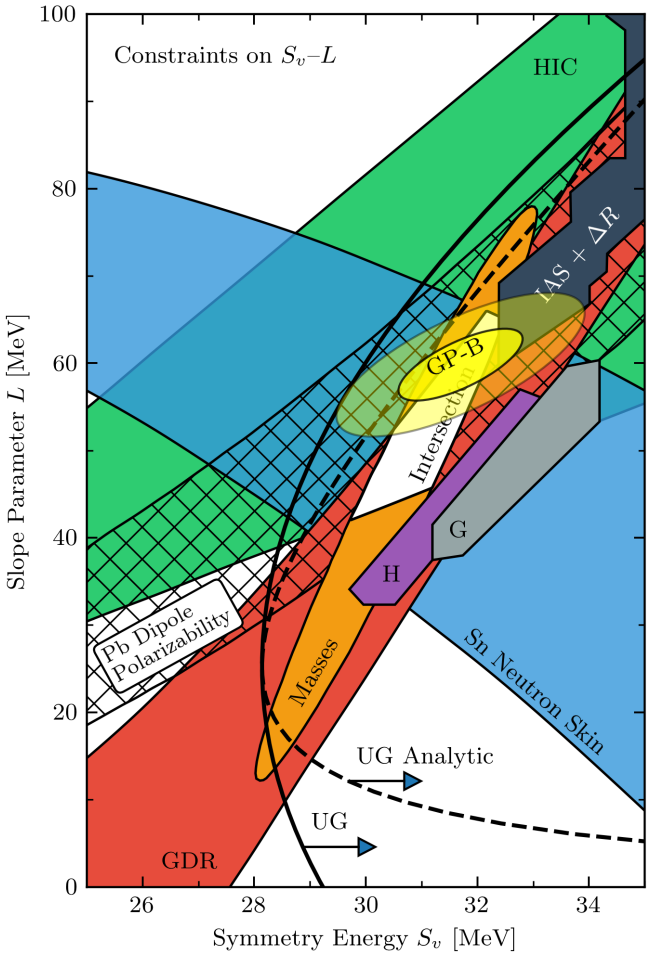

Figure 1.2: Various constraints on the slope parameter L and symmetry energy at saturation density S_v together with theoretical predictions (H, G, GP-B). Figure is taken from Ref. [16] (see also Ref. [2]).

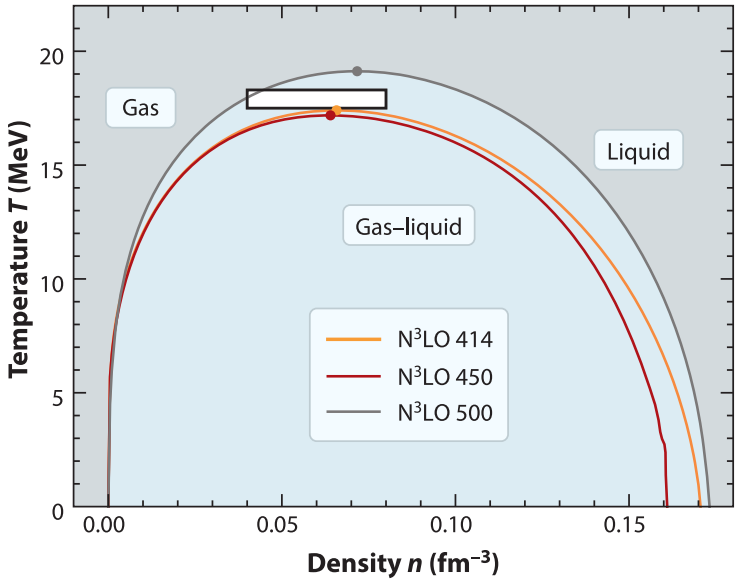

Figure 1.3: Phase coexistence boundaries of symmetric nuclear matter determined in Ref. [17]. Different lines show different interactions, points mark the critical temperature and density. The white box shows the empirically determined critical point. Figure taken from C. Drischler, J. W. Holt, and C. Wellenhofer Ref. [5] (https://doi.org/10.1146/annurev-nucl-102419-041903) under CC BY 4.0 (https://creativecommons.org/licenses/by/4.0/), modified. ©2021 by Annual Reviews.

Furthermore some constraints exist at finite temperatures for the nuclear EOS. For symmetric nuclear matter the EOS has a phase transition with a critical point (temperature and density) that can be determined experimentally. Figure 1.3 shows the calculated phase diagram from Ref. [17] based on different chiral interactions in comparison to the empirically determined critical point. The liquid-gas phase transition of symmetric nuclear matter is investigated in Chapter 7 of this thesis.

1.3 Neutron stars

For an introduction about neutron stars and relation to nuclear physics see, e.g., Refs. [6, 15, 18, 19]. We only give a short summary of topics that are important for this thesis. Figure 1.4 shows a schematic cross section of a neutron star. The following summary of the composition of neutron star matter is based on Refs. [18, 19]. At low densities the crust of the neutron star is given by bound nuclei and electrons. When the density is increased towards the center of the star, nuclei get more neutron rich and at some density neutrons start to drip out of bound nuclei (neutron drip). They form a gas that coexists with the bound nuclei. There is also the possibility that at some higher density protons start to drip out of bound nuclei as well (proton drip), such that matter is composed of bound nuclei, free neutrons and free protons. The possibility of neutron and proton drip will be investigated in this thesis in Chapter 8. At even higher densities nuclei dissolve, and matter is a uniform gas consisting of free neutrons, free protons, electrons, and

muons in beta equilibrium. Uniform matter in beta equilibrium (e.g., around $\sim 5\%$ protons at nuclear saturation density) will be explored in this thesis in Chapter 6 and 9.

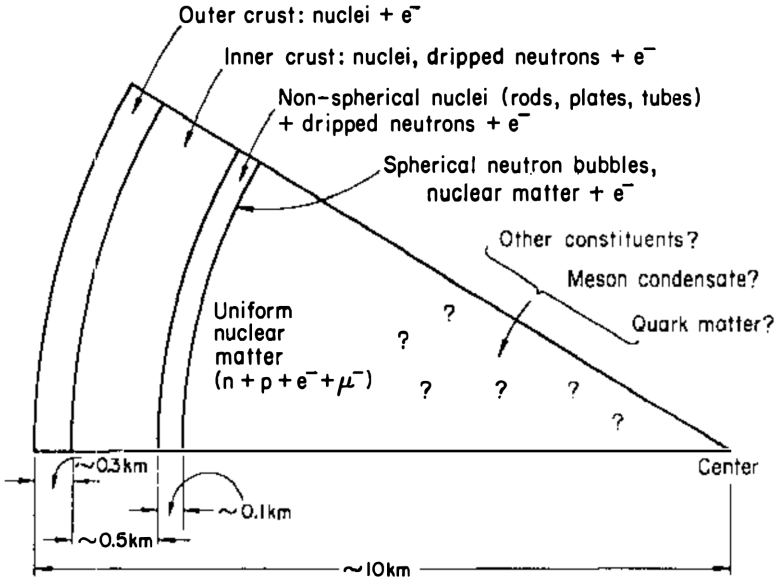

Figure 1.4: Schematic cross section of a neutron star from the outer crust (lowest density) to the core (highest density). Figure is taken from Ref. [19]. ©1995 by Annual Reviews.

The EOS for matter in beta equilibrium uniquely determines the relationship between mass and radius of a neutron star in equilibrium. The Tolman-Oppenheimer-Volkoff (TOV) equation [20, 21]

$$\frac{\mathrm{d}P(r)}{\mathrm{d}r} = -\frac{(\epsilon(r)+P(r))(M(r)+4\pi r^3 P(r)}{r(r-2M(r))}\,, \tag{1.11}$$

$$\frac{\mathrm{d}M(r)}{\mathrm{d}r} = 4\pi r^2 \epsilon(r)\,, \tag{1.12}$$

can be solved to obtain the mass as function of radius $M(R)$. Here $P(r)$ is the pressure and $M(r)$ the enclosed gravitational mass as a function of the current radius. Following, e.g., Ref. [15], starting from the center $r = 0$ with a central pressure $P(0) = P_c$ and mass $M(0) = 0$, the equations can be integrated to larger radii until the pressure at the boundary of the star vanishes. The neutron star radius R is then given by $P(R) = 0$ and the gravitational mass by $M = 4\pi \int_0^R \mathrm{d}r r^2 \epsilon(r)$. By changing the central pressure a mass radius curve can be obtained.

A crucial input to solve the TOV equations is the high-density EOS, e.g., pressure as a function of energy density. Microscopic calculations of the EOS based on nuclear interactions are only reliable up to about $n \lesssim 2n_0$ [5]. However, knowledge of the EOS up to higher densities is necessary for a solution of the TOV equations, e.g., up to $n_{\max} = 8.3 n_0$ in Ref. [22].

The strategy employed by Ref. [22] is to combine the nuclear EOS based on microscopic matter calculations with a high-density extension. The left part of Fig. 1.5 shows this construction for the pressure as a function of energy density. Matter calculations from chiral EFT at nuclear densities are shown as the dark blue band on the left together with a piecewise polytrope extension to

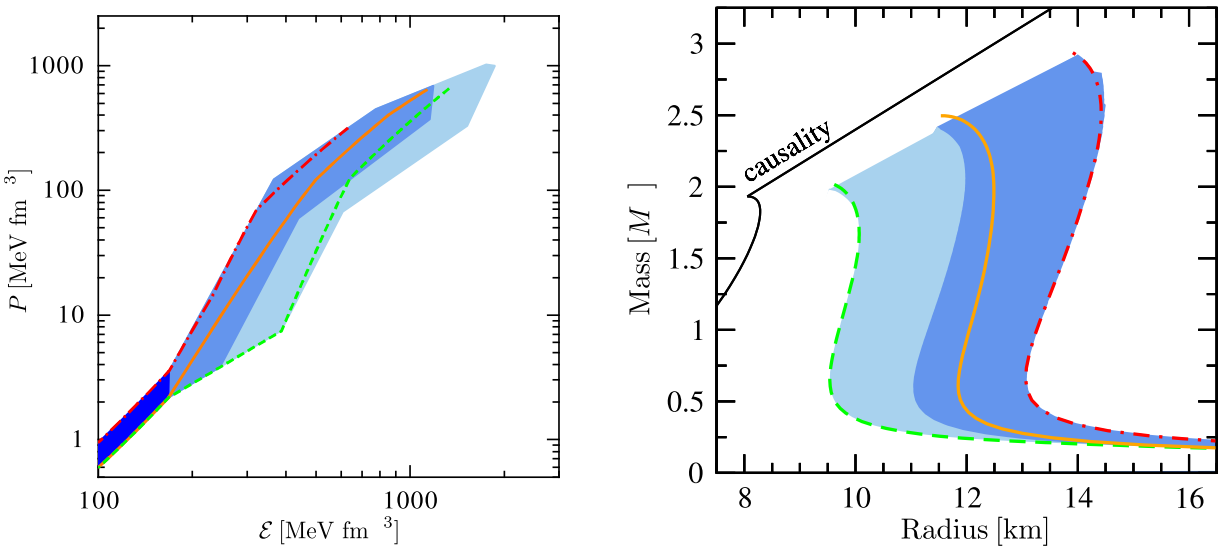

Figure 1.5: Pressure as function of energy density (left) and resulting neutron star mass-radius relation constraints (right). See text for details. Figure is taken from Ref. [22]. ©2013 by The American Astronomical Society.

higher densities (see Ref. [22] for details). The high-density extension is constrained by causality (speed of sound is smaller than speed of light) and the ability to reproduce the most massive neutron star observation, e.g., $M_{\max} \sim 2M_{\odot}$ where $M_{\odot}$ is the mass of our sun [22]. The resulting constraints on the mass-radius relation, as determined from the TOV equations, are shown in the right plot of Fig. 1.5. Three representative EOS and the resulting mass-radius relations are shown as colored lines (see Ref. [22] for details). These calculations can be combined with measurements of neutron star observables to further constrain the EOS and neutron star properties, see, e.g., Refs. [22–33] for calculations where chiral EFT has been used to determine the nuclear EOS.

1.4 Core-collapse supernova explosions and neutron star mergers

The solution of the hydrodynamic equations in astrophysical simulations, e.g., for core-collapse supernovae or neutron star mergers, requires the high-density EOS as a crucial input [12, 34]. In contrast to the determination of the mass-radius relation in the previous section, these simulations require the EOS for finite temperatures and proton fractions.

Figure 1.6 shows the matter composition in spherical core-collapse supernova simulations of Ref. [35]. From there it is evident, that temperatures up to about 100 MeV and proton fractions from about 0.1 to slightly above 0.5 are needed to evolve the simulations. The impact of thermal interaction effects (e.g., the temperature dependence of the pressure) has been studied recently by, e.g., Ref. [36] in core-collapse supernovae and in Ref. [37] for neutron star mergers. Ref. [36] includes thermal interaction effects in the EOS by means of a density-dependent effective nucleon mass and explored the impact in spherically-symmetric core-collapse supernova simulations. The contraction behavior of the proto-neutron star (PNS) and the shock propagation of these simulations are shown in Fig. 1.7. Different lines show different EOS with different

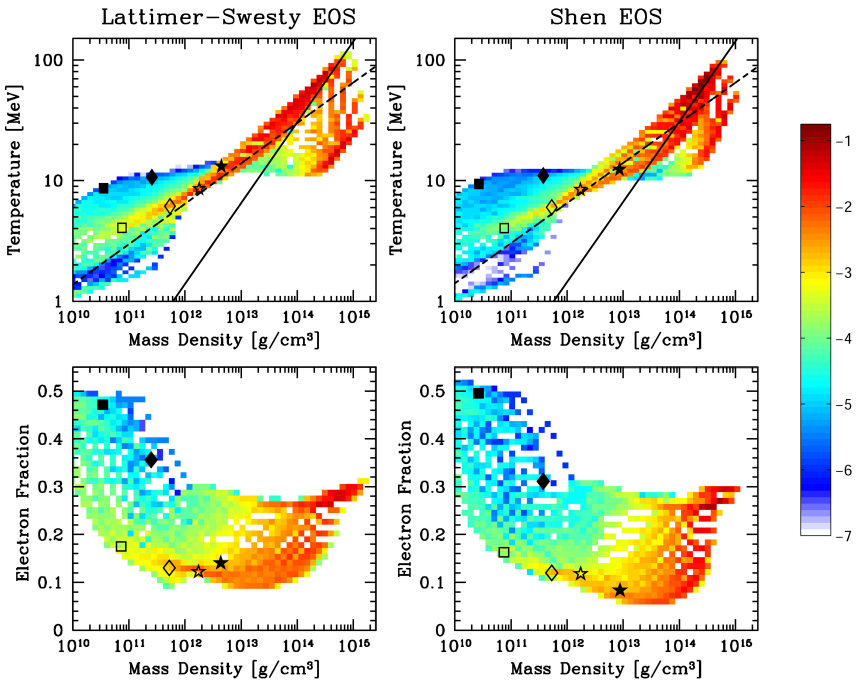

Figure 1.6: Matter distribution of a spherical-symmetric CCSN simulation from Ref. [35] for the Lattimer-Swesty EOS (left) and Shen EOS (right). The colors of each bin encode the mass and time weighted occurrence of the corresponding density and temperature, see Ref. [35]. Figure is taken from Ref. [35]. ©2012 by The American Astronomical Society.

thermal approximations. One can observe a strong impact of the EOS on the PNS contraction and shock propagation. Thermal interaction effects in neutron matter are studied in Chapter 5 of this thesis.

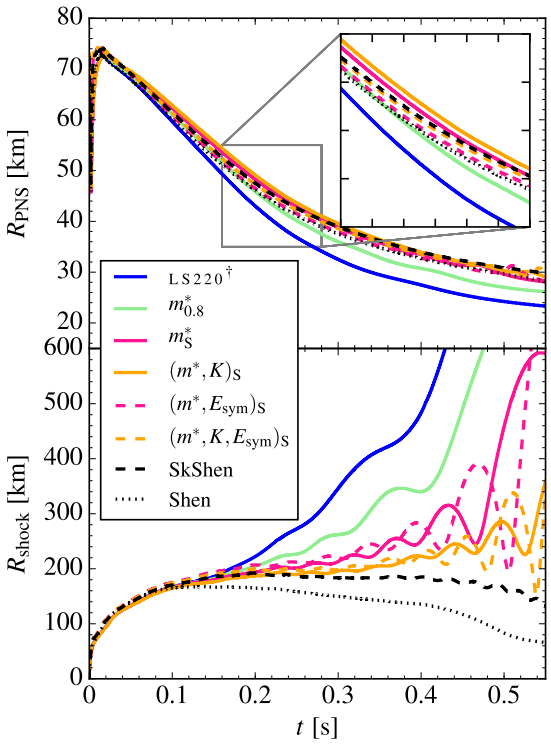

Figure 1.7: Proto-neutron star contraction (upper panel) and shock radius (lower panel) as a function of time from the spherically-symmetric core-collapse supernova simulations of Ref. [36]. Different lines correspond to different EOS employed in the simulations. Figure is taken from Ref. [36]. ©2020 by American Physical Society.

1.5 Overview of this thesis

The structure of this thesis is shown in Fig. 1.8. In Chapter 2 we introduce the nuclear interactions used in the thesis, they are the basis for constructing the Hamiltonians used in the many-body calculations. Chapter 3 introduces many-body perturbation theory to determine thermodynamic properties from the Hamiltonian. An expansion for the grand-canonical potential is presented and it is discussed how an expansion for the free energy can be derived from there. Next in Chapter 4, Gaussian processes are introduced to interpolate EOS data points and to determine thermodynamic derivatives from the free energy. In the rest of the thesis various applications of this framework are presented. Chapter 5 presents calculations of neutron matter at finite temperatures. These are generalized to asymmetric matter in Chapter 6. Chapter 7 shows an analysis of the liquid-gas phase transition of symmetric nuclear matter. In Chapter 8 we investigate phase coexistence at low proton concentration at zero temperature. Finally in Chapter 9 we extend calculations of matter in beta equilibrium to include muons as a degree of freedom.

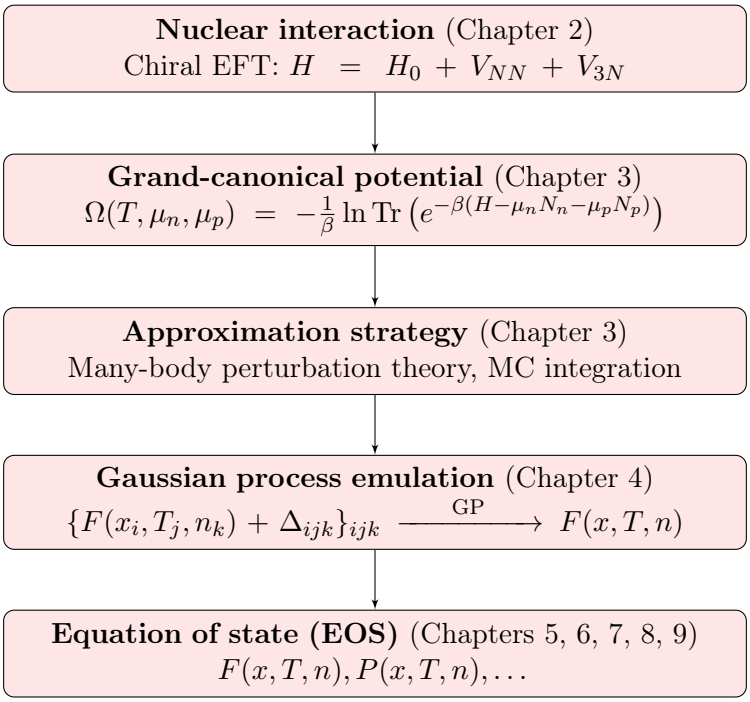

Figure 1.8: Overview of this thesis.

2 Nuclear interactions

As introduced in the previous section, neutrons and protons are important degrees of freedom for astrophysical applications. Knowledge about the interactions of these particles is the starting point for theoretical calculations of the EOS and related quantities.

From the standard model it is known that nucleons (neutrons and protons) are no fundamental particles. They consist of three quarks (up-down-down for neutrons and up-up-down for protons) and the interactions among nucleons is the residual strong interaction of the confined quarks. However, a direct calculations of the EOS based on the quantum chromodynamics (QCD), the theory describing the interaction among quaks, is infeasible, except at very high densities, see, e.g., Refs. [38, 39].

Instead we here take a different approach. Our degrees of freedom will be nucleons (not quarks and gluons) and the interaction among them is described by an effective field theory (EFT) for QCD at low energies which in our case is chiral effective field theory [40–42]. It provides an expansion of nuclear interactions at low energies with the ability to quantify uncertainties of the expansion. One consequence of neglecting the internal structure of the nucleons is the emergence of many-body interactions (that cannot be expressed as a sum of interactions between two nucleons) [40–42]. The most important of those, three-nucleon interactions (known to be important for observables of atomic nuclei and nuclear matter [3, 43, 44]), are included in the calculations in this thesis.

2.1 Chiral effective field theory

The nucleonic interactions considered in this thesis are derived from chiral effective field theory [40–42]. A detailed introduction can be found in Refs. [40–42]. We only give an overview about topics that are important for this thesis. This section is based on Ref. [41].

The degrees of freedoms in chiral EFT are nucleons and pions. The interactions are given by contact interactions (short range) and pion exchanges (long range). To deal with the infinite number of interaction terms that arise, a scheme has to be chosen that orders them by their importance. In chiral EFT this so called power counting orders the terms by powers of their momentum dependence

$$Q = \frac{p}{\Lambda_b}\,, \tag{2.1}$$

where p is a generic momentum and Λ_b is the breakdown scale of the EFT. This is shown in Fig. 2.1. The interaction terms are shown as diagrams and are ordered by their momentum

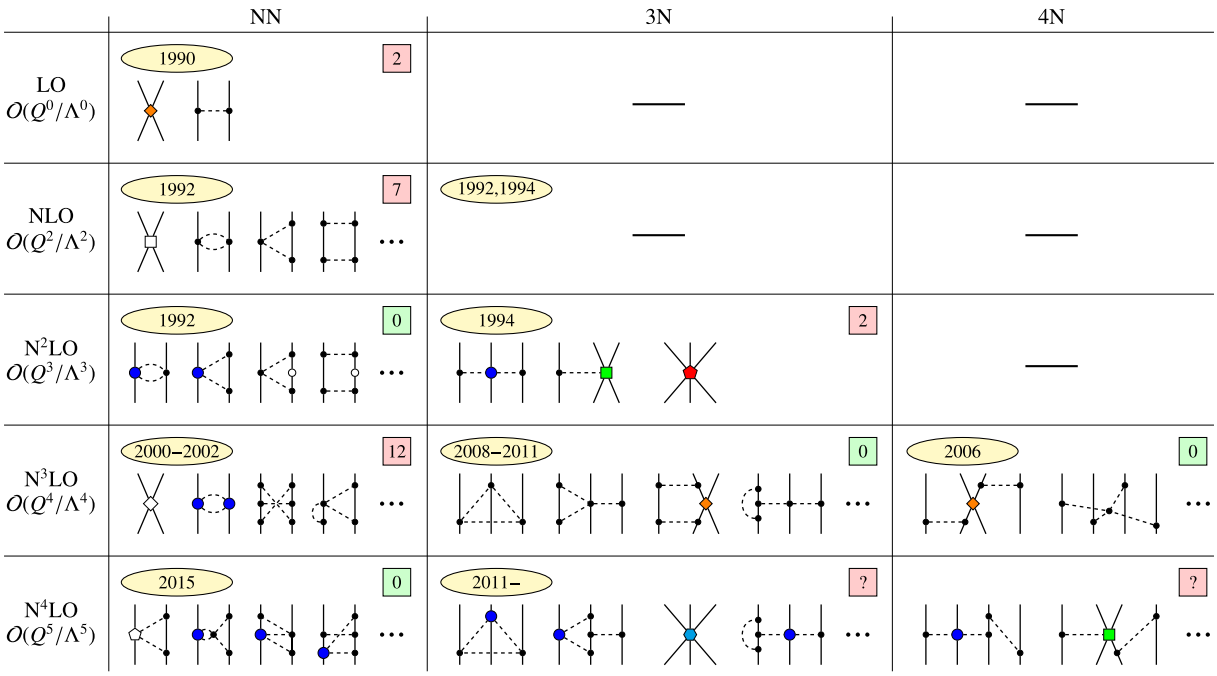

Figure 2.1: Interaction terms arising from Chiral EFT ordered according the power counting scheme by their momentum dependence p/Λ_b. Vertices show contact interactions and dashed lines show pion exchanges. Note that the definition of Q in this figure is different to Eq. (2.1). The figure is taken from Ref. [44] and was modified. ©2020 by Elsevier B.V.

dependence in different rows. Contact interactions are shown as vertices and pion exchanges are depicted as dotted lines. Higher-body interactions are a natural result of the expansion. The interactions are used to derive the general Hamiltonian

$$H = T + V_{NN} + V_{3N} + \dots , \tag{2.2}$$

in operator form, where T is the kinetic energy, V_{NN} (V_{3N}) are two(three)-nucleon interactions, and the dots represent four- and higher-nucleon interactions that are neglected.

The leading order (LO) interaction $V_{LO} \sim Q^0$ that contributes (first row of Fig. 2.1) is given by [40, 41]

$$V_{LO} = C_S + C_T \, \boldsymbol{\sigma}_1 \cdot \boldsymbol{\sigma}_2 - \frac{g_A^2}{4F_\pi^2} \frac{\boldsymbol{\sigma}_1 \cdot \boldsymbol{q} \; \boldsymbol{\sigma}_2 \cdot \boldsymbol{q}}{q^2 + m_\pi^2} \boldsymbol{\tau}_1 \cdot \boldsymbol{\tau}_2 \tag{2.3}$$

where C_S and C_T are momentum independent contact interactions and the last term is the one-pion exchange interaction with the pion mass m_π, nuclear axial coupling constant g_A, and pion decay constant F_π. Note that, e.g., the constant C_S transformed to coordinate space, corresponds to a delta interaction $V(\boldsymbol{r}', \boldsymbol{r}) \sim \delta(\boldsymbol{r}' - \boldsymbol{r})$. $\boldsymbol{\sigma}_i$ and $\boldsymbol{\tau}_i$ are the spin and isospin operators of particle

i, i.e.,

$$\boldsymbol{\sigma}_i = \begin{pmatrix} \sigma_{x,i} \\ \sigma_{y,i} \\ \sigma_{z,i} \end{pmatrix} \quad \text{and} \quad \boldsymbol{\tau}_i = \begin{pmatrix} \tau_{x,i} \\ \tau_{y,i} \\ \tau_{z,i} \end{pmatrix} , \tag{2.4}$$

and we use shorthands of the form $\boldsymbol{\sigma}_i \cdot \boldsymbol{\sigma}_j = \sum_{\alpha=x,y,z} \sigma_{\alpha,i}\sigma_{\alpha,j}$.

The next-to-leading order (NLO) is $\sim Q^2$ as shown in the second row of Fig. 2.1, next-to-next-to-leading order (N^{2}LO) interactions $V_{N^2LO} \sim Q^3$ are shown in the third row of Fig. 2.1. Their expressions have been derived and in general the operator structure $V_{NN}(\boldsymbol{p}', \boldsymbol{p}) = \langle \boldsymbol{p}' | \, V_{NN} \, | \boldsymbol{p} \rangle$ can be written as [40, 41]

$$\begin{aligned}
V_{NN}(\boldsymbol{p}', \boldsymbol{p}) =& V_C(\boldsymbol{p}', \boldsymbol{p}) + \boldsymbol{\tau}_1 \cdot \boldsymbol{\tau}_2 W_C(\boldsymbol{p}', \boldsymbol{p}) && (2.5)\\
&+ (V_S(\boldsymbol{p}', \boldsymbol{p}) + \boldsymbol{\tau}_1 \cdot \boldsymbol{\tau}_2 W_S(\boldsymbol{p}', \boldsymbol{p}))(\boldsymbol{\sigma}_1 \cdot \boldsymbol{\sigma}_2) && (2.6)\\
&+ (V_{LS}(\boldsymbol{p}', \boldsymbol{p}) + \boldsymbol{\tau}_1 \cdot \boldsymbol{\tau}_2 W_{LS}(\boldsymbol{p}', \boldsymbol{p}))(-i\boldsymbol{S} \cdot (\boldsymbol{q} \times \boldsymbol{k})) && (2.7)\\
&+ (V_{T,1}(\boldsymbol{p}', \boldsymbol{p}) + \boldsymbol{\tau}_1 \cdot \boldsymbol{\tau}_2 W_{T,1}(\boldsymbol{p}', \boldsymbol{p}))(\boldsymbol{\sigma}_1 \cdot \boldsymbol{q})(\boldsymbol{\sigma}_2 \cdot \boldsymbol{q}) && (2.8)\\
&+ (V_{T,2}(\boldsymbol{p}', \boldsymbol{p}) + \boldsymbol{\tau}_1 \cdot \boldsymbol{\tau}_2 W_{T,2}(\boldsymbol{p}', \boldsymbol{p}))(\boldsymbol{\sigma}_1 \cdot \boldsymbol{k})(\boldsymbol{\sigma}_2 \cdot \boldsymbol{k}) && (2.9)\\
&+ (V_{\sigma L}(\boldsymbol{p}', \boldsymbol{p}) + \boldsymbol{\tau}_1 \cdot \boldsymbol{\tau}_2 W_{\sigma L}(\boldsymbol{p}', \boldsymbol{p}))\,(\boldsymbol{\sigma}_1 \cdot (\boldsymbol{q} \times \boldsymbol{k}))\,(\boldsymbol{\sigma}_2 \cdot (\boldsymbol{q} \times \boldsymbol{k})) && (2.10)
\end{aligned}$$

where all V_i and W_i are scalar functions of the relative momentum $\boldsymbol{p} = \frac{1}{2}(\boldsymbol{k}_1 - \boldsymbol{k}_2)$ of incoming particles with momenta $\boldsymbol{k}_i$ and relative momentum $\boldsymbol{p}' = \frac{1}{2}(\boldsymbol{k}_1' - \boldsymbol{k}_2')$ of outgoing particles with momenta $\boldsymbol{k}_i'$. Furthermore, the momentum transfer is given by $\boldsymbol{q} = \boldsymbol{p}' - \boldsymbol{p}$, and in the exchange channel by $\boldsymbol{k} = \boldsymbol{p}' + \boldsymbol{p}$ and the total spin by $\boldsymbol{S} = \frac{1}{2}(\boldsymbol{\sigma}_1 + \boldsymbol{\sigma}_2)$. The various coefficient functions V_i and W_i receive contributions of short-range contact interactions and pion exchanges from the different orders NLO and N^{2}LO. For details we refer to Refs. [40, 41].

At N^{2}LO three-nucleon interactions start to contribute as shown in the second column of the third row of Fig. 2.1. Their expressions have been derived in Ref. [45, 46] and are given by two pion exchange (left diagram)

$$V_C = \frac{1}{2}\left(\frac{g_A}{2f_\pi}\right)^2 \sum_{i \neq j \neq k} \frac{(\boldsymbol{\sigma}_i \cdot \boldsymbol{q}_i)(\boldsymbol{\sigma}_j \cdot \boldsymbol{q}_j)}{(q_i^2 + m_\pi^2)(q_j^2 + m_\pi^2)} F_{ijk}^{\alpha\beta} \tau_i^\alpha \tau_j^\beta \tag{2.11}$$

with

$$F_{ijk}^{\alpha\beta} = \delta^{\alpha\beta}\left(-\frac{4c_1 m_\pi^2}{f_\pi^2} + \frac{2c_3}{f_\pi^2}\boldsymbol{q}_i \cdot \boldsymbol{q}_j\right) + \sum_\gamma \frac{c_4}{f_\pi^2}\epsilon^{\alpha\beta\gamma}\tau_k^\gamma \boldsymbol{\sigma}_k \cdot (\boldsymbol{q}_i \times \boldsymbol{q}_j)\,, \tag{2.12}$$

pion exchange plus contact (middle diagram)

$$V_D = -\frac{g_A}{8f_\pi^2}\frac{c_D}{f_\pi^2 \Lambda_\chi} \sum_{i \neq j \neq k} \frac{\boldsymbol{\sigma}_j \cdot \boldsymbol{q}_j}{q_j^2 + m_\pi^2} (\boldsymbol{\tau}_i \cdot \boldsymbol{\tau}_j)(\boldsymbol{\sigma}_i \cdot \boldsymbol{q}_j)\,, \tag{2.13}$$

and contact interaction (right diagram)

$$V_E = \frac{c_E}{2f_\pi^4 \Lambda_\chi} \sum_{i \neq j} (\boldsymbol{\tau}_i \cdot \boldsymbol{\tau}_j) \,. \tag{2.14}$$

Note that at N^{3}LO also four-nucleon interactions start to contribute. Their size has been estimated for neutron matter in the Hartree-Fock approximation in Ref. [47] to about $E_{4N,HF}(n_0) \approx -180\,\text{keV}$ at nuclear saturation density n_0 such that we neglect them.

Finally, we mention that in order to improve the convergence for many-body calculations, chiral EFT interactions can be evolved to lower resolutions using the similarity renormalization group (SRG), see, e.g. Refs [44, 48].

2.2 Partial-wave decomposition

In the previous section, the nuclear interaction was stated in operator form in the momentum basis. For the calculations of the equation of state, operators evaluated in a basis are important. The many-body expansion for the approximate evaluation of the EOS (see Chapter 3) is formulated using single-particle matrix elements in the calculations of this thesis, i.e.,

$$\left\langle \boldsymbol{k}_1' \sigma_1' \tau_1', \boldsymbol{k}_2' \sigma_2' \tau_2' \right| V_{NN} \left| \boldsymbol{k}_1 \sigma_1 \tau_1, \boldsymbol{k}_2 \sigma_2 \tau_2 \right\rangle \,, \tag{2.15}$$

$$\left\langle \boldsymbol{k}_1' \sigma_1' \tau_1', \boldsymbol{k}_2' \sigma_2' \tau_2', \boldsymbol{k}_3' \sigma_3' \tau_3' \right| V_{3N} \left| \boldsymbol{k}_1 \sigma_1 \tau_1, \boldsymbol{k}_2 \sigma_2 \tau_2, \boldsymbol{k}_3 \sigma_3 \tau_3 \right\rangle \,, \tag{2.16}$$

where $\boldsymbol{k}_i$, σ_i, τ_i are momentum, spin projection, and isospin projection of incoming particle i and primes denote outgoing particles.

Our strategy is to load precalculated matrix elements (evaluated in a basis) and use them for our numerical calculations. Note, however, that the expression for V_{3N} depends on 4 momenta each with 3 dimensions (the matrix elements do not depend on center-of-mass momentum, see e.g. Ref. [44]), which makes it impossible to store them due to memory constrains.

Instead, following, e.g., Ref. [44], we use precomputed matrix elements in a partial-wave basis and reconstruct the single-particle basis when needed. Schematically the partial-wave basis for three-nucleon interactions can be derived as follows (following, e.g., Ref. [44]). First the single particle momenta $\boldsymbol{k}_i$ in

$$\left| \boldsymbol{k}_1 \sigma_1 \tau_1, \boldsymbol{k}_2 \sigma_2 \tau_2, \boldsymbol{k}_3 \sigma_3 \tau_3 \right\rangle \,, \tag{2.17}$$

are rewritten to (relative) Jacobi momenta $\boldsymbol{p}$ and $\boldsymbol{q}$

$$\left| \boldsymbol{p}\boldsymbol{q} \right\rangle \left| \sigma_1 \tau_1, \sigma_2 \tau_2, \sigma_3 \tau_3 \right\rangle \,. \tag{2.18}$$

Note that the three-nucleon center of mass momenta is omitted as matrix elements do not depend

on it. Next the momenta $\boldsymbol{p}$ and $\boldsymbol{q}$ are expanded in spherical harmonics

$$|pL_{12}m_{L_{12}}, qL_3m_{L_3}\rangle \left|(\tfrac{1}{2}\tfrac{1}{2})S_{12}M_{S_{12}}\right\rangle \left|(\tfrac{1}{2}\tfrac{1}{2})T_{12}M_{T_{12}}\right\rangle |\sigma_3\tau_3\rangle \tag{2.19}$$

with new states that only depend on the absolute values of the momenta and new angular momentum quantum numbers L_i and projections m_{L_i}. Furthermore the single particle spins and isospin of the first two particles are coupled to $\boldsymbol{S}_{12} = \boldsymbol{s}_1 + \boldsymbol{s}_2$ with projection $M_{S_{12}}$ and $\boldsymbol{T}_{12} = \boldsymbol{t}_1 + \boldsymbol{t}_2$ with projection $M_{T_{12}}$. Next $\boldsymbol{L}_{12}$ and $\boldsymbol{S}_{12}$ are coupled to a total angular momentum $\boldsymbol{J}_{12} = \boldsymbol{L}_{12} + \boldsymbol{S}_{12}$ and $\boldsymbol{L}_3$ is coupled to the spin of the third particle to a total angular momentum $\boldsymbol{J}_3$

$$\left|pq, (L_{12}S_{12})J_{12}m_{J_{12}}, (L_3, \tfrac{1}{2})J_3m_{J_3}, T_{12}M_{T_{12}}, \tau_3\right\rangle \tag{2.20}$$

with corresponding projections $m_{J_{12}}$ and $M_{T_{12}}$. Finally $\boldsymbol{J}_{12}$ is coupled to $\boldsymbol{J}_3$ to a total momentum $\boldsymbol{J}$, and $\boldsymbol{T}_{12}$ is coupled to the isospin of the third particle to a total isospin $\boldsymbol{T}$ such that the final basis states are given by

$$\left|pq, [(L_{12}S_{12})J_{12}, (L_3, \tfrac{1}{2})J_3m_{J_3}]Jm_J, [T_{12}, \tfrac{1}{2}]Tm_T\right\rangle \ . \tag{2.21}$$

The matrix elements evaluated in this basis only depend on four absolute values of momenta. For N grid points per momentum axis, the partial wave basis needs only N^4 total grind points instead of N^{12} for the single-particle basis. This reduction allows to store the partial-wave decomposed matrix elements.

One major advantage of using partial-wave decomposed matrix elements is that the code is universal and does not depend on the particular nuclear interaction that is used. Alternatively Ref. [49] developed a framework that allows to evaluate the matrix elements, of some particular interactions, in the single-particle basis on the fly from the operator expressions.

Starting from the matrix elements in partial waves, the single-particle basis can be constructed using [44]

$$\begin{aligned}
&\langle \boldsymbol{k}_1\sigma_1\tau_1, \boldsymbol{k}_2\sigma_2\tau_2, \boldsymbol{k}_3\sigma_3\tau_3| \, V_{3N} \left|\boldsymbol{k}'_1\sigma'_1\tau'_1, \boldsymbol{k}'_2\sigma'_2\tau'_2\boldsymbol{k}'_3\sigma'_3\tau'_3\right\rangle \\
=&\sum_{JT}\sum_{\alpha\alpha'}\sum_{M_JM_T}\sum_{M_\alpha M_{\alpha'}} \\
&\times Y^*_{L'_{12}M'_{L_{12}}}(\hat{p}')Y^*_{L'_3M'_{L_3}}(\hat{q}')Y_{L_{12}M_{L_{12}}}(\hat{p})Y_{L_3M_{L_3}}(\hat{q}) \\
&\times C^{S_{12}M_{S_{12}}}_{\frac{1}{2}\sigma_1\frac{1}{2}\sigma_2}C^{T_{12}M_{T_{12}}}_{\frac{1}{2}\tau_1\frac{1}{2}\tau_2}C^{J_{12}M_{J_{12}}}_{L_{12}M_{L_{12}}S_{12}M_{S_{12}}}C^{J_3M_{J_3}}_{L_3M_{L_3}\frac{1}{2}\sigma_3}C^{JM_J}_{J_{12}M_{J_{12}}J_3M_{J_3}}C^{TM_T}_{T_{12}M_{T_{12}}\frac{1}{2}\tau_3} \\
&\times C^{S'_{12}M'_{S_{12}}}_{\frac{1}{2}\sigma'_1\frac{1}{2}\sigma'_2}C^{T'_{12}M'_{T_{12}}}_{\frac{1}{2}\tau'_1\frac{1}{2}\tau'_2}C^{J'_{12}M'_{J_{12}}}_{L'_{12}M'_{L_{12}}S'_{12}M'_{S_{12}}}C^{J'_3M'_{J_3}}_{L'_3M'_{L_3}\frac{1}{2}\sigma'_3}C^{JM_J}_{J'_{12}M'_{J'_{12}}J'_3M'_{J_3}}C^{TM_T}_{T'_{12}M'_{T_{12}}\frac{1}{2}\tau'_3} \\
&\times \langle pqJT\alpha| \, V_{3N} \left|p'q'JT\alpha'\right\rangle
\end{aligned}$$

for three-nucleon interactions where the collective label $\alpha = (J_{12}S_{12}L_{12}T_{12}J_3L_3)$ was used, $C^{Jm_J}_{Lm_L,Sm_S}$ are Clebsch-Gordan coefficients and $Y_{Lm_L}(\hat{p})$ are spherical harmonics.

Note that the expressions are in principle sums that contain an infinite amount of terms. In

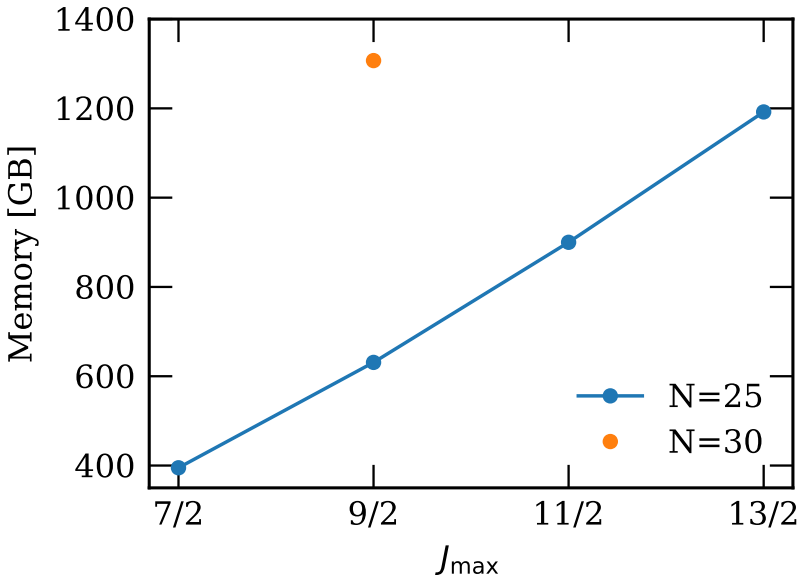

Figure 2.2: Memory needed to store the partial wave decomposed 3N matrix elements as a function of maximal total angular momentum $J_{\max}$ (see text for details).

practical calculations they have to be truncated. Following Refs. [44, 50] we truncate the sums for V_{3N} by restricting the total angular momentum $J \leq J_{\max}$ and the angular momentum of the two-nucleon system by $J_{12} \leq J_{12,\max}$. Figure 2.2 shows the memory required to store the partial wave matrix elements as a function of $J_{\max}$. An analysis of the partial-wave convergence with respect to $J_{\max}$ can be found in Ref. [50]. To improve the accuracy of our calculations, we employ a momentum grid that is more dense below $p_{mid} = 2\,\mathrm{fm}^{-1}$, as higher momenta are less important and restricted by the interaction cutoff, e.g., $\Lambda = 500\,\mathrm{MeV}$.

In this thesis we use partial-wave decomposed matrix elements provided by Ref. [51].

2.3 Regularization

Finally the interactions have to be regulated. We use nonlocal regulator in momentum space [44, 52]

$$\langle \boldsymbol{p}' | \, V_{NN}^{\text{reg.}} \, | \boldsymbol{p} \rangle = f_2(\boldsymbol{p}') \, \langle \boldsymbol{p}' | \, V_{NN} \, | \boldsymbol{p} \rangle \, f_2(\boldsymbol{p}) \tag{2.22}$$

$$\langle \boldsymbol{p}'\boldsymbol{q}' | \, V_{3N}^{\text{reg.}} \, | \boldsymbol{p}\boldsymbol{q} \rangle = f_3(\boldsymbol{p}', \boldsymbol{q}') \, \langle \boldsymbol{p}'\boldsymbol{q}' | \, V_{3N} \, | \boldsymbol{p}\boldsymbol{q} \rangle \, f_3(\boldsymbol{p}, \boldsymbol{q}) \tag{2.23}$$

with regulator functions

$$f_2(p) = \exp\left(- \left(\frac{\boldsymbol{p}^2}{\Lambda^2} \right)^n \right) \tag{2.24}$$

$$f_3(p, q) = \exp\left(- \left(\frac{\boldsymbol{p}^2 + \frac{3}{4}\boldsymbol{q}^2}{\Lambda^2} \right)^n \right) \tag{2.25}$$

where the momenta for two-nucleon interactions are given above and Jacobi momenta are used for three-nucleon interactions (see, e.g., Ref. [44]) for the calculations in this thesis. We use $n = 4$ for the regulator f_3 (for choice in f_2 see Ref. [52]).

2.4 Uncertainty quantification

The expansion of the nuclear Hamiltonian has to be truncated at a given order, e.g., N^{3}LO ($\sim Q^4$). Consequently, observables that are calculated with the truncated Hamiltonian will also be truncated. Given the systematic expansion of chiral EFT, these truncation errors can be estimated by comparing calculations of observables at different orders in the expansion. This is a crucial advantage compared to other interaction models.

The observable (e.g. free energy) has been calculated at different orders in the chiral expansion

$$X^{(0)}(x), \ldots, X^{(k)}(x) \tag{2.26}$$

where $X^{(n)}(x)$ has been calculated with interactions at order Q^n and x is a shorthand for, e.g., proton fraction, temperature, and density (x, T, n). Following Ref. [53] we assuming that the observable also has a expansion

$$X^{(k)}(x) = X_{\text{ref}}(x) \sum_{n=0}^{k} c_n(x) Q^n(x) \tag{2.27}$$

in powers of the EFT parameter $Q = p/\lambda_b$, and $X_{\text{ref}}(x)$ sets the scale such that the expansion coefficients c_i are dimensionless and have natural size (of order one). They can be extracted by differences of different orders, e.g., for $n > 0$

$$c_n(x) = \frac{X^{(k)}(x) - X^{(k-1)}(x)}{X_{\text{ref}}(x) Q^n(x)} \,. \tag{2.28}$$

The truncation error is then given by [53]

$$\Delta X^{(k)}(x) = X_{\text{ref}}(x) \sum_{n=k+1}^{\infty} c_n(x) Q^n(x) \,, \tag{2.29}$$

where the $c_n(x)$ for $n > k$ are unknown.

The simplest estimate of the truncation error is than given by assuming that the next unknown coefficient dominates the uncertainties [53]

$$\Delta X^{(k)}(x) \approx X_{\text{ref}}(x) c_{k+1}(x) Q^{k+1}(x) \tag{2.30}$$

and estimating $c_{k+1}(x)$ using the known coefficients as

$$c_{k+1}(x) \approx \max\left(|c_0(x)|, \ldots, |c_k(x)|\right) \,. \tag{2.31}$$

This uncertainty estimate can also be written as

$$\Delta X^{(k)}(x) \approx Q \cdot \max\left(|X^{(k)}(x) - X^{(k-1)}(x)|, \Delta X^{(k-1)}(x)\right) , \tag{2.32}$$

for observables and is also given in Ref. [54]. In this thesis Eq. (2.32) is referred to as the EKM prescription.

This estimation of the truncation error can be improved in two ways:

1. Instead of assuming that $\Delta X^{(k)}(x)$ is dominated by the first term, more terms can be included in Eq. (2.30).

2. A better estimate for the c_n for $n > k$ (2.31) can be use, e.g., in Ref [53] a posterior distribution $P(c_{k+1}, c_{k+2}, \ldots | c_0, c_1, \ldots, c_k)$ at fixed x has been derived using Bayesian statics.

The recent uncertainty estimated of Ref. [55] treat the coefficients $c_n(x)$ as continuous functions and construct a Gaussian Process (distribution of functions instead of points, see Chapter 4) to describe them. They assume that all coefficients are distributed according to the same Gaussian process where the mean function and kernel can be learned from known coefficients. This sum in Eq. (2.29) can be evaluated analytically in this case without truncations. This new method adds correlations between nearby points (e.g., in density). It has been applied to nuclear matter in Refs. [16, 56]. Furthermore this allows for better propagation of uncertainties to derived quantities (e.g., Ref. [56] use it to construct a distribution of saturation point and saturation energy of symmetric nuclear matter).

3 Many-body perturbation theory

In this thesis, many-body perturbation theory (MBPT) is used to (approximately) calculate the thermodynamic properties of matter starting from the nuclear Hamiltonian. In Sec. 3.1, we first provide an overview of finite-temperature MBPT. A detailed introduction can be found in Refs. [57, 58], we only highlight the parts that are important for this thesis. In Sec. 3.2, we show how an expansion for the free energy can be derived. In zero-temperature MBPT calculations it is common to use a HF reference state (HF-MBPT), since this improves the many-body convergence compared to MBPT around the noninteracting Fermi gas. The generalization of HF-MBPT to finite temperatures is discuss in Sec. 3.3. Parts of this chapter have already been published in Ref. [59] together with Corbinian Wellenhofer, who contributed to the formal developments.

3.1 Grand-canonical ensemble expansion

We determine the thermodynamic properties of nuclear matter starting from the grand-canonical potential [7]

$$\Omega(T, \mu_n, \mu_p) = -\frac{1}{\beta} \ln Z\left(T, \mu_n, \mu_p\right) , \tag{3.1}$$

where $Z(T, \mu_n, \mu_p) = \mathrm{Tr}\left(e^{-\beta(H-\mu_n N_n-\mu_p N_p)}\right)$ is the partition function of the system, with $T = 1/\beta$ the temperature, N_i the particle number of neutrons and protons, and μ_i the chemical potentials of neutrons ($i = n$) and protons ($i = p$). Here and in the following we work in units where $\hbar = c = k_b = 1$. The Hamiltonians H considered in this work consist of the kinetic term (H_0) plus contributions from two- and three-nucleon interactions (see Sec. 5.1):

$$H = H_0 + V_{NN} + V_{3N} . \tag{3.2}$$

MBPT allows to choose a specific partitioning of the Hamiltonian which defines the reference basis that is used for the perturbative expansion, see, e.g., Ref. [60]. The simplest choice consists in expanding $\Omega(T, \mu_n, \mu_p)$ around the noninteracting system with Hamiltonian H_0. However, a more general reference system can be chosen, e.g. [60]

$$H = (H_0 + U) + \lambda \left(V_{NN} + V_{3N} - U\right) , \tag{3.3}$$

where the expansion is around the reference system with Hamiltonian H_0+U and the interaction part $V_{NN} + V_{3N} - U$ is treated as a perturbation. Here in this thesis, the operator U is chosen

as a single-particle potential

$$U = \sum_{\alpha} U_{\alpha} a_{\alpha}^{\dagger} a_{\alpha} \,, \tag{3.4}$$

with creation and annihilation operators $a_{\alpha}^{\dagger}$ and a_{α} where we use collective labels $\alpha = (\mathbf{k}, \sigma, \tau)$ for momentum $\mathbf{k}$, spin projection $\sigma = \pm 1/2$, isospin projection $\tau = \pm 1/2$ (neutron or proton) and the shorthand notation $\sum_{\alpha} f_{\alpha} = \sum_{\sigma\tau} \int \frac{\mathrm{d}^3\mathbf{k}}{(2\pi)^3} f(\mathbf{k}, \sigma, \tau)$. The single-particle spectrum of the reference system is then given by

$$\varepsilon_{\alpha} = \frac{k^2}{2m_{\tau}} + U_{\alpha} \,. \tag{3.5}$$

The perturbation series of the grand-canonical potential is then obtained as (see, e.g. Refs. [57, 58])

$$\Omega(T, \mu) = \sum_{l=0}^{\infty} \lambda^l \Omega_l(T, \mu) \,, \tag{3.6}$$

where

$$\Omega_0(T, \mu) = -\frac{1}{\beta} \sum_{\alpha} \ln\left(1 + e^{-\beta(\varepsilon_{\alpha} - \mu)}\right) \tag{3.7}$$

is the grand-canonical potential of the reference system. In the following sections the contributions from different orders λ will be discussed. The first- and second-order energy contributions at finite temperature with arbitrary neutron-proton asymmetries have been evaluated based on Refs. [57, 58] and have been checked against already derived results when possible.

3.1.1 Non-interacting contribution

The expression for the non-interaction contribution of the grand-canonical potential Eq. (3.7) can be rewritten as

$$\Omega_0(T, \mu_n, \mu_p) = -\frac{4\pi\, g}{\beta} \sum_{\tau} \int_0^{\infty} \frac{\mathrm{d}k}{(2\pi)^3}\, k^2 \ln\left(1 + e^{-\beta(\epsilon(k,\tau) - \mu_{\tau})}\right) \tag{3.8}$$

$$= -g \frac{4\pi}{3(2\pi)^3} \sum_{\tau} \int_0^{\infty} \mathrm{d}k\, k^3 \epsilon'(k, \tau) n(k, \mu, \tau) \,, \tag{3.9}$$

where the spin degeneracy $g = 2$ and $n(k, \mu, \tau)$ are Fermi-Dirac distributions. Note that in general the evaluation of the single-particle energy ϵ depends on the one body potential Eq. (3.4), which typically has to be evaluated self-consistently with the spectrum. Without the single-particle potential, e.g. $U_{\alpha} = 0$, the integrals can be rewritten to

$$\Omega_{0, U_{\alpha}=0} = -\frac{g}{2\sqrt{2}} \sum_{\tau} \left(\frac{m_{\tau}}{\pi}\right)^{3/2} T^{5/2} F_{3/2}(\beta\mu_{\tau}) \tag{3.10}$$

where we have used Fermi-Dirac integrals [7]

$$F_i(x) = \frac{1}{\Gamma(i+1)} \int_0^\infty \mathrm{d}t \, \frac{t^i}{\exp(t-x)+1} \,. \tag{3.11}$$

Using standard thermodynamic relations [7], density n, entropy S and pressure P can be derived as

$$n_{0,U_\alpha=0} = \frac{g}{2\sqrt{2}} \sum_\tau \left(\frac{m_\tau}{\pi}\right)^{3/2} T^{3/2} F_{1/2}(\beta\mu_\tau) \,, \tag{3.12}$$

$$S_{0,U_\alpha=0} = \frac{g}{2\sqrt{2}} \sum_\tau \left(\frac{m_\tau}{\pi}\right)^{3/2} \left(\frac{5}{2} T^{3/2} F_{3/2}(\beta\mu_\tau) - \mu_\tau T^{1/2} F_{1/2}(\beta\mu_\tau)\right) \,, \tag{3.13}$$

$$P_{0,U_\alpha=0} = -\Omega_{0,U_\alpha=0} \,, \tag{3.14}$$

where we have used the relation $F_i'(x) = F_{i-1}(x)$.

3.1.2 First-order energy contributions

The first-order contributions can be expressed using Hugenholtz diagrams as shown in Fig. 3.1 (see, e.g., Refs. [57, 58] for an introduction to the diagrammatic technique and, e.g., Refs. [44, 61] for similar diagrams). Each circle vertex represents a two body interaction V_{NN}, while squares represent three nucleon interactions V_{3N}. Solid lines that connect vertices, represent propagators.

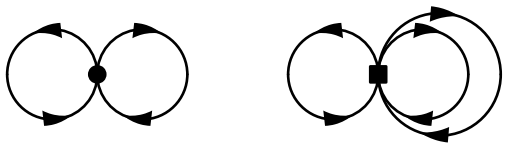

Figure 3.1: First order (Hartree-Fock) Hugenholtz diagrams for two nucleon interactions (left) and three nucleon interactions (right). Diagrams based on Refs. [44, 61].

Analytical expressions for the diagrams involving two- and three nucleon interactions can be derived as (see, e.g., Refs. [57, 58, 62])

$$\Omega_1^{NN}(T, \mu_n, \mu_p) = \frac{1}{2} \sum_{\alpha\beta} n_\alpha n_\beta \left\langle \alpha\beta \right| \mathcal{A}_{12} V_{\mathrm{NN}} \left| \alpha\beta \right\rangle \tag{3.15}$$

and

$$\Omega_1^{3N}(T, \mu_n, \mu_p) = \frac{1}{6} \sum_{\alpha\beta\gamma} n_\alpha n_\beta n_\gamma \left\langle \alpha\beta\gamma \right| \mathcal{A}_{123} V_{3N} \left| \alpha\beta\gamma \right\rangle \,, \tag{3.16}$$

respectively, where $\mathcal{A}_{12}$ and $\mathcal{A}_{123}$ are two- and three-particle antisymmetrizers given by

$$\mathcal{A}_{\mathrm{NN}} = 1 - P_{12} \tag{3.17}$$

$$\mathcal{A}_{\mathrm{3N}} = 1 - P_{12} - P_{13} - P_{23} + P_{13}P_{23} + P_{12}P_{23} \tag{3.18}$$

with permutation operators P_{ij} and the Fermi-Dirac distributions are given by

$$n_\alpha = \frac{1}{e^{\beta(\varepsilon_\alpha - \mu_\tau)} + 1}\,. \tag{3.19}$$

Corresponding zero-temperature expressions can be found in, e.g., Ref. [61]. Equations (3.15) and (3.16) matches the corresponding contribution to the ground-state energy in zero-temperature MBPT, with the Fermi-Dirac distributions replaced by $\theta(k_\mathrm{F} - k)$. This correspondence is lost at second order and beyond, where additional so-called anomalous contributions [57, 58, 63] appear in finite-temperature MBPT.

Furthermore there is one additional contribution due to the single-particle potential U given by

$$\Omega_1^U(T, \mu_n, \mu_p) = -\sum_\alpha n_\alpha U_\alpha\,. \tag{3.20}$$

3.1.3 Second-order energy contributions

The second-order contributions are represented diagramatically in Fig. 3.2. This results in the following expression for the second-order two-nucleon contribution [57, 58, 62]

$$\Omega_2^{\mathrm{NN}}(T, \mu_n, \mu_p) = -\frac{1}{8}\sum_{\alpha\beta\gamma\delta} P_{\alpha\beta\gamma\delta}\left|\langle\alpha\beta|\,\mathcal{A}_{12}V_{\mathrm{N}N}\,|\gamma\delta\rangle\right|^2, \tag{3.21}$$

with

$$P_{\alpha\beta\gamma\delta} = \frac{n_\alpha n_\beta(1-n_\gamma)(1-n_\delta) - (1-n_\alpha)(1-n_\beta)n_\gamma n_\delta}{\varepsilon_\gamma + \varepsilon_\delta - \varepsilon_\alpha - \varepsilon_\beta}\,, \tag{3.22}$$

for the phase space contribution and the energy denominator. This can be rewritten to

$$P_{\alpha\beta\gamma\delta} = \frac{1}{8}\left(\prod_{i=1}^{4}\mathrm{sech}\left(\frac{\beta}{2}\left(\epsilon_i - \mu\right)\right)\right)\frac{\sinh\left(\frac{\beta}{2}\left(\epsilon_\gamma + \epsilon_\delta - (\epsilon_\alpha + \epsilon_\beta)\right)\right)}{\epsilon_\gamma + \epsilon_\delta - (\epsilon_\alpha + \epsilon_\beta)}\,. \tag{3.23}$$

Note that $|\mathrm{sech}(x)| \leq 1$ and that the part involving the energy denominator satisfies

$$\lim_{x\to 0}\frac{\sinh(x)}{x} = 1\,, \tag{3.24}$$

such that $P_{\alpha\beta\gamma\delta}$ is finite in the limit $\varepsilon_\gamma + \varepsilon_\delta - \varepsilon_\alpha - \varepsilon_\beta \to 0$ and can be integrated. See, e.g., Ref. [44] for corresponding zero-temperature expression.

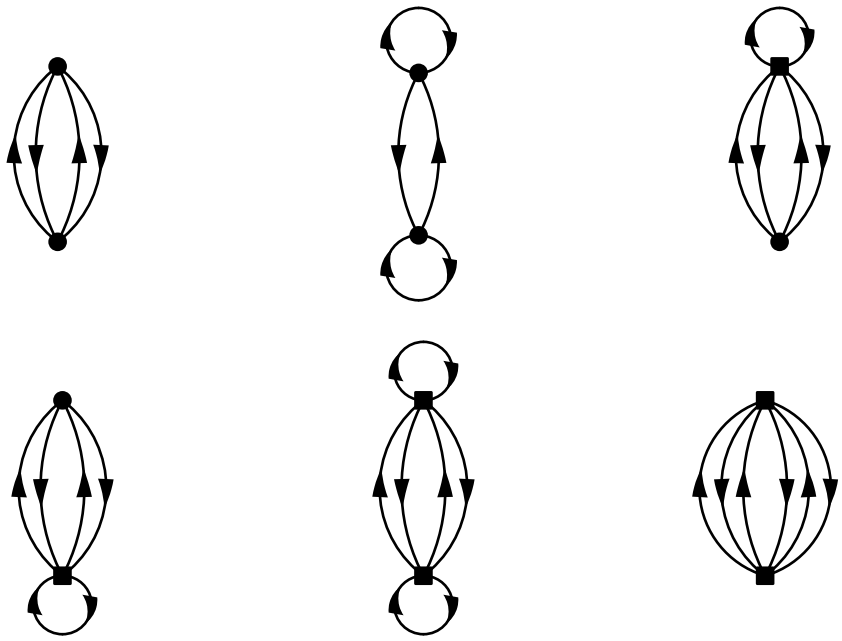

Figure 3.2: Diagrammatic representation of the second order MBPT contributions. The individual diagrams and expressions will be called (from left to right and top to bottom): NN, NN-anomalous, 3N-NN, NN-3N, 3N-3N, 3N-res. Note that 3N-NN and NN-3N are equal. We include only one and include the other contribution by updating the symmetry factor. Therefore, Eq. (3.26) has a prefactor 1/4 instead of 1/8. Furthermore there are more anomalous diagrams not shown that cancel when employing a HF spectrum (including the NN-anomalous diagram). Diagrams based on Refs. [44, 61].

The anomalous diagram with only NN vertices is given by [57, 58, 62]

$$\Omega^{\mathrm{NN}}_{2,\mathrm{anomalous}}(T,\mu_n,\mu_p) = -\frac{1}{2T}\sum_{\beta} n_\beta\,(1-n_\beta)\left(\sum_{\alpha} n_\alpha \,\langle\alpha\beta|\,\mathcal{A}_{12}V_{\mathrm{N}N}\,|\alpha\beta\rangle\right)^2 . \tag{3.25}$$

The other diagrams in Fig. 3.2 that involve three-nucleon interactions are given by

$$\Omega^{\mathrm{NN\text{-}3N}}_{2}(T,\mu_n,\mu_p) = -\frac{1}{4}\sum_{\alpha\beta\gamma\delta\epsilon} P_{\alpha\beta\gamma\delta}\, n_\epsilon \,\langle\alpha\beta|\,\mathcal{A}_{12}V_{NN}\,|\gamma\delta\rangle\,\langle\gamma\delta\epsilon|\,\mathcal{A}_{123}V_{3N}\,|\alpha\beta\epsilon\rangle \tag{3.26}$$

$$\Omega^{\mathrm{3N\text{-}3N}}_{2}(T,\mu_n,\mu_p) = -\frac{1}{8}\sum_{\alpha\beta\gamma\delta\epsilon\phi} P_{\alpha\beta\gamma\delta}\, n_\epsilon \mathrm{n}_\phi \,\langle\alpha\beta\epsilon|\,\mathcal{A}_{123}V_{3N}\,|\gamma\delta\epsilon\rangle\,\langle\gamma\delta\phi|\,\mathcal{A}_{123}V_{3N}\,|\alpha\beta\phi\rangle \tag{3.27}$$

$$\Omega^{\mathrm{3N\text{-}res}}_{2}(T,\mu_n,\mu_p) = -\frac{1}{72}\sum_{\alpha\beta\gamma\delta\epsilon\phi} \frac{n_\alpha n_\beta n_\gamma \bar{n}_\delta \bar{n}_\epsilon \bar{n}_\phi - \bar{n}_\alpha \bar{n}_\beta \bar{n}_\gamma n_\delta n_\epsilon n_\phi}{\epsilon_\delta+\epsilon_\epsilon+\epsilon_\phi-(\epsilon_\alpha+\epsilon_\beta+\epsilon_\gamma)} \times \langle\alpha\beta\gamma|\,\mathcal{A}_{123}V_{3N}\,|\delta\epsilon\phi\rangle\,\langle\delta\epsilon\phi|\,\mathcal{A}_{123}V_{3N}\,|\alpha\beta\gamma\rangle\ . \tag{3.28}$$

For corresponding expressions at zero temperature see e.g. Ref. [44]. Note that we have omitted the expression of the 3N-NN diagram. It has the same contribution as the NN-3N diagrams and we therefore include it in the symmetry factor in Eq. (3.26) (which now is 1/4 instead of 1/8).

Furthermore, there are diagrams at second order that involve the one-body potential. For the

diagrams with two nucleon interactions they are shown in Fig. 3.5 below and their analytical expressions are given by

$$\Omega_2^{\text{NN-U}}(T,\mu_n,\mu_p) = \frac{1}{2T}\sum_\beta n_\beta\,(1-n_\beta)\left(\sum_\alpha n_\alpha \langle\alpha\beta|\,\mathcal{A}_{12}V_{NN}\,|\alpha\beta\rangle\right)U_\beta\,, \tag{3.29}$$

$$\Omega_2^{\text{U-NN}}(T,\mu_n,\mu_p) = \frac{1}{2T}\sum_\alpha n_\alpha\,(1-n_\alpha)\,U_\alpha\left(\sum_\beta n_\beta \langle\alpha\beta|\,\mathcal{A}_{12}V_{NN}\,|\alpha\beta\rangle\right)\,, \tag{3.30}$$

$$\Omega_2^{\text{U-U}}(T,\mu_n,\mu_p) = -\frac{1}{2T}\sum_\beta n_\beta\,(1-n_\beta)\,U_\beta^2\,. \tag{3.31}$$

The anomalous contributions given by Eq. (3.25) and Eqs. (3.29)–(3.31) are not needed in the zero-temperature formalism [57, 58, 63].

3.1.4 Third-order energy contributions

The third order contributions that only involve two-nucleon interactions are shown in Fig. 3.3.

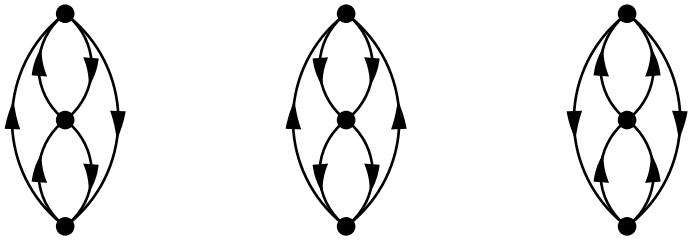

Figure 3.3: Third order diagrams involving two nucleon vertices. The diagrams are called (from left to right): particle-hole (ph), hole-hole (hh), and particle-particle (pp). Diagrams based on Refs. [44, 61].

Their analytical expressions have been derived in Ref. [60] for the finite-temperatures formalism

$$\Omega_3^{\text{ph}} = \frac{1}{3}\sum_{\alpha\beta\gamma\delta\epsilon\phi} n_\alpha n_\beta n_\gamma \bar{n}_\delta \bar{n}_\epsilon \bar{n}_\phi\, F^{\alpha\beta,\delta\epsilon}_{\beta\gamma,\delta\phi}\, \langle\alpha\beta|\,\mathcal{A}_{12}V_{NN}\,|\delta\epsilon\rangle\,\langle\gamma\epsilon|\,\mathcal{A}_{12}V_{NN}\,|\alpha\phi\rangle\,\langle\delta\phi|\,\mathcal{A}_{12}V_{NN}\,|\beta\gamma\rangle \tag{3.32}$$

$$\Omega_3^{\text{pp}} = \frac{1}{24}\sum_{\alpha\beta\gamma\delta\epsilon\phi} n_\alpha n_\beta \bar{n}_\gamma \bar{n}_\delta \bar{n}_\epsilon \bar{n}_\phi\, F^{\alpha\beta,\gamma\delta}_{\alpha\beta,\epsilon\phi}\, \langle\alpha\beta|\,\mathcal{A}_{12}V_{NN}\,|\gamma\delta\rangle\,\langle\gamma\delta|\,\mathcal{A}_{12}V_{NN}\,|\epsilon\phi\rangle\,\langle\epsilon\phi|\,\mathcal{A}_{12}V_{NN}\,|\alpha\beta\rangle \tag{3.33}$$

$$\Omega_3^{\text{hh}} = \frac{1}{24}\sum_{\alpha\beta\gamma\delta\epsilon\phi} n_\alpha n_\beta n_\gamma n_\delta \bar{n}_\epsilon \bar{n}_\phi\, F^{\alpha\beta,\epsilon\phi}_{\gamma\delta,\epsilon\phi}\, \langle\alpha\beta|\,\mathcal{A}_{12}V_{NN}\,|\epsilon\phi\rangle\,\langle\epsilon\phi|\,\mathcal{A}_{12}V_{NN}\,|\gamma\delta\rangle\,\langle\gamma\delta|\,\mathcal{A}_{12}V_{NN}\,|\alpha\beta\rangle \tag{3.34}$$

where we use the shorthand $\bar{n}_i = 1 - n_i$. The phase space contribution together with the energy

denominators is given by

$$F(D_1, D_2) = \frac{1}{D_1 D_2} + \frac{\exp(-\beta D_1)}{D_1(D_1 - D_2)} - \frac{\exp(-\beta D_2)}{D_2(D_1 - D_2)}, \tag{3.35}$$

for the third order NN diagrams. Note, F is symmetric $F(D_1, D_2) = F(D_2, D_1)$ and finite in the limits $D_1 \to 0$, $D_2 \to 0$, $D_1 \to D_2$ and $D_1 \to D_2 \to 0$, such that there are no poles in the integration [60]. Finally for the diagram expressions we use the shorthand

$$F^{\alpha\beta,\delta\epsilon}_{\beta\gamma,\delta\phi} = F\left(\epsilon_\delta + \epsilon_\epsilon - \epsilon_\alpha - \epsilon_\beta, \epsilon_\delta + \epsilon_\phi - \epsilon_\beta - \epsilon_\gamma\right) . \tag{3.36}$$

Furthermore there are more diagrams involving three-nucleon interactions. Non-residual diagrams can be derived by replacing a NN vertex with a self-contracted 3N vertex, e.g.,

$$\langle\alpha\beta|\, \mathcal{A}_{12} V_{NN} \,|\delta\epsilon\rangle \longrightarrow \sum_\omega n_\omega \,\langle\alpha\beta\omega|\, \mathcal{A}_{123} V_{3N} \,|\delta\epsilon\omega\rangle . \tag{3.37}$$

For example for one three-nucleon vertex this results in

$$\begin{aligned}
\Omega_3^{\text{ph-3N-NN-NN}} = \sum_{\alpha\beta\gamma\delta\epsilon\phi} & n_\alpha n_\beta n_\gamma \bar{n}_\delta \bar{n}_\epsilon \bar{n}_\phi \, F^{\alpha\beta,\delta\epsilon}_{\beta\gamma,\delta\phi} \left(\sum_\omega n_\omega \,\langle\alpha\beta\omega|\, \mathcal{A}_{123} V_{3N} \,|\delta\epsilon\omega\rangle \right) \\
& \times \langle\gamma\epsilon|\, \mathcal{A}_{12} V_{NN} \,|\alpha\phi\rangle \,\langle\delta\phi|\, \mathcal{A}_{12} V_{NN} \,|\beta\gamma\rangle
\end{aligned} \tag{3.38}$$

$$\begin{aligned}
\Omega_3^{\text{pp-3N-NN-NN}} = \frac{1}{8} \sum_{\alpha\beta\gamma\delta\epsilon\phi} & n_\alpha n_\beta \bar{n}_\gamma \bar{n}_\delta \bar{n}_\epsilon \bar{n}_\phi \, F^{\alpha\beta,\gamma\delta}_{\alpha\beta,\epsilon\phi} \left(\sum_\omega n_\omega \,\langle\alpha\beta\omega|\, \mathcal{A}_{123} V_{3N} \,|\gamma\delta\omega\rangle \right) \\
& \times \langle\gamma\delta|\, \mathcal{A}_{12} V_{NN} \,|\epsilon\phi\rangle \,\langle\epsilon\phi|\, \mathcal{A}_{12} V_{NN} \,|\alpha\beta\rangle
\end{aligned} \tag{3.39}$$

$$\begin{aligned}
\Omega_3^{\text{hh-3N-3N-NN}} = \frac{1}{8} \sum_{\alpha\beta\gamma\delta\epsilon\phi} & n_\alpha n_\beta n_\gamma n_\delta \bar{n}_\epsilon \bar{n}_\phi \, F^{\alpha\beta,\epsilon\phi}_{\gamma\delta,\epsilon\phi} \left(\sum_\omega n_\omega \,\langle\alpha\beta\omega|\, \mathcal{A}_{123} V_{3N} \,|\epsilon\phi\omega\rangle \right) \\
& \times \langle\epsilon\phi|\, \mathcal{A}_{12} V_{NN} \,|\gamma\delta\rangle \,\langle\gamma\delta|\, \mathcal{A}_{12} V_{NN} \,|\alpha\beta\rangle
\end{aligned} \tag{3.40}$$

Other non-residual diagrams can be derived in a similar manner.

3.1.5 Diagrams included in our calculations

In our calculations we include the complete set of second-order contributions. In particular, we include the residual 3N contribution at second order [49, 64]. At third order we include all contributions that involve only NN interactions for our calculations of neutron matter in Chapter 5. Regarding the nonresidual third-order terms with 3N interactions, we have checked that their contribution in neutron matter is small compared to the corresponding diagrams containing only NN interactions. This is consistent with the findings of Ref. [49]. There are also residual 3N contributions at third order. Based on our results for the second-order residual term we expect them to be small, but this needs to be confirmed by explicit calculations. A more detailed study of the zero-temperature MBPT convergence including selected diagrams up to fourth order can be found in Ref. [49]. The convergence behavior of the expansion at finite

temperature is similar, with well-converged results for neutron matter being obtained at third order (e.g., for the EMN 450 N^3LO interaction, see Chapter 5, the truncation error at third order is at the 100 keV level at $n = 0.2\,\mathrm{fm}^{-3}$). For our calculations of asymmetric matter in Chapter 6 we furthermore include all non-residual 3N diagrams at 3rd order (that are obtained by replacing NN vertices with a self-contracted 3N vertex using Eq. (3.37)).

3.2 Free energy expansion

Usually we are interested in properties of the EOS at a specific number densities n_n and n_p. Thus, the relevant thermodynamic potential is the free energy, which is obtained from $\Omega(T, \mu_n, \mu_p)$ in terms of the Legendre transformation [7]

$$F(T, n) = \Omega(T, \mu_n, \mu_p) + \mu_n\, n_n(T, \mu_n, \mu_p) + \mu_p\, n_p(T, \mu_p, \mu_p)\,, \tag{3.41}$$

where the number densities are given by

$$n_n(T, \mu_n, \mu_p) = -\frac{\partial\Omega(T, \mu_n, \mu_p)}{\partial\mu_n}\,, \tag{3.42}$$

$$n_p(T, \mu_n, \mu_p) = -\frac{\partial\Omega(T, \mu_n, \mu_p)}{\partial\mu_p}\,. \tag{3.43}$$

The free energy determined from Eq. (3.41) and the perturbation series for $\Omega(T, \mu_n, \mu_p)$ up to a given order will in general not reproduce the corresponding zero-temperature perturbation series for the ground-state energy, see, e.g. Ref. [58]. This is because the zero-temperature formalism uses the Fermi momentum $k_{\mathrm{F},i}$ (or chemical potential of the reference system) whereas grand-canonical MBPT at finite temperature uses the exact chemical potential μ_i and has the additional anomalous contributions [58]. It is possible to use the grand-canonical perturbation series also at $T = 0$. However, to obtain a finite-temperature perturbation series that is consistent with the zero-temperature formalism, we use the method of Kohn and Luttinger [63] that is extended to a system that contains neutrons and protons as follows (for other finite-temperature calculations that employ this method, see, e.g., Refs. [17, 62]). We formally expand the chemical potentials as

$$\mu_n = \sum_{i=0}^{\infty} \lambda^n \mu_n^{(i)}\,, \tag{3.44}$$

$$\mu_p = \sum_{i=0}^{\infty} \lambda^n \mu_p^{(i)}\,, \tag{3.45}$$

where $\mu_\tau^{(0)}$ are the chemical potentials of the reference system with formally the same density as

the interacting system, i.e.,

$$n_n(T,\mu_n^0,\mu_p^0) = -\frac{\partial\Omega_0(T,\mu_n^{(0)}),\mu_p^{(0)}}{\partial\mu_n^0}\,, \tag{3.46}$$

$$n_p(T,\mu_n^0,\mu_p^0) = -\frac{\partial\Omega_0(T,\mu_n^{(0)}),\mu_p^{(0)}}{\partial\mu_p^0}\,. \tag{3.47}$$

By inserting the expansion Eq. (3.45) into Eq. (3.41) and reexpanding Ω and n around $\mu_n^{(0)}$ and $\mu_p^{(0)}$ we obtain

$$\Omega\left(T,\mu_n,\mu_p\right) = \sum_{n=0}^{\infty}\sum_{i=0}^{\infty}\sum_{j=0}^{\infty}\lambda^n\frac{(\mu_n-\mu_n^{(0)})^i}{i!}\frac{(\mu_p-\mu_p^{(0)})^j}{j!}\Omega_n^{(i,j)}(T)\,, \tag{3.48}$$

$$\Omega_n^{(i,j)}(T) = \partial_{\mu_n}^i\partial_{\mu_p}^j\;\Omega_n\left(T,\mu_n,\mu_p\right)\Big|_{\mu_n=\mu_n^{(0)},\mu_p=\mu_p^{(0)}}\,, \tag{3.49}$$

for the grand-canonical potential. Individual densities of neutrons and protons can also be expanded to

$$n_n(T,\mu_n,\mu_p) = -\partial_{\mu_n}\Omega(\mu_n,\mu_p) = \sum_{n=0}^{\infty}\sum_{i=0}^{\infty}\sum_{j=0}^{\infty}\lambda^n\frac{(\mu_n-\mu_n^{(0)})^i}{i!}\frac{(\mu_p-\mu_p^{(0)})^j}{j!}\Omega_n^{(i+1,j)}\,, \tag{3.50}$$

$$n_p(T,\mu_n,\mu_p) = -\partial_{\mu_p}\Omega(\mu_n,\mu_p) = \sum_{n=0}^{\infty}\sum_{i=0}^{\infty}\sum_{j=0}^{\infty}\lambda^n\frac{(\mu_n-\mu_n^{(0)})^i}{i!}\frac{(\mu_p-\mu_p^{(0)})^j}{j!}\Omega_n^{(i,j+1)}\,. \tag{3.51}$$

By requiring that individual densities agree with densities of the reference system (with $\mu_n^{(0)}$ and $\mu_p^{(0)}$), e.g. $n_n = n_n^0 = -\Omega_0^{(1,0)}$ and $n_p = n_p^0 = -\Omega_0^{(0,1)}$ higher orders can be determined recursively starting from reference potentials, e.g.

$$\mu_n^{(1)} = \frac{\Omega_0^{(1,1)}\Omega_1^{(0,1)} - \Omega_0^{(0,2)}\Omega_1^{(1,0)}}{(\Omega_0^{(1,1)})^2 - \Omega_0^{(0,2)}\Omega_0^{(2,0)}} \tag{3.52}$$

$$\mu_p^{(1)} = \frac{\Omega_0^{(1,1)}\Omega_1^{(1,0)} - \Omega_0^{(2,0)}\Omega_1^{(0,1)}}{(\Omega_0^{(1,1)})^2 - \Omega_0^{(0,2)}\Omega_0^{(2,0)}} \tag{3.53}$$

By inserting the expansion the free energy can be expressed as

$$\begin{aligned} F &= \Omega + \mu_n N_n + \mu_p N_p && (3.54)\\ &= \left(\Omega_0^{(0,0)} - \mu_n^{(0)}\Omega_0^{(1,0)} - \mu_p^{(0)}\Omega_0^{(0,1)}\right) && (3.55)\\ &+ \lambda\Omega_1^{(0,0)}\\ &+ \lambda^2\left(\Omega_2^{(0,0)} - F_2^a\right)\\ &+ \lambda^3\left(\Omega_3^{(0,0)} - F_3^a\right)\\ &+ \mathcal{O}\left(\lambda^4\right) \end{aligned}$$

where the correction terms at second and third order (due to the expansion around the reference system) are given by

$$F_2^a = \frac{1}{2}(\mu_n^{(1)})^2\Omega_0^{(2,0)} - \mu_n^{(1)}\mu_p^{(1)}\Omega_0^{(1,1)} - \frac{1}{2}(\mu_p^{(1)})^2\Omega_0^{(0,2)}\,, \tag{3.56}$$

$$F_3^a = \text{termes proportional to } \mu_n^{(1)} \text{ or } \mu_p^{(1)}\,. \tag{3.57}$$

The leading part $F_0 = \Omega_0^{(0,0)} - \mu_n^{(0)}\Omega_0^{(1,0)} - \mu_p^{(0)}\Omega_0^{(0,1)}$ is the free energy of the reference system. These expressions are obtained by fixing the higher-order contributions $\mu_\tau^{(i)}$ in Eq. (3.45) such that Eqs. (3.46) and (3.47) are maintained up to higher-order terms in the expansion of μ_τ about $\mu_\tau^{(0)}$.

For one-component isotropic systems it has been shown that the additional terms given by Eqs. (3.56), (3.57), etc., cancel the corresponding anomalous contributions in the $T \to 0$ limit [63, 65]. That is,

$$\Omega_l^{(0)}(T, \mu_n^{(0)}, \mu_p^{(0)}) - F_l^a(T, \mu_n^{(0)}, \mu_p^{(0)}) \xrightarrow{T\to 0} E_l^{(0)}(k_{\mathrm{F,n}}, k_{\mathrm{F,p}})\,, \tag{3.58}$$

where $E_l^{(0)}(k_{\mathrm{F,n}}, k_{\mathrm{F,p}})$ is the contribution of order l in zero-temperature MBPT, with neutron and proton Fermi momenta $k_{\mathrm{F,n}}$ and $k_{\mathrm{F,p}}$.

Note, that the evaluation of Eq. (3.55) only depends on the reference chemical potentials $\mu_n^{(0)}$ and $\mu_p^{(0)}$ (which are directly fixed by the densities n_n and n_p by using Eqs. (3.46) and (3.47)), but not on the exact chemical potentials μ_n and μ_p.

3.3 Self-consistent Hartree-Fock expansion

The calculations in this thesis are carried out using the generalization of HF-MBPT to finite temperatures. Compared to calculations with a noninteracting reference system, using a HF basis is expected to improve the convergence behavior of MBPT [49, 60, 66, 67]. The expression for the HF potential reads [60, 61]

$$U_\alpha = \sum_\beta n_\beta \langle\alpha\beta|\,\mathcal{A}_{12}V_{\mathrm{N}N}\,|\alpha\beta\rangle + \frac{1}{2}\sum_{\beta\gamma} n_\beta n_\gamma \langle\alpha\beta\gamma|\,\mathcal{A}_{123}V_{3N}\,|\alpha\beta\gamma\rangle\,. \tag{3.59}$$

This matches the expression for the first-order self-energy correction (see, e.g., Ref. [58] for the NN expression), as shown diagrammatically in Fig. 3.4. Note that while the evaluation of the HF potential in the zero-temperature formalism is straightforward (the expressions directly depend on the Fermi momenta and therefore on density), in the grand-canonical case it has to be computed self-consistently by solving

$$\varepsilon_\alpha(T, \mu_n, \mu_p) = \frac{k^2}{2m_\alpha} + U_\alpha[T, \mu_n, \mu_p; \varepsilon_\alpha(T, \mu_n, \mu_p)] \tag{3.60}$$

at fixed T, μ_n, and μ_p as the Fermi-Dirac distributions n_α depend on ε_α.

The chemical potential dependence of the potential U_α has to be fixed before the reexpansion

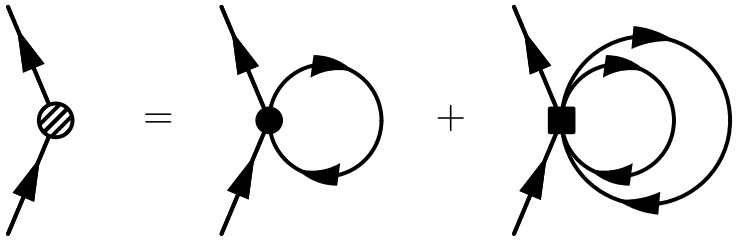

Figure 3.4: Definition of the single-particle potential U_α (left side) as the self-consistent Hartree-Fock self-energy. Solid dots (squares) represent $V_{\mathrm{N}N}$ (V_{3N}) interactions.

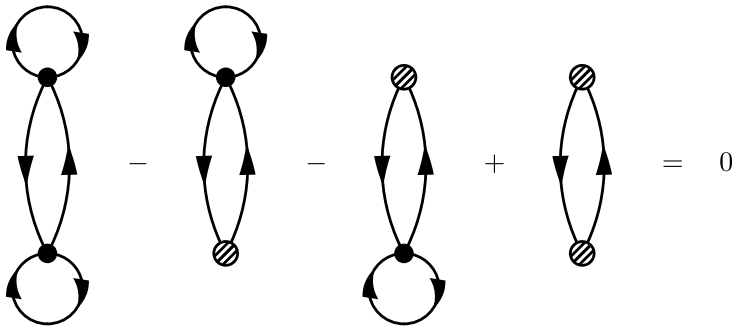

Figure 3.5: Cancellation of anomalous NN contributions at second order in Hartree-Fock MBPT at finite temperature. The diagrams correspond to Eqs. (3.25), (3.29), (3.30), and (3.31) in that order.

is performed (or the μ_n and μ_p dependence of U_α would lead to unwanted derivatives). To archive this, we substitute μ_n and μ_p by the reference chemical potentials $\mu_n^{(0)}$ and $\mu_p^{(0)}$, i.e.

$$U_\alpha(T, \mu_n, \mu_p) \longrightarrow U_\alpha(T, \mu_n^{(0)}, \mu_p^{(0)})\,, \tag{3.61}$$

before performing the reexpansion, such that U_α does not depend on μ_n and μ_p anymore.

Apart from improving the convergence of MBPT, the self-consistent HF potential has also the benefit that it removes all anomalous contributions associated with diagrams that have single-vertex loops [60]. In particular, it removes the anomalous contributions as well as the additional ones from the reexpansion about $\mu_\tau^{(0)}$ at second order [62] and third order. For the second-order anomalous contributions from two-body interactions, this cancellation is depicted diagrammatically in Fig. 3.5. The cancellation occurs because with our choice of U_α, the four diagrams of Fig. 3.5 give matching contributions up to an additional minus sign for the second and third diagram. Furthermore, with our U_α it is $\mu_n^{(1)} = \mu_p^{(1)} = 0$, which implies that the correction terms given by Eqs. (3.56) and (3.57) vanish, as they involve powers of $\mu_n^{(1)}$ and $\mu_p^{(1)}$. Hence, with U_α given by the self-consistent HF self-energy (incorporated as described above), the perturbation series for the free energy Eq. (3.55) simplifies to

$$F(T, \mu_n^{(0)}, \mu_p^{(0)}) = F_0 + \lambda\Omega_1^{(0)} + \lambda^2\Omega_{2,\mathrm{normal}}^{(0)} + \lambda^3\Omega_{3,\mathrm{normal}}^{(0)} + \mathcal{O}\big(\lambda^4\big)\,, \tag{3.62}$$

and the consistency with the zero-temperature formalism is evident (the subscript normal indicates that no anomalous diagrams are present at this order). Note, however, that new types

of anomalous contributions that are not canceled by the HF potential arise at fourth order and beyond [60].

4 Gaussian process

This chapter introduces Gaussian processes as a tool to interpolate EOS data points. We first give an overview of Gaussian processes, show how to include data points in the construction, demonstrate how derivatives can be calculated, and finally show how hyperparameters are determined.

4.1 Introduction

A Gaussian process (GP) is a collection of random variables

$$\{f(x) : x \in I\}, \tag{4.1}$$

with a continuous label $x \in I$ where e.g. $I = \mathbb{R}, \mathbb{R}^2$ or $\mathbb{R}^3$, see, e.g., Refs. [68, 69]. The random variables $f(x)$ are characterized by a covariance function (or kernel) $K(x, x')$ and a mean value $\mu(x)$ such that

$$\mu(x) = \mathbb{E}[f(x)]\,, \tag{4.2}$$

$$K(x, x') = \mathbb{E}[(f(x) - \mu(x))(f(x') - \mu(x'))]\,, \tag{4.3}$$

where $\mathbb{E}$ is the expectation value [68]. Furthermore for any finite amount of points from the index set $x_1, \ldots, x_n \in I$ the joined probability distribution function of the random variables $y_i = f(x_i)$ is a multivariate normal distribution [68, 69]

$$P(\{y_i\}_i|\{x_i\}_i) = \frac{1}{(2\pi)^{n/2}\det(\Sigma)^{1/2}} \exp\left(-\frac{1}{2}(\boldsymbol{y} - \boldsymbol{\mu})\Sigma^{-1}(\boldsymbol{y} - \boldsymbol{\mu})\right) \tag{4.4}$$

where the components of $\Sigma \in \mathbb{R}^{n\times n}$ and $\boldsymbol{\mu} \in \mathbb{R}^n$ are given by

$$\Sigma_{ij} = K(x_i, x_j)\,, \tag{4.5}$$

$$\mu_i = \mu(x_i). \tag{4.6}$$

The covariance function has to be chosen such that Σ is always a positive semi-definite matrix [68]. A typical choice is the square-exponential kernel [68]

$$K(x_1, x_2) = \sigma^2 \exp\left(-\frac{(x_1 - x_2)^2}{2l^2}\right) \tag{4.7}$$

that is parameterized by a overall scale σ and a length scale l. These hyperparameters determine

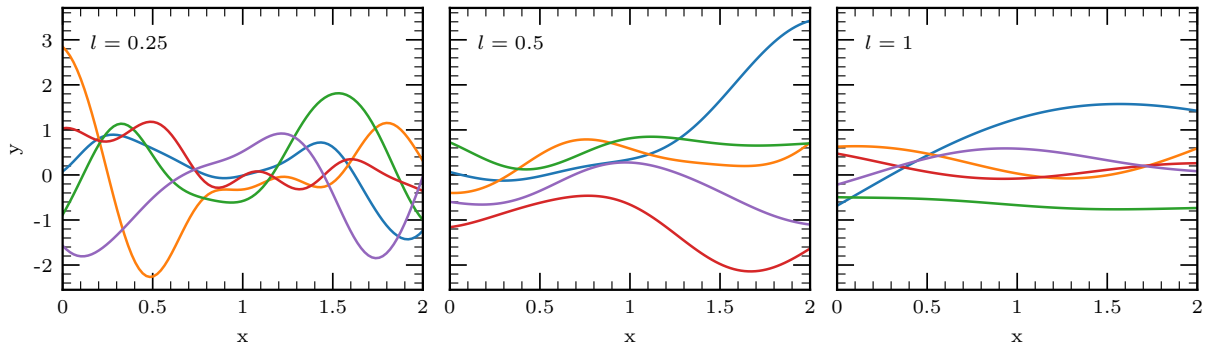

Figure 4.1: Samples drawn from Gaussian process (different colors) with mean $\mu = 0$ and square-exponential kernel for different length scales $l = 0.25, 0.5, 1$ (from left to right) and $\sigma = 1$.

the behavior of the Gaussian process. See Ref. [68] for a detailed discussion about other kernel choices.

Fig. 4.1 shows samples that are drawn from a GP with the square-exponential kernel for different values of l. The samples look like continuous functions. However as the plot in Fig. 4.1 (and usually any practical calculations) only depends on a finite amount of points $\{x_i\}_i$, the Gaussian process can be evaluated according to Eq. (4.4) by sampling from a multivariate normal distribution.

Note that the variance of the GP for this kernel is given by

$$\mathrm{Var}(x) = \mathbb{E}[(f(x) - \mu(x))^2] = \sigma^2 \,, \tag{4.8}$$

such that for $\sigma = 1$ almost all samples fall into the 96% interval $[-2, 2]$. Furthermore the covariance vanishes for two points x_1 and x_2 with $|x_1 - x_2| \gg l$, e.g.

$$\mathrm{Cov}(x_1, x_2) = \mathbb{E}[(f(x_1) - \mu(x_1))(f(x_2) - \mu(x_2))] \overset{|x-y|\gg l}{\approx} 0 \,, \tag{4.9}$$

such that points that are far apart (as measured by the length scale l) are uncorrelated. Finally the samples are smooth functions, this is a result of the kernel that is also smooth [68].

4.2 Adding data points

The samples in Fig. 4.1 are random curves distributed around zero. To use them for interpolation, they can be used as a prior distribution and Bayes theorem can applied to incorporate known data points [68, 69]. Given data points $\{x_i\}_i$ with known values $\{y_i\}_i$, we would like to find the distribution function of the values $\{y_i^*\}_i$ at positions $\{x_i^*\}_i$. Following Refs. [68, 69], training data points can be added as follows: By definition of the GP, the joined distribution function of $\{y_i\}_i$ and $\{y_i^*\}_i$

$$P(\{y_i\}_i, \{y_i^*\}_i | \{x_i\}_i, \{x_i^*\}_i) \tag{4.10}$$

is given by Eq. (4.4) as a normal distribution, where the matrix Σ is given by

$$\Sigma = \begin{pmatrix} A & B \\ B^T & C \end{pmatrix} \tag{4.11}$$

and the elements of the submatrices A, B, C, and D are given by

$$A_{ij} = K(x_i, x_j) + \delta_{ij}\sigma^2\,, \tag{4.12}$$
$$B_{ij} = K(x_i, x_j^*)\,, \tag{4.13}$$
$$C_{ij} = K(x_i^*, x_j^*)\,. \tag{4.14}$$

where σ was added to account for normally distributed noise of the training data [68]. The conditional distribution $P(\{y_i^*\}_i|\{x_i\}_i, \{y_i\}_i, \{x_i^*\}_i)$ is also a normal distribution with updated mean vector μ^* and covariance matrix Σ^* given by [68, 69]

$$\mu^* = B^T A^{-1} \boldsymbol{y}\,, \tag{4.15}$$
$$\Sigma^* = C - B^T A^{-1} B\,. \tag{4.16}$$

The conditional distribution of a Gaussian process is again a Gaussian process with updated mean and covariance function [68, 69]. Note that for $x^* = x$ and $\sigma = 0$ this results in

$$\boldsymbol{\mu}^* = \boldsymbol{y}\,, \tag{4.17}$$
$$\Sigma^* = 0\,, \tag{4.18}$$

such that the GP interpolates all training data points by construction.

This is illustrated in Fig. 4.2 where the posterior distribution is shown for different values of the length scale l together with the 1σ and 2σ uncertainty bands. Note that the mean (black) line passed exactly through all data points and that the uncertainties vanish close to the training points. Between data points, the GP is less constrained and the predicted uncertainty increases. The size of the uncertainty is determined by how correlated nearby points are and can be chosen by the kernel function (by changing the length scale and the overall scale in the radial basis functions used here).

4.3 Calculating derivatives

The derivative (or in general any linear transformation) of a Gaussian process is again a Gaussian process [68]. The joined distribution of a GP with its derivative can be constructed as [56]

$$\begin{pmatrix} f(x) \\ \partial_x f(x) \end{pmatrix} \sim GP\left(\begin{pmatrix} m(x) \\ \partial_x m(x) \end{pmatrix}, \begin{pmatrix} K(x,x) & \partial_{x_*} K(x, x_*) \\ \partial_x K(x_*, x) & \partial_x \partial_{x_*} K(x_*, x_*) \end{pmatrix}\right) \tag{4.19}$$

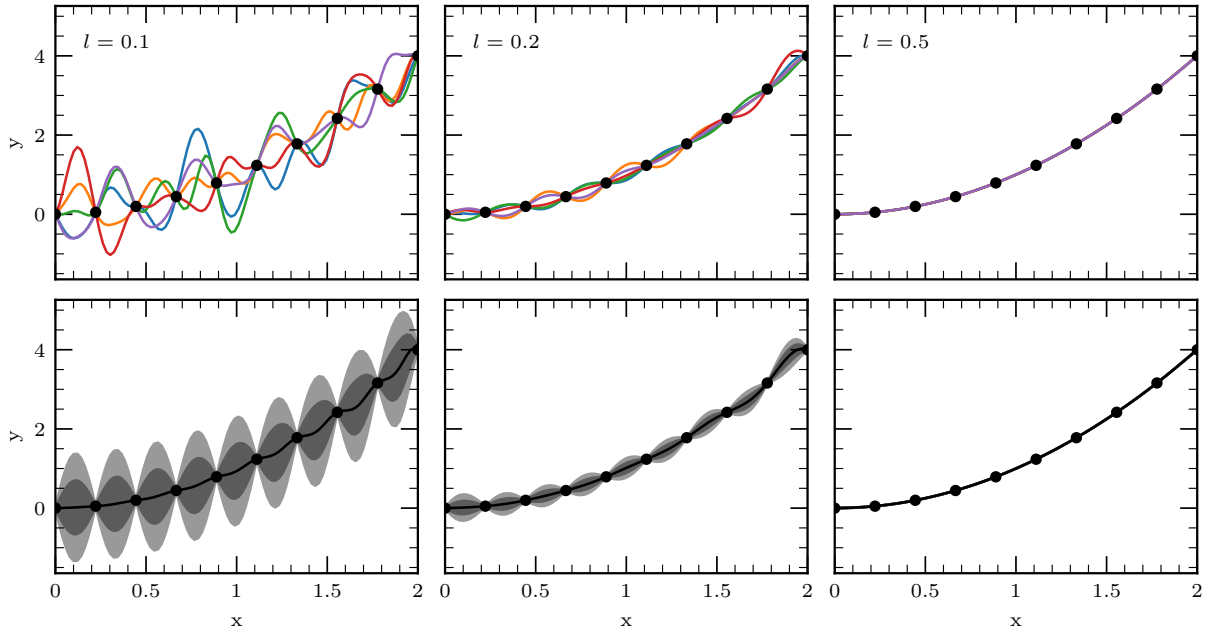

Figure 4.2: Samples drawn from a Gaussian process (upper panels) with known data points (black dots). Different length scales l are shown in the panels from left to right. Lower panels show the mean value together with the 1σ (dark gray) and 2σ (light gray) uncertainty bands.

where the mean function and kernel are given by

$$\boldsymbol{\mu} = \begin{pmatrix} m(x) \\ \partial_{x^*} m(x^*) \end{pmatrix} \tag{4.20}$$

$$\Sigma = \begin{pmatrix} K(x,x) & \partial_{x_*} K(x,x_*) \\ \partial_x K(x_*,x) & \partial_x \partial_{x_*} K(x_*,x_*) \end{pmatrix} \tag{4.21}$$

and we have used the linearity of the expectation value, e.g.

$$\mathbb{E}[(\partial_x f(x) - \partial_x \mu(x))(f(x') - \mu(x'))] = \partial_x \mathbb{E}[(f(x) - \mu(x))(f(x') - \mu(x'))] = \partial_x K(x,x')\,. \tag{4.22}$$

To add data points, the same method as in Sec. 4.2 can be used. See Refs. [56, 68] for more details.

4.4 Determining the hyperparameters

So far the resulting GP prediction depends on the value of the hyperparameters that are used. Ideally they would be integrated out to obtain predictions that are independent of them [68, 69]

$$P(y^*|x^*, \{x_n\}_n, \{y_n\}_n) = \int P(y^*|x^*, \{x_n\}_n, \{y_n\}_n, \theta) P(\theta|\{x_n\}_n, \{y_n\}_n) \mathrm{d}\theta\,, \tag{4.23}$$

where $P(\theta|\{x_n\}_n, \{y_n\}_n)$ is the posterior distribution of the hyperparameters given the data points. Note that the posterior distribution Eq. (4.23) does not need to be a Gaussian process [69]. The integral can be approximated by using the maximum of the hyperparameter posterior [68, 69]

$$P(y^*|x^*, \{x_n\}_n, \{y_n\}_n) \approx P(y^*|x^*, \{x_n\}_n, \{y_n\}_n, \theta_{\max}) \tag{4.24}$$

where $\theta_{\max}$ is the maximum of the posterior distribution

$$P(\theta|\{x_n\}_n, \{y_n\}_n) = \frac{P(\{y_n\}_n|\{x_n\}_n, \theta)P(\theta)}{P(\{x_n\}_n, \{y_n\}_n)} \tag{4.25}$$

and $P(\theta)$ is the prior distribution of the hyperparameters θ. Assuming that the prior $P(\theta)$ is uniform $\theta_{\max}$ can be obtained by maximizing the likelihood

$$P(\{y_n\}_n|\{x_n\}_n, \theta) \tag{4.26}$$

which is given by the Gaussian process.

4.5 Gaussian processes in this thesis

The calculations of the free energy per particle $F(n, x, T)/A$ as a function of density n, proton fraction x and temperature T is a computationally involved task. Evaluations of every point (n, x, T) involves the numerical calculation of several high dimensional integrals (see Chapter 3) and therefore has to be limited to evaluation on a grid. GPs are used to interpolate the grid points to a smooth free energy function and to calculate the partial derivatives (like pressure or chemical potentials). They allow to incorporate the residual noise of the Monte Carlo integration employed. Furthermore, by construction, they lead to second-order mixed partial derivative that are commuting, despite the noise of the grid points.

GPs are used in Chapters 6, 7, 8, and 9.

5 Neutron matter at finite temperature

In this Chapter we first explore the EOS of neutron matter at finite temperature which, compared to symmetric nuclear matter or matter with finite asymmetries, is a simpler many-body system. This Chapter has already been published in Ref. [59] together with Corbinian Wellenhofer. I have performed all calculations presented here.

While nuclear matter at zero temperature has been investigated quite extensively based on chiral EFT interactions [49, 61, 70–80], studies at finite temperature are less advanced. This is an unsatisfying situation as, e.g., recent core-collapse supernova simulations have demonstrated the importance of a proper treatment of finite-temperature effects in the EOS [36, 81]. In neutron star merger simulations, thermal effects are sometimes approximated via a constant thermal index (see, e.g., Ref. [82]). The availability of microscopic calculations over the full range of relevant temperatures would make such approximations obsolete, at least up to densities where nuclear interactions are applicable and reliable. For recent work that implements chiral EFT constraints into EOS functionals, with a focus on thermal effects, see Ref. [83].

Nuclear matter at finite temperature has been studied with a range of many-body methods. In addition to calculations using the Brueckner-Hartree-Fock approach [84] and nominally variational calculations [85], the finite-temperature EOS has been calculated using many-body perturbation theory (MBPT) [11, 17, 62, 86, 87], and nonperturbatively using the self-consistent Green's function (SCGF) approach [73, 88–90] and lattice EFT [91].

In this Chapter, we take several steps towards improved finite-temperature MBPT calculations. For an efficient evaluation of individual diagrams, we represent NN and 3N interactions in a single-particle representation following the framework of Ref. [49] and employ Monte Carlo sampling techniques to reliably compute the resulting high-dimensional MBPT phase space integrals in an efficient way. We treat 3N interactions explicitly, without employing density-dependent two-body approximations (see, e.g., Refs. [61, 92]). Moreover, we include NN and 3N interactions through partial-wave decomposed matrix elements [44, 50], which enables MBPT calculations for general nuclear forces. To provide systematic uncertainty estimates, we employ a large set of chiral NN plus 3N interactions at different orders in the chiral expansion up to $\mathrm{N^3LO}$. We take into account all contributions of NN interactions up to third-order in the MBPT expansion around the self-consistent Hartree-Fock (HF) solution, which implicitly includes contributions from anomalous diagrams at second and third order in MBPT. Finally, we provide a detailed analysis of thermal interaction effects and to which extent they can be approximated by a density-dependent effective mass and a thermal index, which is of interest for astrophysical applications.

We use the MBPT framework at finite temperature as discussed in Chapter 3. See Chapter 3

in particular for the role of anomalous contributions and the simplifications when using a HF partitioning of the Hamiltonian. In Sec. 5.1 we discuss the details of the calculational setup and in Sec. 5.2 we present results for various thermodynamic quantities and their uncertainties based on different nuclear interactions obtained from chiral EFT up to N^{3}LO. Moreover, we study the different contributions to thermal effects, and use the thermal index to extract the neutron effective mass.

5.1 Calculational setup

In this Chapter we present a systematic study of the neutron matter EOS based on different nuclear interactions obtained from chiral EFT. First, we employ the NN potentials of Entem, Machleidt, and Nosyk (EMN) [52] with cutoffs $\Lambda = 450\,\mathrm{MeV}$ and $\Lambda = 500\,\mathrm{MeV}$ at orders N^{2}LO and N^{3}LO. Three-nucleon interactions are included up to the same order in the chiral expansion as two-nucleon interactions, using nonlocal regulators with the same cutoff Λ [49]. Note that the N^{2}LO 3N contributions from the mid- and short-range couplings c_D and c_E vanish in neutron matter for nonlocal regulators [61], and hence our results are independent of the particular c_D, c_E fits for all employed interactions in this work.[1] To explore the cutoff dependence we show the variation from $\Lambda = 450\,\mathrm{MeV}$ to $\Lambda = 500\,\mathrm{MeV}$ as a band with borders labeled "EMN N^{2}LO" or "EMN N^{3}LO", respectively. These interactions were studied in Ref. [49] up to fourth order in the zero-temperature MBPT expansion, which provides a benchmark for our calculations.

Second, to improve the convergence of the MBPT calculations, we apply the similarity renormalization group (SRG) [48] to decouple low and high momenta via unitary transformations. The resulting low-resolution interactions lead to less correlated wave functions and can lead to a significantly improved convergence of many-body calculations [93]. (Note, however, that unevolved EMN interactions are still sufficiently perturbative to be applicable for the neutron matter calculations presented here.) In practical calculations the SRG flow cannot be computed exactly but needs to be truncated, typically by discarding all induced operators beyond the three-body level (see, e.g., Refs. [94–97]). The Hebeler+ interactions of Ref. [70] are derived by evolving the N^{3}LO NN potential of Ref. [98] to resolution scales λ_{SRG}, while the 3N interactions at N^{2}LO are determined at the corresponding resolution scale by fits to the ^{3}H binding energy and the ^{4}He radius using the cutoff Λ_{3N}. In Ref. [70], different NN+3N interactions were derived, each characterized by $\lambda_{\mathrm{SRG}}/\Lambda_{\mathrm{3N}}$. In this work we in particular employ the interactions "1.8/2.0", "2.8/2.0", "2.0/2.5" and "2.0/2.0 (PWA)", where for the last a different set of long-range 3N couplings has been used (see Ref. [70] for details). Finally, we also employ new interactions from Ref. [44], where NN+3N interactions are consistently SRG evolved to scales λ_{SRG} using the framework of Ref. [99]. For all interactions, we include NN partial waves up to total angular momentum $J_{12} \leqslant 8$. Three-nucleon partial waves are included up to $J_{\mathrm{tot}} \leqslant 9/2$ and $J_{12} \leqslant 5$ or 6 for SRG-evolved and EMN interactions, respectively. We have checked that these truncations give converged results below the 100-keV level. All nuclear interactions (including the SRG

[1] Note that three-body contributions proportional to c_4 are absent as well in pure neutron matter for all regulators [61].

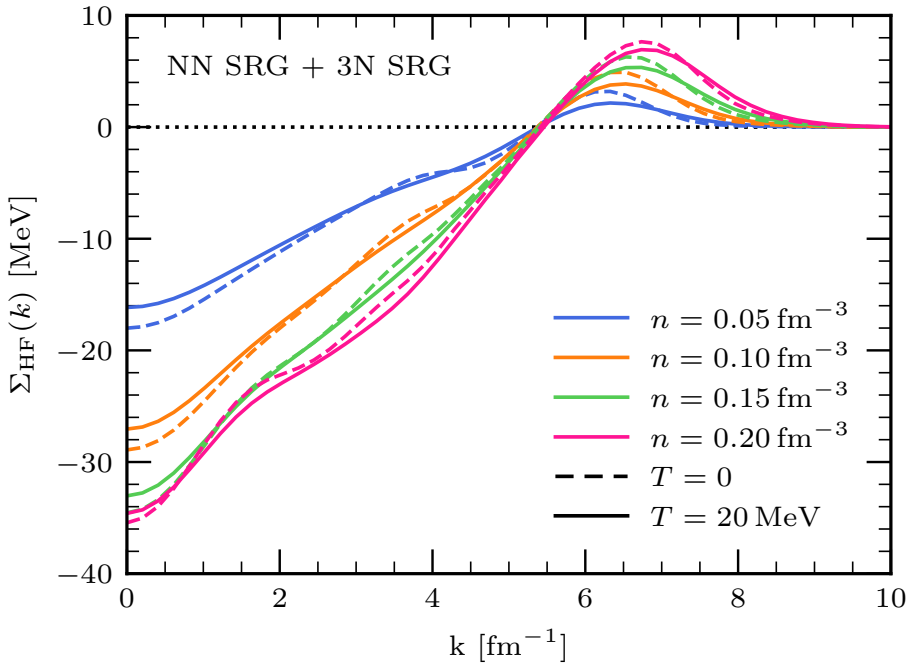

Figure 5.1: Self-consistent Hartree-Fock self-energy $\Sigma_{HF}(k)$ as a function of momentum k at temperatures $T = 0$ (dashed) and $T = 20\,\mathrm{MeV}$ (solid lines) for different densities, obtained from the consistently SRG-evolved NN+3N interaction with $\lambda_{\mathrm{SRG}} = 1.8\,\mathrm{fm}^{-1}$.

evolution) have been provided by Ref. [51] in partial-wave decomposed form (see Chapter 2).

To test the sensitivity to the SRG resolution scale λ_{SRG}, we show the variation from $\lambda_{\mathrm{SRG}} = 1.8\,\mathrm{fm}^{-1}$ to $\lambda_{\mathrm{SRG}} = 2.8\,\mathrm{fm}^{-1}$ as bands with borders labeled "NN SRG + 3N fit" for the Hebeler+ interactions (with $\Lambda_{3N} = 2.0\,\mathrm{fm}^{-1}$) and "NN SRG + 3N SRG" for the consistently evolved interactions. The cutoff and SRG scale variations are only one source of uncertainty. Uncertainty estimates based on the convergence of the EFT expansion are studied in Sec. 5.3 and are depicted in Figs. 5.7 and 5.9 as bands without borders.

For all results in the following we employ a HF partitioning of the Hamiltonian. Therefore, we first show the HF self-energy $\Sigma_{\mathrm{HF}}(k)$ in Fig. 5.1 for different densities at $T = 0$ and $T = 20\,\mathrm{MeV}$. Here and in the following we use $T = 10^{-3}\,\mathrm{MeV}$ to obtain zero-temperature results with our finite-temperature code. We have checked that using even lower temperatures does not change the results and verified that our $T = 10^{-3}\,\mathrm{MeV}$ results can reproduce zero-temperature results from Ref. [49] very well. The expression for the HF self-energy is given by Eq. (3.59). Note that Fermi-Dirac distribution functions n_β depend on the self-energy, such that a self-consistent solution is necessary, in contrast to zero-temperature calculations. We start with a free spectrum and iterate Eq. (3.60) until convergence is reached. The self-consistent HF self-energy is more conveniently obtained by working at fixed density; i.e., we perform the self-consistent iterations of Eq. (3.60) while adjusting at each iteration step μ_0 (resp. $\tilde{\mu}$, see Sec. 3.3) to n according to Eq. (3.47).

The results shown in Fig. 5.1 are for the "NN SRG + 3N SRG" interaction at $\lambda_{\mathrm{SRG}} = 1.8\,\mathrm{fm}^{-1}$. We find that the self-energy is mainly attractive up to high momenta around $k \approx 6\,\mathrm{fm}^{-1}$.

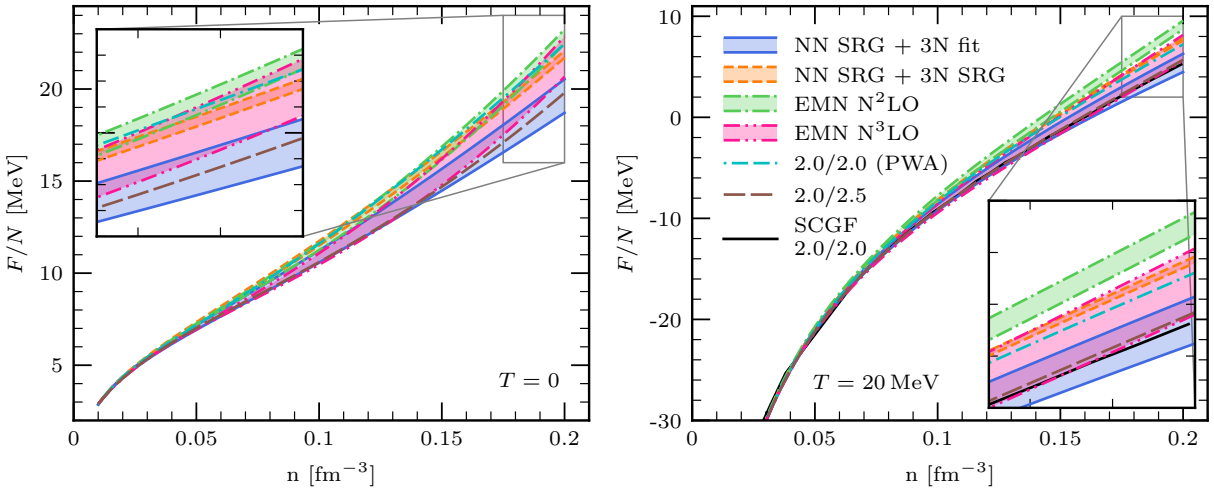

Figure 5.2: Free energy per particle, F/N, as function of the density n at $T = 0$ (left) and $T = 20\,\mathrm{MeV}$ (right panel) for different chiral interactions. Bands display variations of the SRG scale from $\lambda_{\mathrm{SRG}} = 1.8\,\mathrm{fm}^{-1}$ to $\lambda_{\mathrm{SRG}} = 2.8\,\mathrm{fm}^{-1}$ for both sets of SRG-evolved interactions, while for the EMN interactions they display the cutoff variations from $\Lambda = 450\,\mathrm{MeV}$ to $\Lambda = 500\,\mathrm{MeV}$. Results for the interactions "2.0/2.5" and "2.0/2.0 (PWA)" are shown as individual lines. See the text for more details about the interactions. The insets display the density range from $n = 0.175\,\mathrm{fm}^{-3}$ to $n = 0.2\,\mathrm{fm}^{-3}$.

Three-particle interactions yield repulsive net contributions for momenta $k \lesssim 5\,\mathrm{fm}^{-1}$ while the temperature dependence of the results is remarkably small. At the highest density shown ($n = 0.2\,\mathrm{fm}^{-3}$), the NN contribution to the self-energy is $-69.1\,\mathrm{MeV}$ while 3N contributions yield $33.7\,\mathrm{MeV}$ for $k = 0$ and $T = 0$. For very high momenta ($k \gtrsim 10\,\mathrm{fm}^{-1}$), the self-energy vanishes due to the employed regulators for the NN and 3N interactions.

5.2 Free energy, pressure, and entropy

The free energy is calculated within MBPT using the formalism discussed in Chapter 3. We include contributions from NN interactions up to third order, while we neglect 3rd order diagrams involving 3N interactions. Momentum integrals in the individual diagrams are evaluated using the Vegas integration algorithm from Ref. [100] where we take the implementation from Ref. [101] (see also Ref. [49]).

In Fig. 5.2 we present results for the free energy per particle for $T = 0$ (left) and $T = 20\,\mathrm{MeV}$ (right panel). The different bands (and lines) correspond to different interactions, and the bands result from variations of the interaction cutoff scale and the SRG resolution scale (see legend and the previous section for details). Lines at the borders of bands always represent results for one of the Hamiltonians in that given set. Theoretical uncertainty estimates based on the EFT expansion are provided in Sec. 5.3.

While our results at low densities are almost insensitive to the interactions considered, differences emerge with increasing density. In particular, the size of the cutoff variation bands

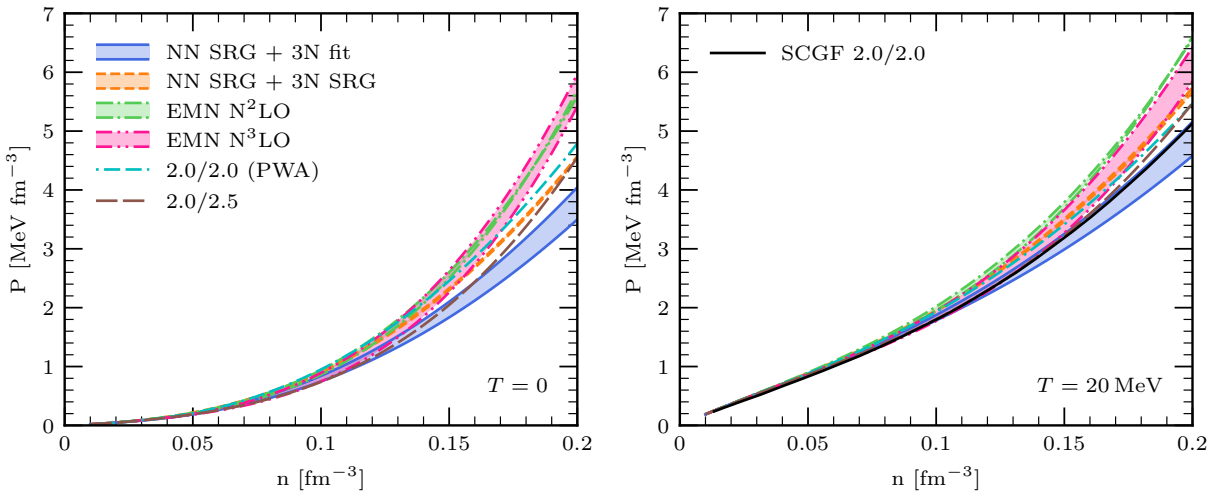

Figure 5.3: Pressure P as function of the density n at $T = 0$ (left) and $T = 20\,\mathrm{MeV}$ (right) for different chiral interactions. For details on how the bands are constructed for the different interactions see the caption of Fig. 5.2 and the text. The density derivative $P = n^2\partial_n(F/N)$ has been calculated analytically by first fitting the results for the interaction free energy F_{int} via Eq. (5.4) while treating the free gas contribution analytically (see text for details).

increases, as expected. We note that the cutoff dependence of the EMN N^{3}LO interactions is larger than for N^{2}LO in our calculation. This could be due to a slower MBPT convergence at N^{3}LO. Furthermore, we find that the SRG scale dependence of the "NN SRG + 3N fit" interactions is comparable to the cutoff sensitivity of the EMN interactions, while the variation of the results for the consistently evolved "NN SRG +3N SRG" interactions is much smaller, only about 400 keV at $n = 0.2\,\mathrm{fm}^{-3}$ for $T = 0$. This indicates that effects from neglected four- and higher-body forces in the SRG evolution are very small for neutron matter in this resolution scale regime (see also Ref. [44]), and that higher-order MBPT contributions are likely small.

We determine the pressure as the density derivative of the free energy, i.e.,

$$P = n^2 \frac{\partial}{\partial n} \left.\frac{F}{N}\right|_T . \tag{5.1}$$

At finite temperature the free energy per particle diverges logarithmically in the zero-density limit (see, e.g., Ref. [17]). This is a result of the free Fermi gas contribution and is also present without interactions. To evaluate Eq. (5.1) accurately, we separate the free Fermi gas contribution, which is treated exactly, and differentiate numerically only the interaction free energy,

$$F_{\mathrm{int}}(T,n) = F_{\mathrm{FG}}(T,n) - F(T,n)\,. \tag{5.2}$$

(Note that for convenience we define the interaction free energy F_{int} as the negative of $F - F_{\mathrm{FG}}$.) The pressure is then expressed as

$$P(T,n) = P_{\mathrm{FG}}(T,n) - n^2 \frac{\partial}{\partial n} \left.\frac{F_{\mathrm{int}}(T,n)}{N}\right|_T , \tag{5.3}$$

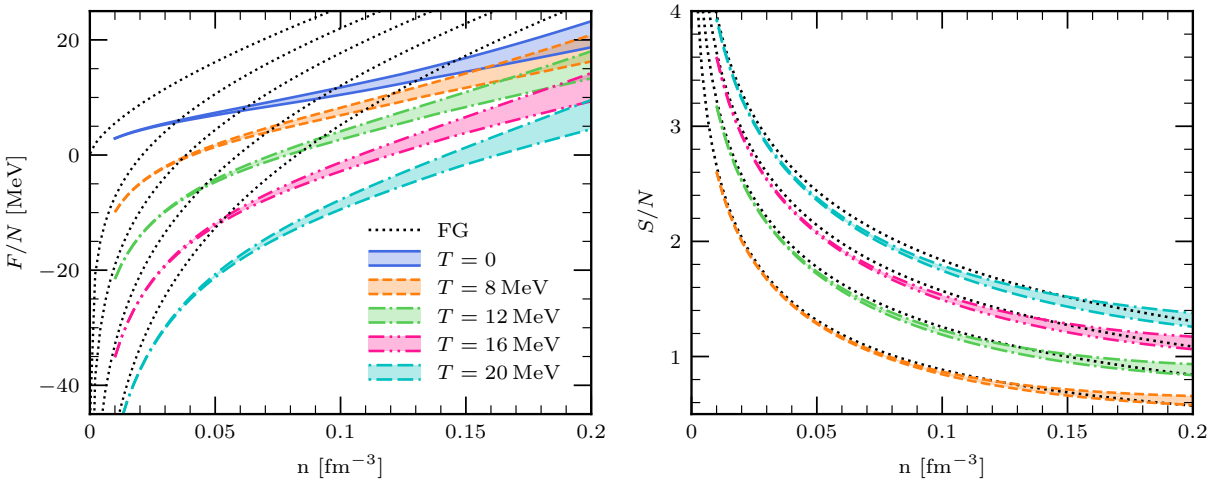

Figure 5.4: Free energy per particle, F/N (left), and entropy per particle, S/N (right), for $T = 0, 8, 12, 16$, and 20 MeV as a function of density n. The free Fermi gas (FG) is shown as a dotted line. Bands for the free energy are determined by taking the minimum and maximum value of the bands shown in Fig. 5.2 and the same procedure is applied for the entropy. Note that the divergence of the free energy per particle for vanishing density originates from the free Fermi gas contribution.

where the pressure of the free gas $P_{\mathrm{FG}}(T, n)$ can be evaluated using polylogarithms. To evaluate the interaction contribution to the pressure, we employ a fit function and calculate the derivative of the fit analytically. We use the function from Ref. [102],

$$\frac{F_{\mathrm{int}}(T,n)}{N} = a_0(T) + \sum_{i=1}^{4} a_i(T) \left(\frac{n}{n_0}\right)^{\frac{i+1}{3}} , \tag{5.4}$$

with saturation density $n_0 = 0.16\,\mathrm{fm}^{-3}$ to set the scale. We also checked that the simpler function $F_{\mathrm{int}}/N = a\,(n/n_0)^{\alpha} + b\,(n/n_0)^{\beta}$ yields similar results, but with worse fit quality. The results for the pressure are shown in Fig. 5.3. They demonstrate that the model dependence is increased compared to the free energy, as expected for a quantity obtained through a derivative.

To obtain a better insight into the temperature dependence of the EOS, we show the free energy per particle for $T = 0, 8, 12, 16$, and 20 MeV as a function of density in the left panel of Fig. 5.4. For comparison we also show the free energy of the free Fermi gas. Here, for each temperature the respective band combines the individual bands from the different interaction sets shown in Fig. 5.2. The width of the bands increases with increasing density in a comparable way for all temperatures. This reflects the fact that the shift of F for different temperatures is mainly caused by the free Fermi gas contribution; i.e., the temperature dependence of the interaction contribution is small by comparison. The temperature dependence is investigated in more detail in Sec. 5.4.

Finally, we calculate the entropy per particle, $S/N = -\partial_T F/N|_n$, via

$$S(T,n) = S_{\mathrm{FG}}(T,n) + \frac{\partial}{\partial T} F_{\mathrm{int}}(T,n)\bigg|_n , \tag{5.5}$$

where again the free gas contribution is treated analytically and the interaction contribution is evaluated by employing a fit function. The results are shown in the right panel of Fig. 5.4. The entropy is dominated by the free gas contribution $S_{\rm FG}$, which is a direct consequence of the weak temperature dependence of $F_{\rm int}$ (see also Fig. 5.8 and corresponding discussion). As a consequence, the entropy also exhibits only a very weak sensitivity to the employed Hamiltonian.

5.3 Chiral expansion

Chiral EFT provides a formal expansion in powers of

$$Q = \frac{p}{\Lambda_b}\,, \tag{5.6}$$

where p is the relevant momentum scale for the observable of interest and Λ_b the breakdown scale of the EFT. To further investigate the interaction uncertainties, we first show in Fig. 5.5 the free energy per particle for different orders in the chiral EFT expansion (LO, NLO, N^{2}LO, and N^{3}LO, corresponding to different orders Q^0, Q^2, Q^3, and Q^4 in the NN+3N interactions). The narrow bands show the cutoff variation from $\Lambda = 450\,\text{MeV}$ to $\Lambda = 500\,\text{MeV}$. The convergence of the chiral expansion is evident in Fig. 5.5 as the relative contributions get consistently smaller with increasing chiral order. The only exception is the N^{2}LO contribution which is larger than the NLO contribution at densities around $n \approx 0.2\,\text{fm}^{-3}$. This is a result of 3N interactions, which start to contribute at N^{2}LO. These give a repulsive contribution which becomes sizable for $n \gtrsim 0.1\,\text{fm}^{-3}$ (see the qualitative difference between the NLO and N^{2}LO results shown in Fig. 5.5).

The convergence of the chiral expansion at finite temperature is examined in Fig. 5.6 where we plot the uncertainty bands for the interaction free energy $F_{\rm int} = F_{\rm FG} - F$ as a function of density at the different chiral orders for $T = 0$ (left) and $T = 20\,\text{MeV}$ (right). Obviously, the convergence behavior is similar at $T = 0$ and at finite temperature. This again reflects the fact that the dominant part of the temperature dependence corresponds to the free gas contribution. For example, the shift $F_{\rm int}(T = 20\,\text{MeV}) - F_{\rm int}(T = 0)$ is only about $1\,\text{MeV}$ at $n = 0.2\,\text{fm}^{-3}$, while the shift of the free gas contribution is $-13.8\,\text{MeV}$ (see also Fig. 5.8).

A crucial asset of the EFT expansion is the possibility to estimate errors associated with the truncation of the expansion at a finite order. Following Refs. [53, 54] we estimate the uncertainty of an observable $X(p)$ in the following way:

$$\Delta X^{(j)} = Q \cdot \max\Big\{\big|X^{(j)} - X^{(j-1)}\big|, \Delta X^{(j-1)}\Big\}\,, \tag{5.7}$$

where $X^{(j)}$ denotes the observable calculated from interactions up to order N^{j}LO. To apply this prescription to the EOS of neutron matter at a specific density n, we follow Ref. [49] and choose the breakdown scale in Eq. (5.6) equal to $\Lambda_b = 500\,\text{MeV}$ and the momentum scale equal to $p = \sqrt{3/5}\,k_{\rm F}$, with $k_{\rm F} = (3\pi^2 n)^{1/3}$ the zero-temperature Fermi momentum.

Note that for our uncertainty estimates we omit the leading-order (LO) error. The estimate

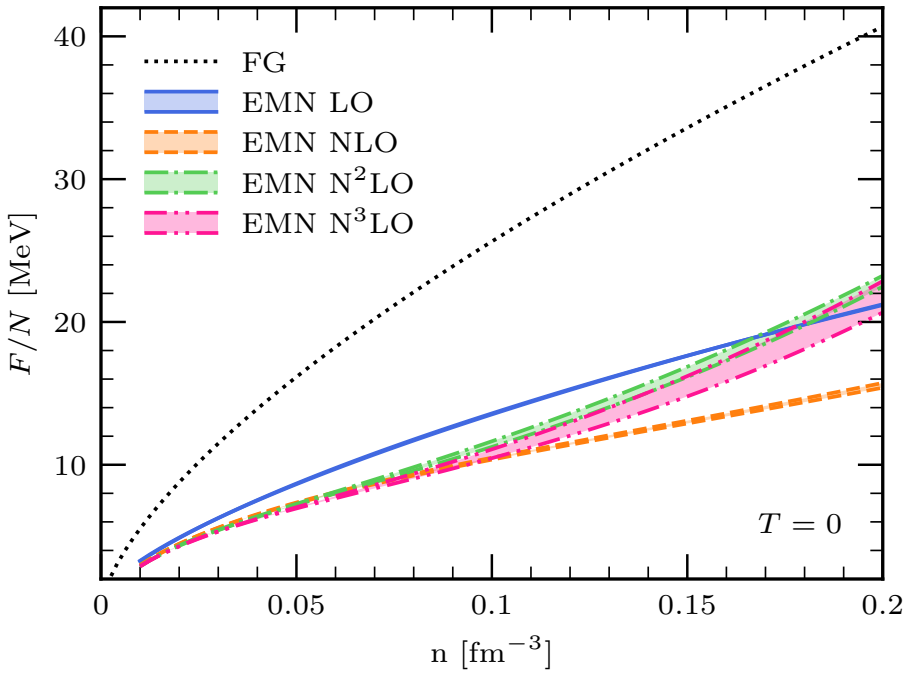

Figure 5.5: Free energy per particle, F/N, for $T = 0$ as a function of density n for the EMN interaction at different chiral orders (LO, NLO, N^{2}LO, and N^{3}LO). Bands display the cutoff variation from $\Lambda = 450\,\mathrm{MeV}$ to $\Lambda = 500\,\mathrm{MeV}$. The free Fermi gas (FG) is shown as a dotted line.

$\Delta X^{\mathrm{LO}} = Q^2 |X^{\mathrm{LO}}|$ is problematic in the present context in several ways. First, at nonzero temperature there exists a finite density at which the free energy has a zero crossing, resulting in vanishing errors. Second, at low densities the free energy per particle at finite temperature is dominated by the free gas contribution, and clearly the corresponding enhancement of ΔX^{LO} is unwarranted. These two features could be amended by separating the noninteracting (free Fermi gas) contribution, i.e., by using $\Delta X^{\mathrm{LO}} = Q^2 |X^{\mathrm{LO}} - X^{\mathrm{FG}}|$ instead. However, we regard it as a clearer strategy to omit the LO error as well as the LO contribution at higher orders in Eq. (5.7).

Recently a new Bayesian framework for estimating correlated EFT truncation errors based on Gaussian processes (GP-B) was introduced in Refs. [16, 56]. To provide an alternative error estimate, we apply their publicly available code [103] using $p = k_{\mathrm{F}}$ and $\Lambda_b = 600\,\mathrm{MeV}$ (see Ref. [16]). A comparison of the prescription by Epelbaum, Krebs, and Meißner (EKM), Eq. (5.7), to the GP-B estimate (68% credible interval) is shown in Fig. 5.7 for the free energy (left) and pressure (right). The EKM prescription Eq. (5.7) provides slightly larger error estimates, but overall both methods give very similar uncertainty bands.

5.4 Thermal interaction effects

Next, we explore thermal effects of the interaction contributions to the EOS. First, in Fig. 5.8 we examine the interaction free energy $F_{\mathrm{int}} = F_{\mathrm{FG}} - F$ as a function of temperature for different densities. The results show that the temperature dependence of F_{int} is very small for all con-

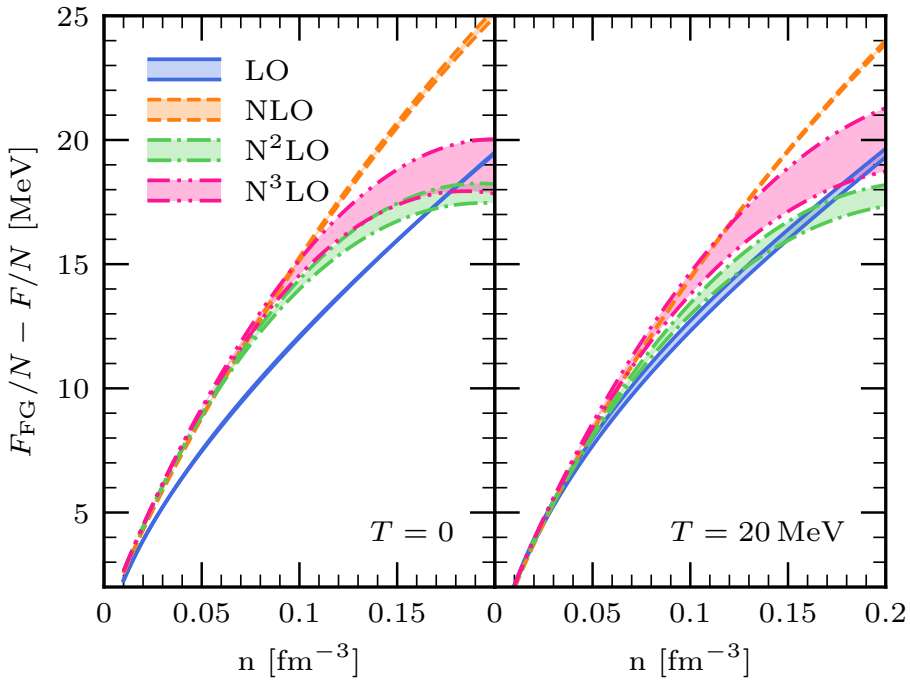

Figure 5.6: Interaction free energy per particle, $F_{\rm int}/N = F_{\rm FG}/N - F/N$, for $T = 0$ (left) and $T = 20\,\text{MeV}$ (right) as a function of density n for the EMN interaction (see Fig. 5.5 for details and the definition of the bands).

sidered densities, as noted above. To characterize thermal interaction effects in more detail we define the thermal part of a given thermodynamic quantity $X(T,n)$ as the difference between finite-temperature and zero-temperature value (see, e.g., Ref. [104]), i.e.,

$$X_{\rm th}(T,n) = X(T,n) - X(T=0,n)\,. \tag{5.8}$$

From the thermal components of the pressure and internal energy density one obtains a very useful quantity that characterizes thermal effects, the so-called thermal index $\Gamma_{\rm th}$ (see, e.g., Ref. [104]):

$$\Gamma_{\rm th}(T,n) = 1 + \frac{P_{\rm th}(T,n)}{\mathcal{E}_{\rm th}(T,n)}\,, \tag{5.9}$$

where $\mathcal{E}_{\rm th} = E_{\rm th}/V$ is the thermal energy density. The free Fermi gas has $\Gamma_{\rm FG,th} = 5/3$ (see Eq. (5.11)) independent of density and temperature. Any deviations of $\Gamma_{\rm th}(T,n)$ from 5/3 is thus due to thermal interaction effects. The thermal index is often used to parametrize the temperature dependence of nuclear EOS used in astrophysical simulations [82, 105], where a constant $\Gamma_{\rm th}$ independent of T and n (e.g., $\Gamma_{\rm th} = 1 - 2$) is sometimes adopted.

Our results for the thermal energy (top), the thermal pressure (middle) and the thermal index (bottom) at $T = 20\,\text{MeV}$ are displayed in Fig. 5.9. For comparison, we also show as a black solid line the thermal index obtained in Ref. [102] using the self-consistent Green's function (SCGF) approach with the "2.0/2.0" interaction of Ref. [70]. Our MBPT calculations are consistent with

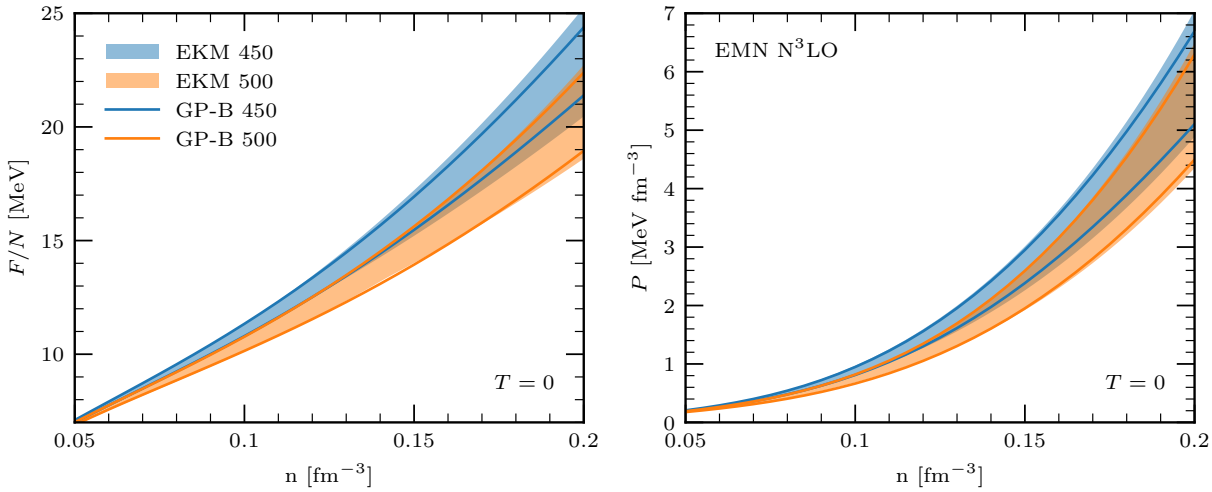

Figure 5.7: Comparison of the EFT uncertainty estimates calculated by the EKM prescription Eq. (5.7) (bands) to the Bayesian error estimates based on Gaussian processes (GP-B) of Refs. [16, 56] for the EMN N^{3}LO interaction with $\Lambda = 450\,\mathrm{MeV}$ and $\Lambda = 500\,\mathrm{MeV}$. Shown are the free energy per particle, F/N (left), and pressure P (right) as a function of density n for $T = 0$. Solid lines mark the boundaries of the 68% GP-B bands.

these nonperturbative SCGF results as the SCGF line is very similar to the NN SRG + 3N fit band, which includes the same interaction.

Compared to the thermal pressure and the thermal index, the thermal energy exhibits a much smaller interaction dependence. This can be understood in terms of the decomposition (at fixed density)

$$\begin{aligned} E_{\mathrm{th}}(T) = (F_{\mathrm{FG}}(T) - F_{\mathrm{FG}}(T=0)) \\ - (F_{\mathrm{int}}(T) - F_{\mathrm{int}}(T=0)) + T\,S(T)\,. \end{aligned} \tag{5.10}$$

Here, $F_{\mathrm{int}}(T) - F_{\mathrm{int}}(T=0)$ is small (see Fig. 5.8), and the entropy S deviates only slightly from its free Fermi gas value (see Fig. 5.4). Hence, the thermal energy E_{th} is dominated by the free gas contribution. The thermal pressure and the thermal index, however, involve the density derivative of $F_{\mathrm{int}}(T,n)$ and thus deviate more significantly from the corresponding Fermi gas values and, as a consequence, have larger uncertainties. In particular, 3N interactions have a crucial effect on their density dependence. The thermal pressure would increase with increasing density if 3N interactions were not included, as found also in Ref. [102].

The temperature dependence of the thermal index Γ_{th} is shown in Fig. 5.10 for the EMN N^{3}LO interaction. Since the index is defined as $\Gamma_{\mathrm{th}} = 1 + P_{\mathrm{th}}/\mathcal{E}_{\mathrm{th}}$, the thermal index is very sensitive to uncertainties in P_{th} and E_{th} at low temperatures (and low densities) where both these quantities are small. Therefore, in addition to the cutoff-variation band we include in Fig. 5.10 also an estimate of the numerical Monte Carlo integration errors for these quantities, where we have chosen $\Delta P_{\mathrm{th}} = 20\,\mathrm{keV\,fm^{-3}}$ and $\Delta E_{\mathrm{th}}/N = 20\,\mathrm{keV}$. As seen in Fig. 5.10, this leads to sizable uncertainties for Γ_{th} at low temperatures. For $T \gtrsim 10\,\mathrm{MeV}$ the uncertainties are better controlled and we see only a weak temperature dependence of the thermal index. This

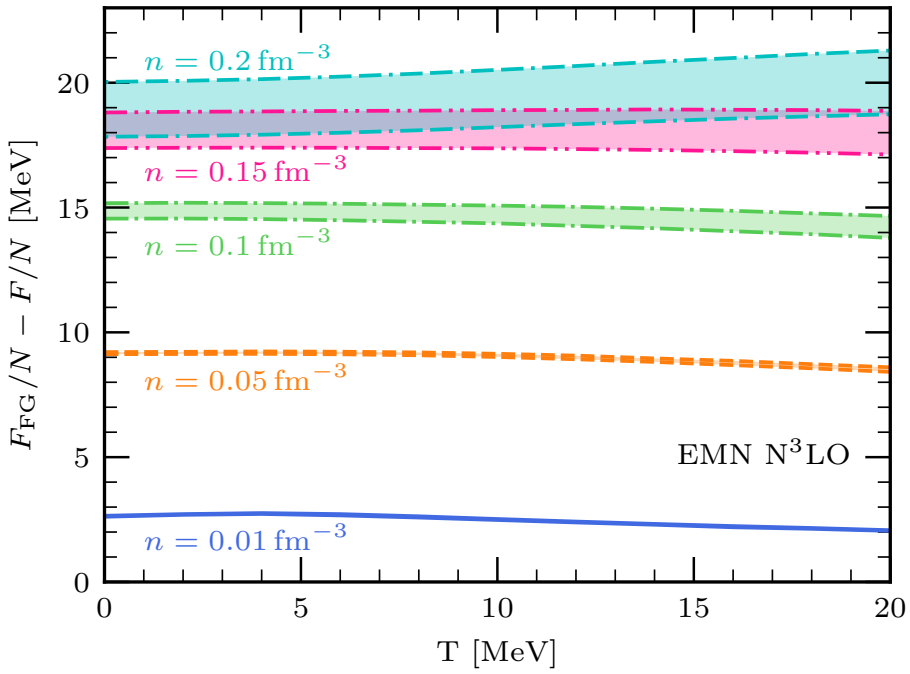

Figure 5.8: Interaction contribution to the free energy per particle, $F_{\mathrm{int}}/N = F_{\mathrm{FG}}/N - F/N$, as a function of temperature T for different densities $n = 0.01, 0.05, 0.1, 0.15$, and $0.2\,\mathrm{fm}^{-3}$, obtained from the EMN N^{3}LO NN+3N interactions (the bands are the same as in Fig. 5.2). The temperature dependence for the other interactions is similarly flat.

behavior is similar for all the other interactions considered.

5.5 Effective mass approximation

In the previous section we showed that the thermal index $\Gamma_{\mathrm{th}}(T, n)$ exhibits only a very weak temperature dependence (see Fig. 5.10). Here, we now make use of this feature to construct an approximate parametrization of thermal effects in terms of a density-dependent effective neutron mass $m_n^*(n)$. The thermal index $\Gamma_{\mathrm{th}}^*(n)$ of an ideal gas of fermions with density-dependent effective mass $m_n^*(n)$ can be expressed as (see, e.g., Ref. [104])

$$\Gamma_{\mathrm{th}}^*(n) = \frac{5}{3} - \frac{n}{m_n^*}\frac{\partial m_n^*}{\partial n}\,. \tag{5.11}$$

In Ref. [102] it was demonstrated that Γ_{th}^* determined via Eq. (5.11), with an effective mass taken from microscopic calculations, agrees well with the thermal index determined by $\Gamma_{\mathrm{th}} = 1 + P_{\mathrm{th}}/\mathcal{E}_{\mathrm{th}}$. That means, by taking for $\Gamma_{\mathrm{th}}^*(n)$ our microscopic results for $\Gamma_{\mathrm{th}}(T, n)$ at $T = 20\,\mathrm{MeV}$ shown in Fig. 5.9, we can integrate Eq. (5.11) to obtain[2] $m_n^*(n)$. For this we use $m_n^*/m_n(n = 0) = 1$, $\Gamma_{\mathrm{th}}(n = 0) = 5/3$, and interpolate linearly to our lowest-density result for Γ_{th} at $n = 0.01\,\mathrm{fm}^{-3}$.

[2]Note that uncertainties of Γ_{th} are enhanced at low densities (see Fig. 5.10 and discussion) so that m^* obtained by integrating Eq. (5.11) is an approximation.

The results for the neutron effective mass $m_n^*(n)$ determined by this procedure are shown in Fig. 5.11. The bands display cutoff or SRG scale variations (see caption of Fig. 5.2). We observe that $m_n^*(n)$ first decreases with increasing density, while at around $n \gtrsim 0.1\,\mathrm{fm}^{-3}$ the effective mass starts to increase again. This effect is related to the contribution of 3N interactions. Based only on NN interactions, the resulting effective mass would decrease with density. A similar qualitative behavior is also found in the SCGF calculations of Ref. [102].

From our results for the effective mass $m_n^*(n)$ we can construct an approximate parametrization of the temperature dependence of the EOS. For this, we again separate thermodynamic quantities into cold and thermal parts, e.g., for the pressure

$$P(T,n) = P(T=0,n) + P_{\mathrm{th}}(T,n)\,. \tag{5.12}$$

The thermal part $P_{\mathrm{th}}(T)$ is now approximated by

$$P_{\mathrm{th}}(T,n) \approx P^{m^*}_{\mathrm{FG,th}}(T,n)\,, \tag{5.13}$$

where $P^{m^*}_{\mathrm{FG,th}}$ is the thermal pressure of an ideal gas of neutrons with density-dependent mass $m_n^*(n)$, i.e.,

$$P^{m^*}_{\mathrm{FG,th}}(T,n) = n^2 \frac{\partial}{\partial n} \frac{F_{\mathrm{FG,th}}(T,n,m_n^*(n))}{N}\,, \tag{5.14}$$

where $F_{\mathrm{FG,th}}(T,n,m_n^*(n))$ is the expression for the thermal free energy of the free neutron gas with m substituted by $m_n^*(n)$.

With the microscopic calculations at zero and finite temperature at hand, we now investigate the quality of such an approximation. That is, we compare the results for the pressure $P(T,n)$ obtained using three different ways to calculate its thermal part P_{th}:

1. the full finite-temperature calculation for $P_{\mathrm{th}}(T,n)$,
2. the ideal gas approximation with bare neutron mass $P_{\mathrm{th}}(T,n) \approx P^{m}_{\mathrm{FG,th}}(T,n)$, and
3. the ideal gas approximation with density-dependent effective mass $P_{\mathrm{th}}(T,n) \approx P^{m^*}_{\mathrm{FG,th}}(T,n)$.

The results are shown in Fig. 5.12. The effective-mass approximation $P^{m^*}_{\mathrm{FG,th}}$ reproduces excellently the full finite-temperature calculation P_{th}, whereas results based on the bare mass $P^{m}_{\mathrm{FG,th}}$ deviate from the full finite-temperature calculation, with an increasing error as the density increases. This demonstrates that $\Gamma_{\mathrm{th}}(T,n) \approx \Gamma^*_{\mathrm{th}}(n)$ and $m_n^*(n)$ capture the finite-temperature effects of the neutron matter EOS very well.

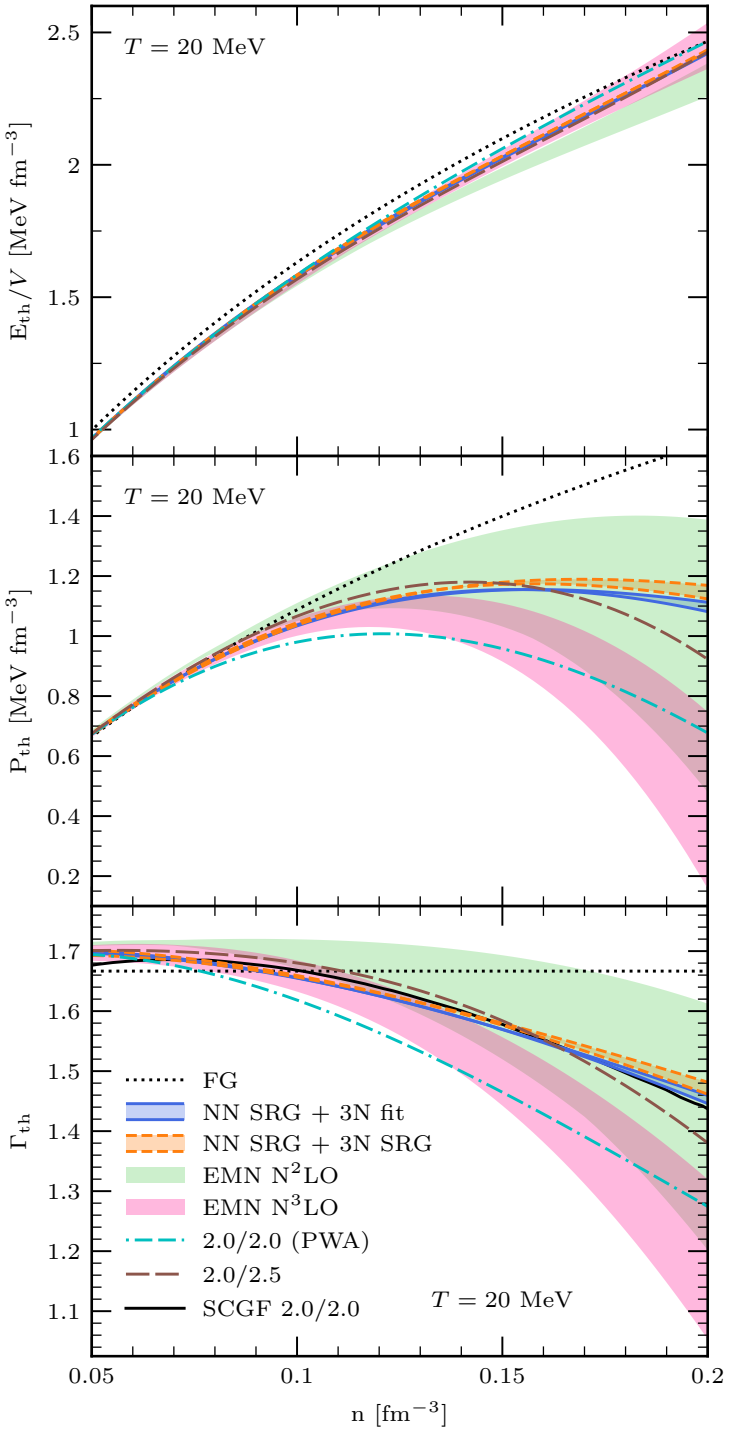

Figure 5.9: Thermal energy E_{th} (top), thermal pressure P_{th} (middle), and thermal index Γ_{th} (bottom) at $T = 20\,\mathrm{MeV}$ as a function of density n. Bands with borders are the same as in Fig. 5.2, while bands without borders display EFT uncertainty estimates from the EKM prescription Eq. (5.7). The free Fermi gas (FG) is shown as a dotted line. For comparison the thermal index of the "2.0/2.0" interaction obtained from self-consistent Green's function (SCGF) calculations from Ref. [102] is also shown (black solid line). The "2.0/2.0" interaction is contained in the NN SRG + 3N fit band. A similar analysis for E_{th}, P_{th}, and Γ_{th} has also been performed in Ref. [102].

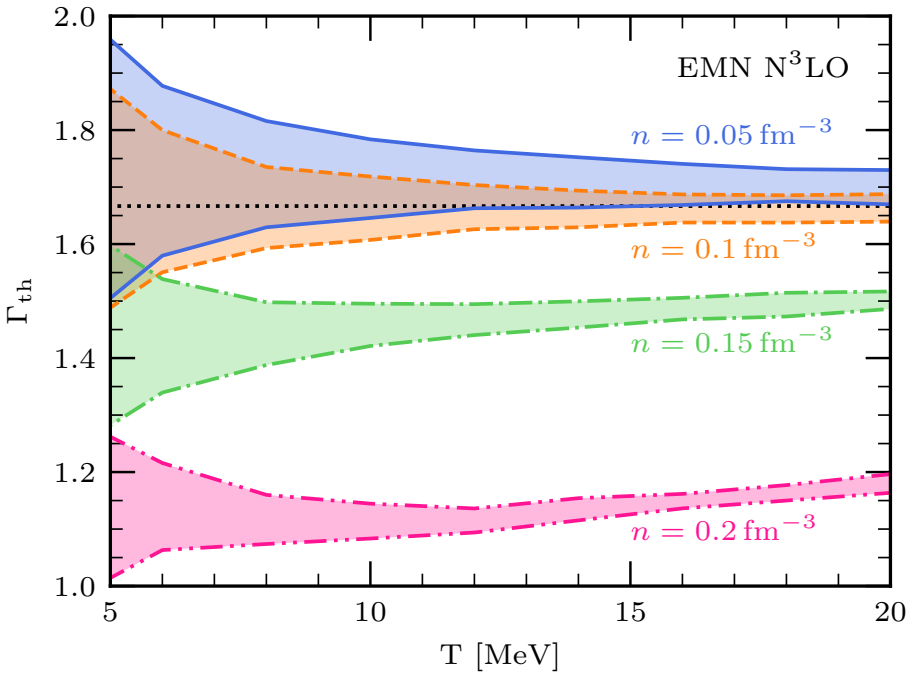

Figure 5.10: Temperature dependence of the thermal index Γ_{th} of the EMN N^{3}LO interaction for $n = 0.05, 0.1, 0.15$, and $0.2\,\mathrm{fm}^{-3}$. The bands combine cutoff variation from $\Lambda = 450\,\mathrm{MeV}$ to $\Lambda = 500\,\mathrm{MeV}$ with a constant error estimate for the Monte Carlo integration (see text for details). The dotted line marks $\Gamma_{\mathrm{FG,th}} = 5/3$.

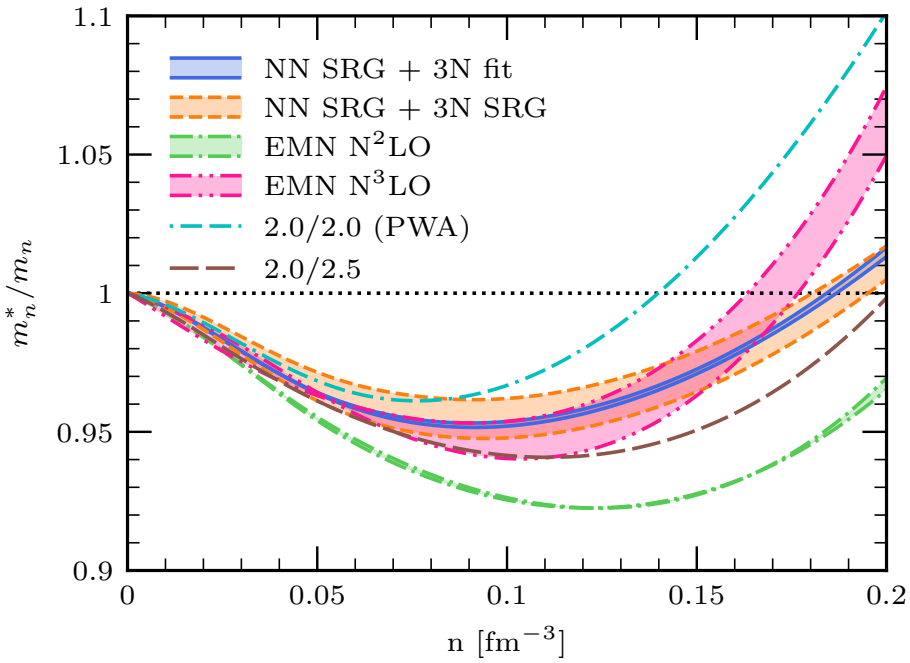

Figure 5.11: Results for the neutron effective mass $m_n^*(n)$ as a function of density n derived from the thermal index $\Gamma_{\mathrm{th}}(T, n)$ at $T = 20\,\mathrm{MeV}$ as discussed in the text. Results are shown for different NN+3N interactions (same as in Fig. 5.2).

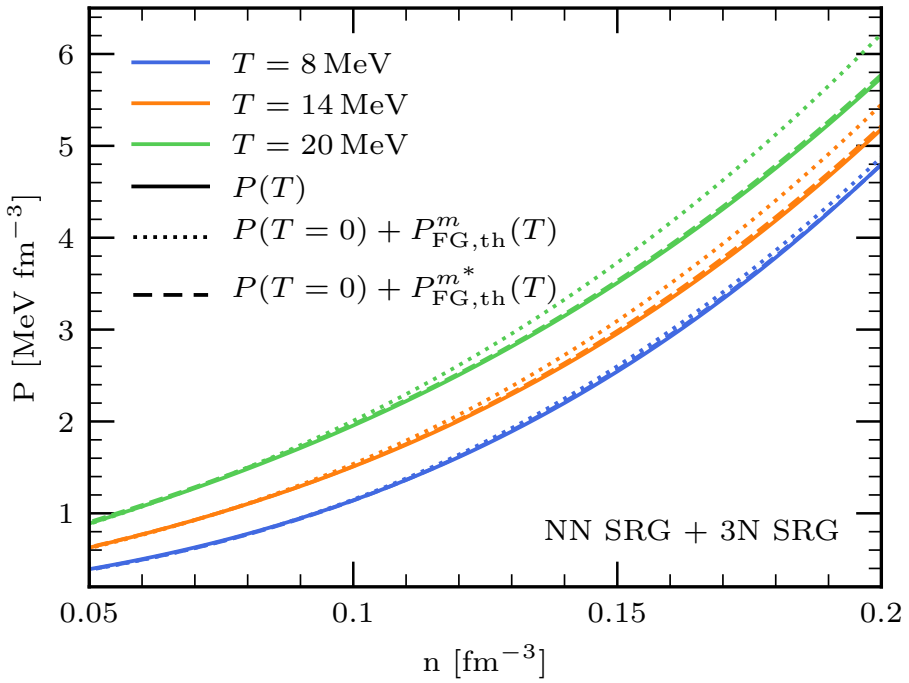

Figure 5.12: Comparison of the full temperature-dependent pressure (solid lines) to ideal Fermi gas approximations of the thermal contribution with bare neutron mass $P^{m}_{\mathrm{FG,th}}(T)$ (dotted lines) and with effective neutron mass $P^{m^*}_{\mathrm{FG,th}}(T)$ from Fig. 5.11 (dashed lines). The employed effective mass $m^*_n(n)$ is extracted at $T = 20\,\mathrm{MeV}$. See text for more details. Shown are temperatures $T = 8, 14$, and $20\,\mathrm{MeV}$ (different colors) for the consistently SRG-evolved NN+3N interaction with $\lambda_{\mathrm{SRG}} = 1.8\,\mathrm{fm}^{-1}$. The dashed lines overlap excellently with the respective solid lines for $T = 8\,\mathrm{MeV}$ and $T = 14\,\mathrm{MeV}$.

6 Asymmetric matter at finite temperature

In this Chapter, we calculate the EOS for arbitrary proton fractions and temperatures based on chiral EFT interactions to high order. We then construct a Gaussian process emulator of the free energy that enables nonparametric evaluations of the EOS and thermodynamic derivatives for arbitrary nuclear conditions, including beta equilibrium, to provide direct results for neutron star matter based on chiral EFT.

This Chapter has already been published in Ref. [1]. I performed all the calculations and developed the Monte-Carlo code for MBPT to arbitrary proton fractions by generalizing the code discussed in Chapter 5.

Our asymmetric nuclear matter calculations are based on many-body perturbation theory (MBPT) around a self-consistent Hartree-Fock (HF) state. The details can be found in Chapter 3, we only provide a summary here. The framework for evaluating MBPT diagrams using Monte Carlo integration is based on previous works [49, 59]. We use the Vegas Monte Carlo integration algorithm from Ref. [100] where we take the implementation from Ref. [101] to evaluate high-dimensional phase space integrals. We start from the grand-canonical potential,

$$\Omega(\mu_n, \mu_p, T) = -T \ln \mathrm{Tr} \left(e^{-(H - \mu_n n_n V - \mu_p n_p V)/T} \right), \tag{6.1}$$

where T is the temperature, V the system volume, and $\mu_{\tau=n,p}$ are the neutron and proton chemical potentials with corresponding baryon densities n_τ. The Hamiltonian $H = H_0 + V_{\mathrm{NN}} + V_{\mathrm{3N}}$ contains a kinetic term together with nucleon-nucleon (NN) and three-nucleon (3N) interactions constructed from chiral EFT up to next-to-next-to-next-to-leading order ($\mathrm{N^3LO}$). The MBPT series at finite T is organized following Refs. [57, 58] with the same choice of reference system as in Ref. [59]. We include all contributions from NN and 3N interactions up to second order, and at third order all interaction vertices that are NN or 3N with one line closing on itself (corresponding to the normal-ordered two-body approximation). This has been shown to be a very good approximation at $T = 0$ [49] and for neutron matter at finite T [59]. For our main results, we employ the NN interactions of Entem, Machleidt, and Nosyk (EMN) with cutoff $\Lambda = 450\,\mathrm{MeV}$ [52] and 3N interactions fit to nuclear saturation at $\mathrm{N^2LO}$ ($c_D = 2.25, c_E = 0.07$) and $\mathrm{N^3LO}$ ($c_D = 0, c_E = -1.32$) [49]. We include NN partial waves up to total angular momenta $J_{12} \leqslant 12$, and 3N channels up to $J_{\mathrm{tot}} \leqslant 9/2$ and $J_{12} \leqslant 6$ [44]. These truncations lead to uncertainties that are small compared to the EFT uncertainties for the considered densities. The interactions where provided by Ref. [51] in partial-wave decomposed form (see Chapter 2).

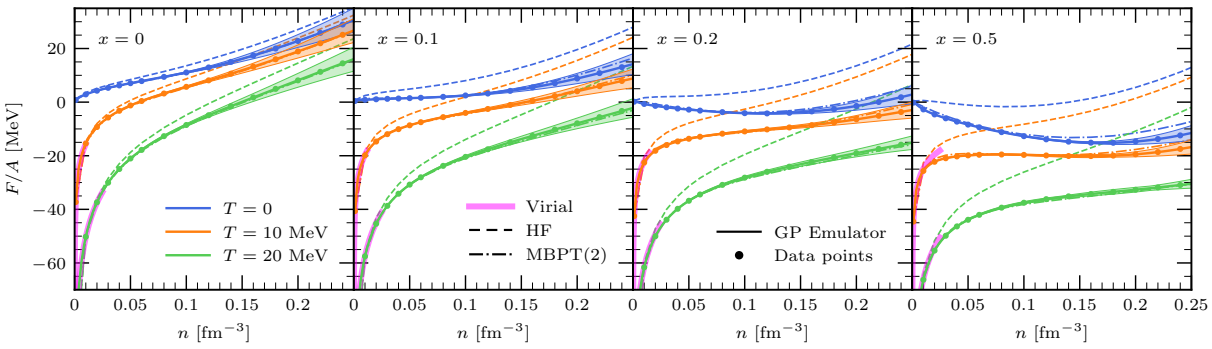

Figure 6.1: Free energy per particle F/A at N^{3}LO ($\Lambda = 450\,\mathrm{MeV}$) for different proton fractions $x = 0, 0.1, 0.2$, and 0.5 (panels from left to right) and for temperatures $T = 0, 10$, and $20\,\mathrm{MeV}$ (blue, orange, and green) as a function of density n. Our MBPT results are given by the dots, while the constructed GP emulator is shown with solid lines. The bands display theoretical EFT uncertainty estimates according to Eq. (6.3). To show the MBPT convergence, results at the HF level (dashed) and at second order (dot-dashed) are given as well. At low densities $n \leqslant 0.025\,\mathrm{fm}^{-3}$, we also compare to the virial EOS [106, 107] (for $T = 20\,\mathrm{MeV}$ this corresponds to a neutron fugacity $z_n \leqslant 0.45, 0.39, 0.34, 0.18$ for $x = 0, 0.1, 0.2, 0.5$).

The free energy density F/V is determined by

$$\frac{F}{V}(n, x, T) = \frac{\Omega}{V}(\mu_n, \mu_p, T) + \mu_n n_n(\mu_n, \mu_p, T) + \mu_p n_p(\mu_n, \mu_p, T)\,, \tag{6.2}$$

where the neutron and proton densities are given by $n_\tau = -\partial_{\mu_\tau}\Omega/V$, the total density by $n = n_n + n_p$, and $x = n_p/n$ is the proton fraction. To obtain the free energy, Eq. (6.2), as a function of density, we invert the relation between densities and chemical potentials by generalizing the method from Ref. [63] to multiple chemical potentials. In doing so, we formally expand the chemical potentials around a reference system with the same density and proton fraction as the interacting system. This re-expansion is necessary to obtain a perturbation series that is consistent with the zero-temperature formalism, and effectively deals with the anomalous diagrams at finite T [59, 60, 63].

As the evaluation of MBPT diagrams involves the computation of high-dimensional phase-space integrals, the computation of the thermodynamic potential for a large number of densities, temperatures and proton fractions is a complex task. Hence, for the evaluation of the free energy per particle and its derivatives, we construct an emulator for $F(n, x, T)/A$ using three dimensional Gaussian process (GP) regression [68], see Chapter 4 for a introduction. Gaussian processes allow us to interpolate the EOS in a way that does not spoil thermodynamic consistency (e.g., second-order derivatives commute) and to handle residual noise from the Monte Carlo integration. We use the Python library of Ref. [108] and employ the squared exponential kernel [68] with an overall scale and three length scales as hyperparameters that are determined by maximizing the likelihood. In constructing the GP, we assume that each diagram has $\Delta E_d = 5\,\mathrm{keV}$ noise from the Monte Carlo integration and the total noise of every EOS point is calculated as $\sqrt{\sum_d \Delta E_d^2}$

T	n	MBPT	$x = 0.3$		$x = 0.5$	
			N^{2}LO	N^{3}LO	N^{2}LO	N^{3}LO
0	0.1	HF	−0.6	0.8	−3.1	−1.6
0	0.1	2	−8.7	−8.4	−12.4	−12.1
0	0.1	3	−8.9(5)	−8.8(2)	−12.9(4)	−12.7(1)
0	0.16	HF	3.1	4.6	−0.1	1.4
0	0.16	2	−8.5	−8.3	−13.4	−13.1
0	0.16	3	−10.1(11)	−9.9(5)	−15.5(9)	−15.1(4)
0	0.2	HF	7.9	9.1	4.5	5.5
0	0.2	2	−6.1	−6.1	−11.6	−11.5
0	0.2	3	−8.6(27)	−8.7(13)	−14.6(24)	−14.7(10)
20	0.1	HF	−23.4	−23.3	−26.3	−26.1
20	0.1	2	−33.6	−34.1	−37.7	−38.1
20	0.1	3	−33.3(9)	−33.4(5)	−37.6(8)	−37.5(4)
20	0.16	HF	−13.5	−13.7	−16.7	−17.1
20	0.16	2	−28.9	−29.9	−34.1	−35.1
20	0.16	3	−29.8(11)	−29.0(6)	−35.5(7)	−34.3(7)
20	0.2	HF	−6.4	−7.2	−9.7	−10.8
20	0.2	2	−25.7	−27.3	−31.5	−33.1
20	0.2	3	−27.7(17)	−26.7(9)	−34.2(11)	−32.7(9)

Table 6.1: MBPT convergence of the free energy per particle F/A in MeV at N^{2}LO and N^{3}LO for different proton fractions x, temperatures T in MeV, and densities n in fm^{-3}. The EFT uncertainties determined by Eq. (6.3) are given in parentheses for the third-order MBPT results.

where the sum is over all diagrams. The resulting total noise is much smaller than interaction uncertainties due to the chiral EFT expansion and is not visible in the plots. We treat the Fermi gas (FG) contribution analytically and emulate the interaction energy per particle $F_{\rm int}/A = F/A - F_{\rm FG}/A$. The GP emulator can be performed in any set of variables. However, replacing n by the Fermi momentum $k_{\rm F} = (3\pi^2 n/2)^{1/3}$ was found to simplify the evaluation of derivatives. Moreover, all input variables are normalized to $[0, 1]$ to prevent numerical artifacts in the GP.

6.1 Free energy and GP emulation

In Fig. 6.1 we present results for F/A as a function of density for different proton fractions and temperatures. We evaluate the MBPT diagrams on the non-uniform grid with values $n = 0.001, 0.01, 0.02, \ldots, 0.05, 0.06, 0.08, \ldots, 0.32\,\text{fm}^{-3}$, $x = 0, 0.1, \ldots, 0.7$, and $T = 0, 5, 10, 15, 20, 30\,\text{MeV}$, such that in regions where the free energy changes more rapidly, more EOS points are calculated. The EOS points are marked with dots in Fig. 6.1, while the results obtained from the GP emulator are shown as solid lines. An excellent agreement is evident.

To further assess the quality of the emulator we employ the following strategy: for every data point calculated, we construct a GP emulator without including that data point. The difference of the GP prediction to the actual data point serves as a measure of the prediction quality. The maximal (mean) error obtained by this procedure is 0.0656 MeV (0.0096 MeV) when restricted

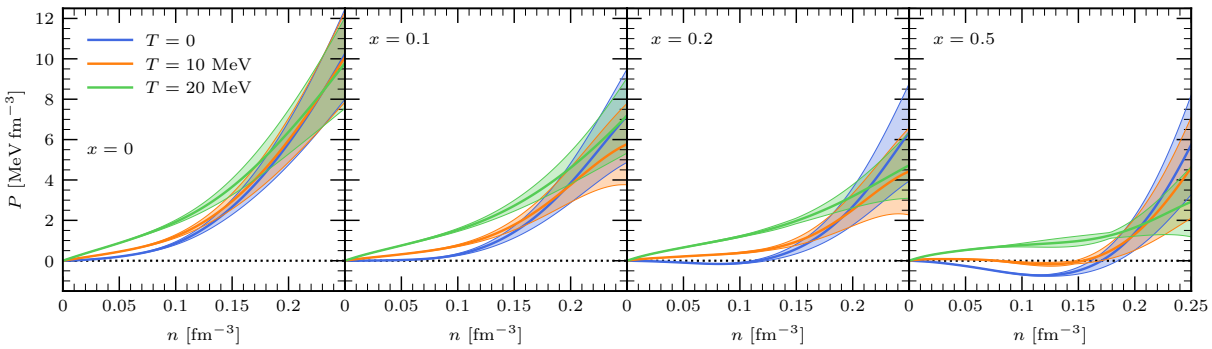

Figure 6.2: Same as Fig. 6.1 but for the pressure P at N^{3}LO ($\Lambda = 450\,\mathrm{MeV}$) from the GP emulator and with EFT uncertainties.

to the data points shown in the plots ($n \leqslant 0.25\,\mathrm{fm}^{-3}$, $x \leqslant 0.5$, and $T \leqslant 20\,\mathrm{MeV}$). If necessary, the quality of the emulator could even be improved by using an optimized kernel.

At low densities and finite T, we compare our results to the model-independent virial EOS [106, 107] in Fig. 6.1. Since we consider homogeneous matter, we do not include the contributions from alpha particles in the virial EOS (i.e., we compare against Ref. [107] for $n_\alpha = 0$) For $n \leqslant 0.025\,\mathrm{fm}^{-3}$ and low fugacities, we find excellent agreement with our results. For higher densities, the inclusion of higher virial coefficients and effects due to the effective nucleon mass play an important role.

For estimates of the theoretical uncertainties for an observable X due to the truncated chiral expansion we use the prescription of Ref. [54],

$$\Delta X^{(j)} = Q \cdot \max\left(|X^{(j)} - X^{(j-1)}|, \Delta X^{(j-1)}\right) , \tag{6.3}$$

where $X^{(j)}$ is the observable calculated at N^{j}LO and the expansion parameter is $Q = p/\Lambda_b$, where we take $\Lambda_b = 500\,\mathrm{MeV}$ for the EFT breakdown scale and p is a typical momentum for the observable of interest. Following Ref. [49], we take p to be the root-mean-square momentum of the Fermi gas $p^2 = \langle k^2 \rangle = 3T(\sum_\tau m_\tau^{5/2} F_{3/2}(\mu_\tau/T))/(\sum_\tau m_\tau^{3/2} F_{1/2}(\mu_\tau/T))$, where the chemical potentials μ_τ are determined from the density $n_\tau = 2^{-1/2}\,(m_\tau T/\pi)^{3/2}\,F_{1/2}(\mu_\tau/T)$ and $F_n(x) = \Gamma(n+1)^{-1} \int_0^\infty \mathrm{d}t\, t^n (1+\exp(t-x))^{-1}$ are Fermi integrals (see Chapter 1). The resulting EFT uncertainty bands at N^{3}LO are shown for the third-order MBPT results in Fig. 6.1. In addition, we show the first-order (HF) and second-order MBPT(2) results to assess the MBPT convergence of the expansion. Table 6.1 gives numerical values at particular values of n, x, T to document the MBPT and chiral convergence.

6.2 Pressure and thermal effects

The pressure $P = n^2 \partial_n (F/A)|_{x,T} = P_{\mathrm{FG}} + n^2 \partial_n (F_{\mathrm{int}}/A)|_{x,T}$ is shown in Fig. 6.2 for different proton fractions and temperatures, where the derivative of the interaction energy F_{int}/A is calculated using the GP emulator. As expected, the pressure decreases with increasing proton fraction, and for very neutron-rich conditions depends only weakly on the temperature for $n \gtrsim n_0$. Inter-

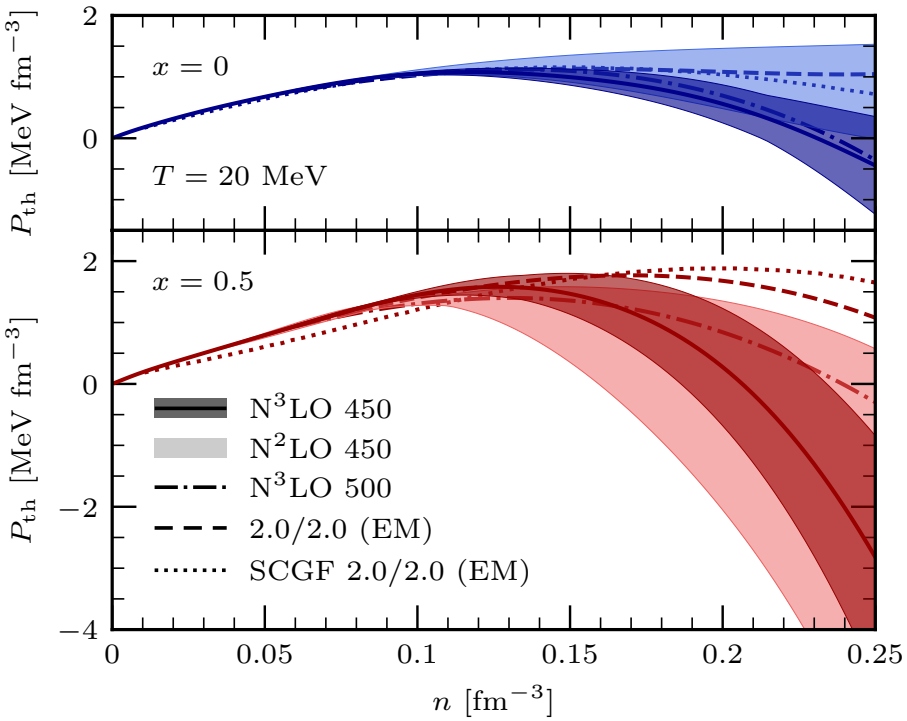

Figure 6.3: Thermal pressure $P_{\rm th}$ for neutron matter (blue) and symmetric matter (red) for $T = 20\,\text{MeV}$ as a function of density. In addition to the N^{3}LO results with $\Lambda = 450\,\text{MeV}$ (solid lines) we also show $\Lambda = 500\,\text{MeV}$ (dot-dashed lines) as well as for the 2.0/2.0 (EM) interaction [70] (dashed lines). For the latter, we compare against the SCGF results from Ref. [102] (dotted lines). The darker EFT uncertainty bands are N^{3}LO, while the lighter ones are for N^{2}LO.

estingly, for symmetric matter we find that the pressure decreases with increasing temperature for $n \gtrsim 0.2\,\text{fm}^{-3}$. This negative thermal expansion has also been observed in Ref. [17] for low-momentum interactions. For neutron-rich matter, this behavior is seen in Fig. 6.2 starting at higher densities.

To investigate this further, we show the thermal pressure $P_{\rm th} = P(T) - P(T=0)$ in Fig. 6.3 for neutron matter and symmetric matter for $T = 20\,\text{MeV}$. We find that the thermal pressure starts to decrease at $n \approx 0.15\,\text{fm}^{-3}$ and becomes negative around $n \approx 0.2\,\text{fm}^{-3}$. For neutron matter this finding is consistent with Ref. [59] and can be understood in terms of a neutron effective mass m_n^* that increases at higher density due to repulsive 3N contributions [59, 102] [$P_{\rm th} \leqslant 0$ requires $\partial m_n^*/\partial n_n \geqslant 0$, see Eqs. (39) and (41) in Ref. [59]]. Figure 6.3 shows that a decreasing thermal pressure at higher densities is found at different orders (N^{2}LO and N^{3}LO), different cutoffs ($\Lambda = 450\,\text{MeV}$ and $500\,\text{MeV}$), as well as for the 2.0/2.0 (EM) interaction [70], while the size of the decrease has large theoretical uncertainties. For the 2.0/2.0 (EM) interaction, we can also compare our MBPT against self-consistent Green's function (SCGF) results [102] and find good agreement (with the small differences likely due to the $T = 0$ extrapolation and the normal-ordering approximation in Ref. [102]). Note that the cutoff dependence of the negative thermal expansion might indicate that the maximal density accessible is limited based on the

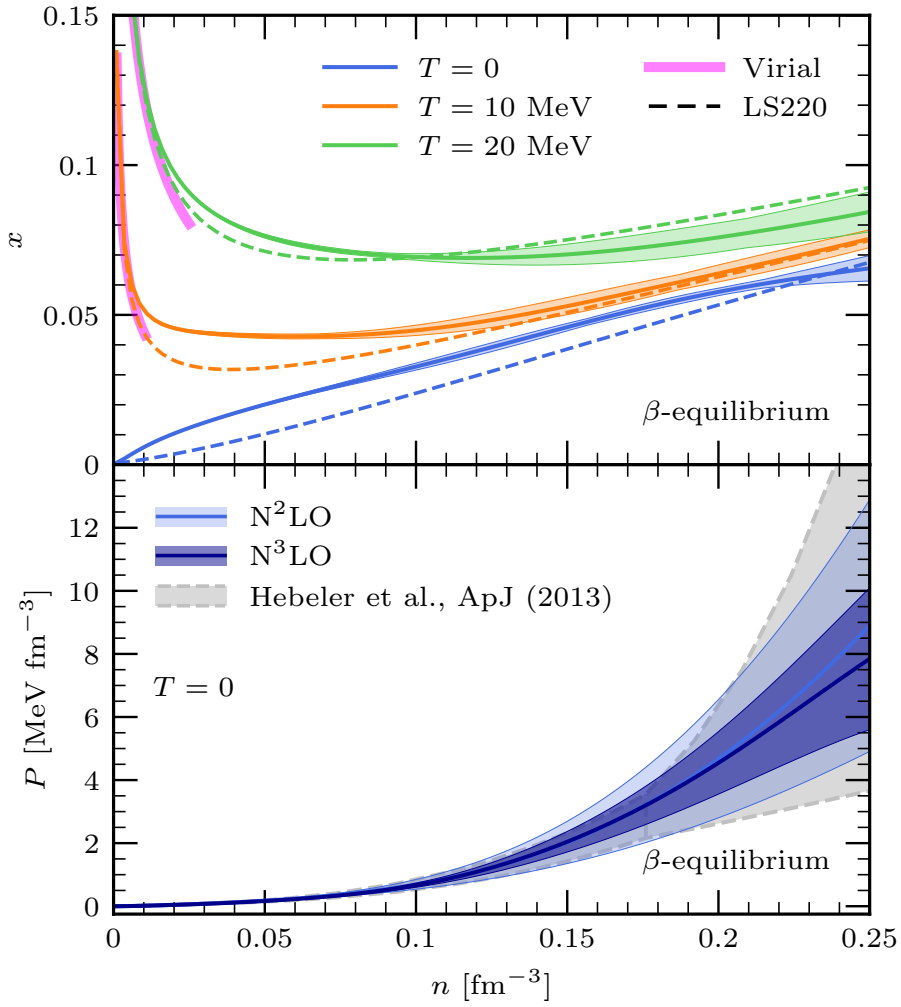

Figure 6.4: Upper panel: Proton fraction x in beta equilibrium at N^{3}LO for different T as a function of density. For comparison, we show the virial EOS and the LS220 EOS [109]. Lower panel: Pressure P in beta equilibrium for $T = 0$ at N^{2}LO and N^{3}LO. We compare against the EOS band from Hebeler *et al.* [22] based on chiral EFT interactions up to $1.1n_0$ and a general piecewise polytrope extension to higher densities.

employed interactions.

6.3 Matter in beta equilibrium

Using the GP, we can access arbitrary proton fractions and derive other quantities through thermodynamically consistent derivatives. We first use the GP to calculate the proton fraction x of neutron star matter in beta equilibrium as a function of density for different temperatures. For a given density and temperature, x is determined by the condition $m_n + \mu_n = m_p + \mu_p + m_e + \mu_e$ (see, e.g., Ref. [22]), where the neutron and proton chemical potentials are given by $\mu_\tau = F/A + n\partial_n(F/A) + (\delta_{\tau,p} - x)\,\partial_x(F/A)$. The electron chemical potential is determined from the density of an ultra-relativistic Fermi gas, $n_e = 2/\pi^2 T^3 F_2(\mu_e/T)$ with the Fermi integral F_2 (see Eq. (3.7) with $\epsilon(p) = p$) through charge neutrality $n_p = n_e$. Our results using the GP

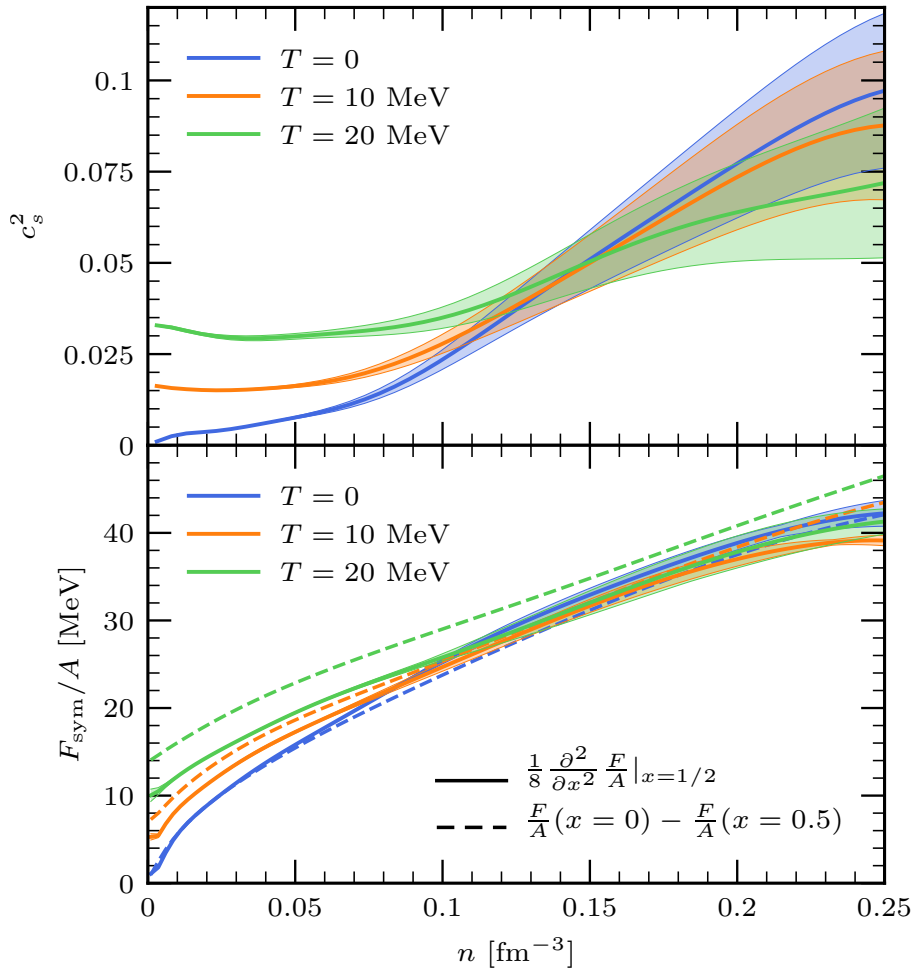

Figure 6.5: Speed of sound squared c_s^2 for neutron matter (upper panel) and symmetry free energy per particle $F_{\rm sym}/A$ (lower panel) at N^{3}LO for different T as a function of density. We show results based on different definitions for $F_{\rm sym}/A$ (second derivative around symmetric matter and difference between neutron and symmetric matter).

emulator are shown in the upper panel of Fig. 6.4. We find very narrow EFT uncertainty bands in this case, using again Eq. (6.3) with $Q = Q(n, x = x_{\beta\text{-eq.}}^{\rm N^3LO}(n,T), T)$. At small densities and finite T, the proton fraction is dominated by the kinetic part and follows the virial EOS. At higher densities, the density dependence of x is weaker, with proton fractions of $4 - 8\,\%$ for the temperatures considered. Overall, we find a reasonable agreement with the Lattimer and Swesty EOS LS220 [109] but our chiral EFT results exhibit a weaker density dependence.

The GP thus also enables a first nonparametric calculation of the neutron star EOS. In the lower panel of Fig. 6.4 we show the pressure of matter in beta equilibrium $P(n, x_{\beta\text{-eq.}}, T = 0)$ at N^{2}LO and N^{3}LO with EFT uncertainty estimates. The N^{3}LO band is systematically smaller and overlaps with the N^{2}LO band over the full density range. Moreover, both bands behave naturally towards higher densities and hence show no indication for a breakdown of the chiral expansion up to $n \lesssim 0.25\,\text{fm}^{-3}$. For comparison, we also show the EOS band from Hebeler *et al.* [22] based on chiral EFT interactions up to $1.1 n_0$ and a general piecewise polytrope extension to higher

densities constrained by causality and the observation of two-solar-mass neutron stars. This EOS band results mainly from variations of the chiral 3N forces, so that the comparison is not direct. Nevertheless, the overlap with the nonparametric N^{2}LO and N^{3}LO bands is remarkable. Up to n_0, the N^{3}LO band prefers high pressures in the Hebeler *et al.* band [22] and at higher n, it provides important new constraints.

6.4 Speed of sound and symmetry energy

Next, we study the speed of sound $c_s^2 = \partial P/\partial\varepsilon|_{S,x} = \frac{n}{P+\varepsilon}\partial P/\partial n|_{S,x}$ with the internal energy density $\varepsilon = n(E/A + m_n)$ (see, e.g. Ref. [104]). The derivative at constant entropy S and constant proton fraction x is performed numerically based on $P(n, x, T(n, x, S))$. Our results using the GP emulator are shown for neutron matter in the upper panel of Fig. 6.5. Given that c_s^2 is a second derivative, the EFT uncertainties are larger in this case. At $T = 0$, c_s^2 increases monotonously while the increase is weaker at finite T. As for the pressure, c_s^2 decreases at higher densities with increasing T.

As another GP application, we show the symmetry free energy per particle $F_{\rm sym}/A$ as a function of density for different T in the the lower panel of Fig. (6.5). We compare two common definitions: the second derivative around symmetric matter and the difference between neutron matter and symmetric matter, where the difference probes the size of contributions beyond a quadratic x dependence (see Chapter 1 for the asymmetry expansion). Since the numerical uncertainties are enhanced in second derivatives due to residual noise from the Monte Carlo integration, we calculate $\partial^2(F/A)/\partial x^2|_{x=1/2}$ by fitting a GP to each MBPT diagram individually. The difference definition is more sensitive to thermal effects due to the nonquadratic contributions contained in the kinetic part. For the second-derivative definition, we find that $F_{\rm sym}/A$ is narrowly predicted at N^{3}LO at a fixed saturation density n_0, with $F_{\rm sym}(n_0)/A \approx 30\,\text{MeV}$ at $T = 0$, while the uncertainty increases if one allows this reference density to vary [56]. Moreover, the T dependence of the symmetry energy is mild at n_0, with larger increases at lower and higher n.

7 Liquid-gas phase transition in symmetric nuclear matter

This chapter investigates the temperature dependence of symmetric nuclear matter ($x = 0.5$). In this limit we will assume that neutron and protons are thermodynamic indistinguishable, neglecting isospin breaking effects. The liquid-gas phase transition is studied and the phase diagram is calculated. Finally we provide the critical temperature and critical density, which can be extracted from experiments. The calculations are based on the Gaussian process emulator discussed in Chapter 6 to evaluate the EOS for the EMN interaction with a cutoff of $\Lambda = 450\,\mathrm{MeV}$ where we include second order MBPT diagrams (MBPT(2)) only (see Chapter 6). The nuclear liquid-gas transition has previously been studied based on chiral EFT interactions in, e.g., Refs. [17, 88]. For a general introduction to the liquid-gas transition see, e.g., Refs. [7, 8].

7.1 Pressure

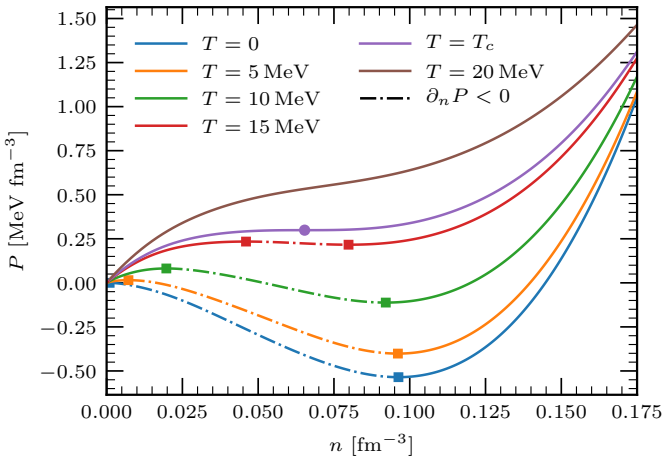

Figure 7.1: Pressure of symmetric nuclear matter as function of the number density. Different line show different temperatures $T = 0, 5, 10, 15, 20$ MeV. The dot-dashed line segments show regions where the pressure derivative is negative. The filled circle shows the critical point, see text.

Figure 7.1 shows the pressure of symmetric nuclear matter for different temperatures. For larger temperatures, e.g., $T = 20\,\mathrm{MeV}$, the pressure is a monotonically increasing function of density, while at lower temperatures there are regions where the pressure decreases with increasing density (shown by the dot-dashed lines and delimited by filled squares with $\partial_n P = 0$).

Furthermore for some temperatures and densities the pressure is negative, e.g., for $T = 0$ the pressure is negative for all densities up to nuclear saturation density.

The critical temperature T_c is the lowest temperature such that the pressure is still a monotonic function of density, with the critical density n_c defined as the saddle point of the pressure [8], e.g.,

$$\left.\frac{\partial P}{\partial n}\right|_{n_c,T_c} = \left.\frac{\partial^2 P}{\partial n^2}\right|_{n_c,T_c} = 0\,. \tag{7.1}$$

The critical point is shown as a solid circle in Fig. 7.1. The region where the pressure is not monotonically increasing with density $\partial P/\partial n < 0$ (spinodal region) has a negative isothermal compressibility $\kappa_T = n^{-1}\partial n/\partial P|_T < 0$ and is therefore unphysical (see Refs. [7, 8, 17] for details and general stability relation $\kappa_T \geq 0$). This Van-der-Waals like EOS is a result of enforcing a single phase [8]. It is a sign that there are conditions, where the system is unstable to phase separation into a mixture of gas and liquid (in analogy with the Van-der-Waals EOS) [8, 17]. Phase separation is possible in the unstable region $T < T_c$, for $T \geq T_c$ there will be a single phase.

For the first-order liquid-gas phase transition in symmetric nuclear matter, our results give the preliminary ranges for the critical temperature, density, and pressure, $T_c = 15.9 - 16.3\,\mathrm{MeV}$, $n_c = 0.07 - 0.11\,\mathrm{fm}^{-3}$, and $P_c = 0.30 - 0.40\,\mathrm{MeV\,fm}^{-3}$, where the ranges are obtained by considering the N^{3}LO interaction at MBPT(3) and MBPT(2). A full analysis will be the topic of future work.

7.2 Maxwell construction

The system is unstable to phase separation in the unphysical region, it will separate into phases with different densities [8, 17]. The physical EOS can be recovered from Fig. 7.1 by applying a Maxwell construction (equal-area rule in the P-V diagram) [7, 8, 17].

The phase transition will occur at constant T, constant P, and constant μ and the densities of the two phases can be determined by using

$$P(T, n_g) = P(T, n_l)\,, \tag{7.2}$$

$$\mu(T, n_g) = \mu(T, n_l)\,, \tag{7.3}$$

where μ is the chemical potential, n_g is the density of the gas phase, and n_l the density of the liquid phase, see e.g. Ref. [7].

This is shown in Fig. 7.2 for $T = 10\,\mathrm{MeV}$. At low densities the system is in a pure gas phase. At the first filled circle the system separates into two phases with densities n_l and n_g and the phase transition occurs at constant P and μ. After the second filled circle there is a pure liquid phase. In the liquid-gas phase it is energetically favorable to form droplets with density n_l surrounded by a gas with density n_g. Note that the region with negative isothermal compressibility is enclosed in the coexistence region and is removed after the construction.

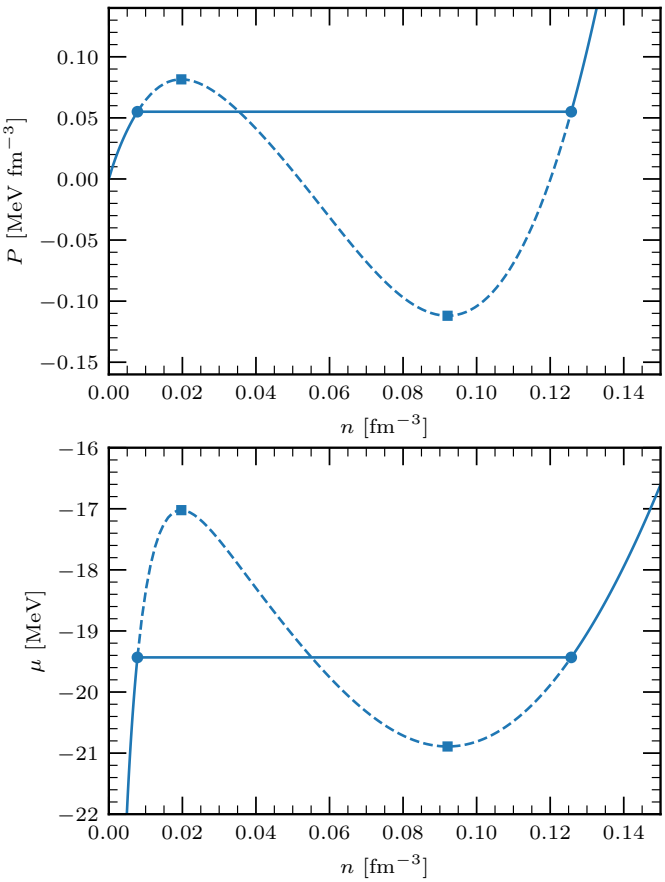

Figure 7.2: Pressure (upper panel) and chemical potential (lower panel) as function of number density for $T = 10\,\mathrm{MeV}$. The filled circles show the densities n_g and n_l with simultaneous equal pressure and chemical potentials. The region where the isothermal compressibility is negative are enclosed by filled squares.

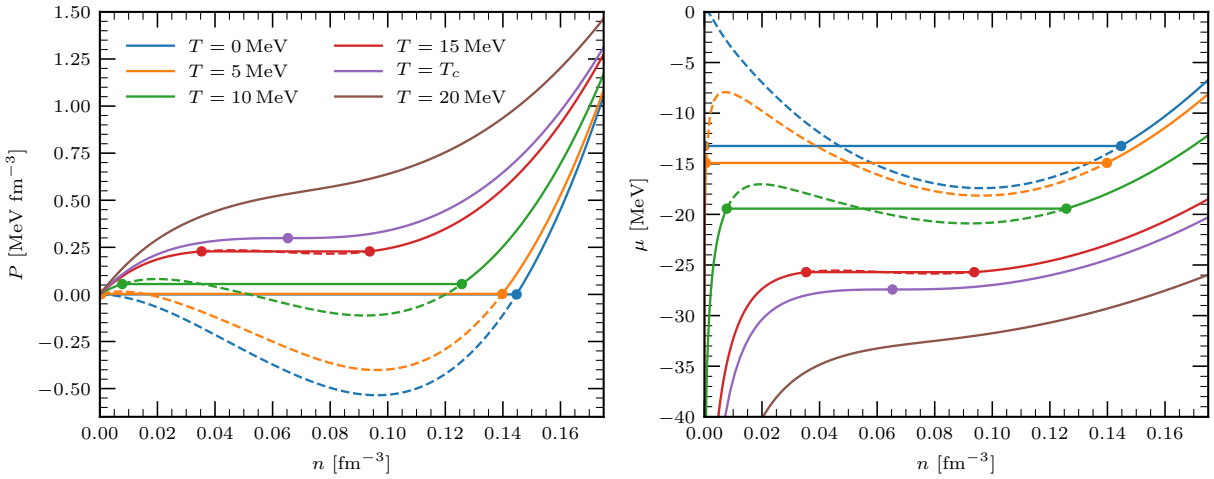

Figure 7.3: Maxwell construction for the pressure (left) and chemical potential (right) as a function of number density for different temperatures (color). The dotted lines show the quantities without the Maxwell construction.

For our calculations this construction is always possible for $0 < T < T_c$. The physical pressure and physical chemical potential are shown for different temperatures in Fig. 7.3. Note that there is no pure gas phase at $T = 0$.

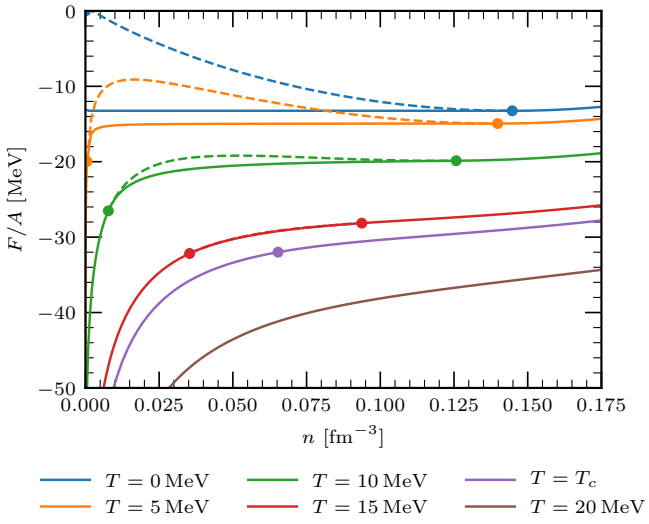

Figure 7.4: Maxwell construction for the free energy as a function of number density for different temperatures (colors). Filled circles show the densities n_g and n_l of equal pressure and chemical potential. Dotted lines show the free energy without the Maxwell construction.

Given the pressure P and the chemical potential μ of the physical system, the physical free energy F can be constructed as

$$\frac{F}{A} = \mu - P/n \tag{7.4}$$

where n is the density. Pressure and chemical potential are held constant in the liquid-gas phase $n_g \leq n \leq n_l$ phase. The physical free energy is shown in Fig. 7.4. Note that the physical free energy is lower than the energy of to the unphysical EOS (dashed lines).

7.3 Phase diagram

Fig. 7.5 shows the phase diagram of symmetric nuclear matter. The phase coexistence boundary (binodal), as determined from the Maxwell construction, is shown as solid lines. In addition we also show the spinodal line, which encloses the unphysical region with negative isothermal compressibility, e.g. $\partial P/\partial n < 0$. Note that the spinodal region (densities n and temperatures T with $\partial P(T,n)/\partial n < 0$) is contained in the binodal region. Phase coexistence is possible inside of the binodal line. A extension of this study to low proton fractions at $T = 0$ with a focus on the existence of proton drip is presented in Chapter 8.

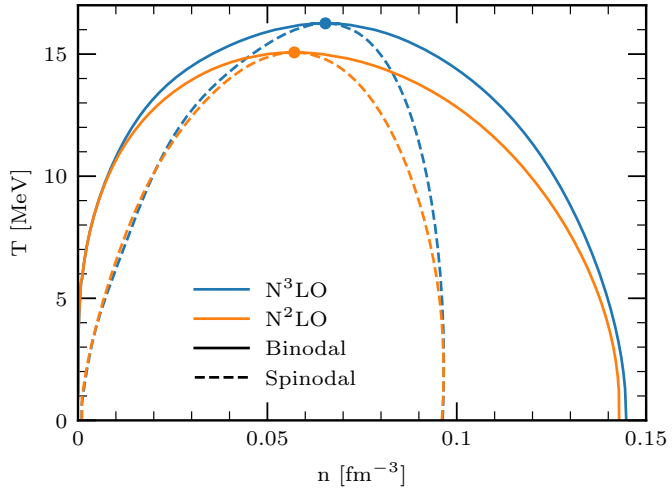

Figure 7.5: Phase diagram in density-temperature plane of symmetric nuclear matter. Binodal (solid) and spinodal (dashed) are shown for different interaction orders N^{2}LO (orange) and N^{3}LO (blue). Inside the binodal line a gas-liquid mixture coexists.

8 Dilute proton solution

This chapter investigates the possibility of phase coexistence at low proton concentrations and zero temperature as introduced in Chapter 1. For this investigation we follow Ref. [19]. Furthermore we neglect finite-size effects (Coulomb interaction, surface effects) [19]. For a general introduction to phase transitions see, e.g., Refs. [7, 8].

8.1 Chiral EFT calculations

Our investigations of dilute proton solutions in neutron-rich matter are based on our calculations of the asymmetric matter EOS presented in Chapter 6. Here, we only give a short summary of the method. Thermodynamic quantities are determined starting from a expansion of the grand-canonical potential

$$\Omega(\mu_n, \mu_p, T) = -T \ln \mathrm{Tr} \left(e^{-(H - \mu_n n_n V - \mu_p n_p V)/T} \right) \tag{8.1}$$

in many-body perturbation theory, where μ_n and μ_p are neutron and proton chemical potentials, T is the temperature and V the volume. The Hamiltonian is given by $H = T + V_{NN} + V_{3N}$ with kinetic energy T, two-nucleon potential V_{NN} and three-nucleon potential V_{3N}. Two- and three-nucleon interactions are constructed using chiral effective field theory at next-to-next-to-next-to-leading order ($\mathrm{N^3LO}$) with a cutoff of $\Lambda = 450\,\mathrm{MeV}$. Furthermore, interactions at $\mathrm{N^2LO}$ are used to test the sensitivity to the interaction.

The thermodynamic potential at fixed density of neutrons and protons, the Helmholtz free energy, is given by

$$\begin{aligned} \frac{F}{V}(n, x, T) = \frac{\Omega}{V}(\mu_n, \mu_p, T) &+ \mu_n n_n(\mu_n, \mu_p, T) \\ &+ \mu_p n_p(\mu_n, \mu_p, T) \end{aligned} \tag{8.2}$$

where n is the total density and x the proton fraction. It is constructed by re-expanding around a reference system with the same density (see Chapter 3 for the details). Pressure $P = n^2 \partial_n (F/A)$ and chemical potentials $\mu_\tau = F/A + n\partial_n(F/A) + (\delta_{\tau,p} - x)\,\partial_x(F/A)$ for $\tau = n, p$ are determined from free energy F/A by using a Gaussian process emulator (see Chapters 4 and 6 for details).

8.2 Results

In the following nuclear matter will refer to a system that has a non-zero proton concentration ($x > 0$). The coexistence of neutron matter with nuclear matter (neutron drip) and nuclear matter with nuclear matter (proton drip) can be determined by using pressure and chemical potentials [7, 8, 19]. For neutron drip the conditions read

$$P(n_n^{(1)}, 0) = P(n_n^{(2)}, n_p^{(2)}) \tag{8.3}$$
$$\mu_n(n_n^{(1)}, 0) = \mu_n(n_n^{(2)}, n_p^{(2)}) \tag{8.4}$$

while for proton drip we have

$$P(n_n^{(1)}, n_p^{(1)}) = P(n_n^{(2)}, n_p^{(2)}) \tag{8.5}$$
$$\mu_n(n_n^{(1)}, n_p^{(1)}) = \mu_n(n_n^{(2)}, n_p^{(2)}) \tag{8.6}$$
$$\mu_p(n_n^{(1)}, n_p^{(1)}) = \mu_p(n_n^{(2)}, n_p^{(2)}) \tag{8.7}$$

where $n_\tau^{(1)}$ are the densities in the system with fewer protons.

8.2.1 Binodal

The solutions to Eqs (8.3) - (8.7) are shown in Fig. 8.1. The densities for neutron drip $n_n^{(1)}$, $n_n^{(2)}$, and $n_p^{(2)}$ are shown as blue lines while the densities for proton drip (with additional $n_p^{(1)} > 0$) are shown in red when coexistence is possible. The lower panel shows the proton chemical potential for the coexistence of neutron matter $\mu_p(\mu_n, 0)$ with nuclear matter $\mu_p(\mu_n, n_p^{(2)})$ (neutron drip). For $\mu_n \gtrsim 14.47\,\mathrm{MeV}$ the proton chemical potential in neutron matter smaller than in nuclear matter

$$\mu_p(\mu_n, n_p = 0) < \mu_p(\mu_n, n_p^{(2)})\,, \tag{8.8}$$

e.g. it is energetically favorable for protons to move from nuclear matter to neutron matter (proton drip). In this region it is inconsistent to have coexistence of neutron matter with nuclear matter. Proton drip is possible starting at $\mu_n \approx 14.47\,\mathrm{MeV}$ where the proton chemical potentials are equal [in this case the solution for neutron drip is also a solution for proton drip Eqs. (8.5) - (8.7)], while we also find coexistence for higher densities.

8.2.2 Phase diagram

The coexistence occurs along lines in the (n_n, n_p) plane, e.g.

$$n_n = n_n^{(1)}(1-\alpha) + n_n^{(2)}\alpha \tag{8.9}$$
$$n_p = n_p^{(1)}(1-\alpha) + n_p^{(2)}\alpha \tag{8.10}$$

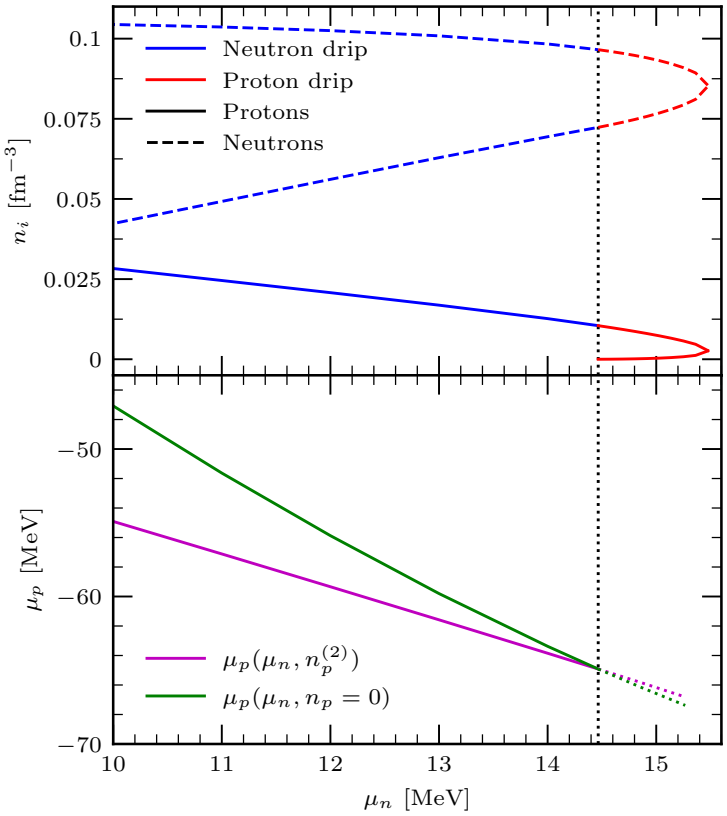

Figure 8.1: Upper panel: Coexistence of neutron matter with asymmetric matter (blue lines left of the vertical dotted line) and coexistence of asymmetric matter with asymmetric matter (red lines right side) as a function of the neutron chemical potential. Proton number densities are shown as solid lines and neutron densities are shown with dashed lines. Lower panel: Proton chemical potential as a function of the neutron chemical potential in neutron matter and asymmetric matter for coexistence of neutron matter with asymmetric matter. The vertical dotted line shows the neutron chemical potential where both proton chemical potentials have equal values.

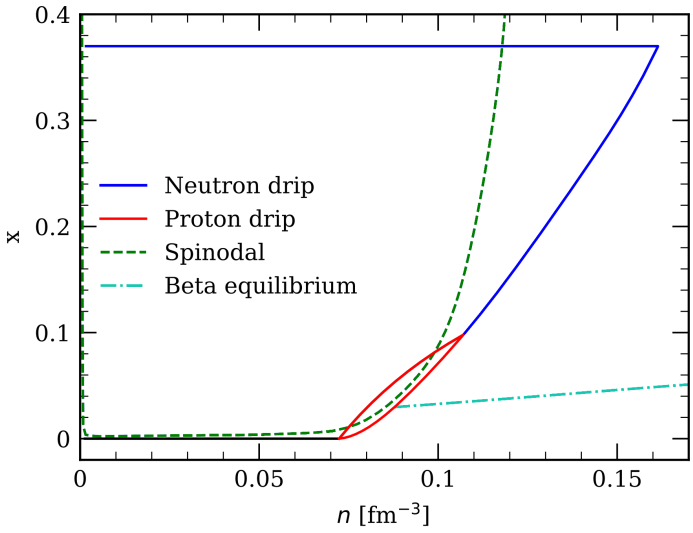

Figure 8.2: Phase diagram as a function of the total number density and the proton fraction for the N^{3}LO interaction. In addition to the regions where neutron drip (blue) and proton drip (red) is possible, also the spinodal line Eq. (8.11) (green) and the composition of homogeneous matter in beta equilibrium are shown.

where $\alpha \in [0,1]$ is the volume fraction (and $n_p^{(1)} = 0$ for neutron drip). The corresponding phase diagram in the (x,n) plane is shown in Fig. 8.2. We find that neutron drip (blue region) is possible for a large region in proton fraction and density. The vertical end of the neutron drip region at $x \approx 0.37$ is reached for $\mu_n = 0$ with vanishing pressure $P = 0$ (self-bound system). Furthermore we also find a small region with low proton concentration where proton drip is possible (red).

We determine the composition in β-equilibrium for matter in the homogeneous phase by solving $m_n + \mu_n\left(x(n),n\right) = m_p\left(x(n),n\right) + \mu_p + m_e + \mu_e\left(x(n),n\right)$ (see, e.g., Ref. [22]) where the electrons are treated ultra relativistic, e.g. $\mu_e = (3\pi^2 n_e)^{1/3}$ [22], and we assume charge neutrality $n_e = n_p$. For high densities $n \gtrsim 0.09\,\mathrm{fm}^{-3}$ matter in β-equilibrium is in its homogeneous phase, while it reaches proton and neutron drip for lower densities.

In addition we also show the spinodal line (instability to density fluctuation) determined by [22]

$$v_0 = \frac{\partial \mu_p}{\partial n_p} - \frac{(\partial \mu_p/\partial n_n)^2}{(\partial \mu_n/\partial n_n)} = 0 \tag{8.11}$$

in Fig. 8.2. Note that the instability region is contained in the neutron and proton drip region.

8.2.3 Robustness

Finally we want to investigate, how robust our findings for proton drip are. First, the results in Fig. 8.2 are for the nuclear interaction at order N^{3}LO. For the interaction at N^{2}LO we also find proton drip, and the proton fraction and density region where it is possible is shown in Fig. 8.3.

The proton drip regions for N^{2}LO and N^{3}LO are similar.

Furthermore, conditions when proton drip can occur are very neutron rich. It would be desirable to vary properties of neutron matter and check how robust the finding for proton drip are and what the impact of neutron matter is. We use the phenomenological parametrization of the energy per particle $\epsilon(x,n)$ as a function of proton fraction x and total density n from Ref. [22]

$$\begin{aligned}\epsilon(x,n) = \epsilon_{\text{kin}}(x,n) \\ - T_0\left[(2\alpha - 4\alpha_L)x(1-x) + \alpha_L\right]\left(\frac{n}{n_0}\right) \\ - T_0\left[(2\eta - 4\eta_L)x(1-x) + \eta_L\right]\left(\frac{n}{n_0}\right)^{4/3},\end{aligned} \tag{8.12}$$

where $n_0 = 0.16\,\text{fm}^{-3}$, $T_0 = (3\pi^2 n_0/2)/(2m)$ is the energy at the Fermi momentum, ϵ_{kin} is the free gas contribution, and the nucleon-nucleon interaction is parameterized by constants α, η for symmetric nuclear matter (SNM) and α_L, η_L for pure neutron matter (PNM).

Following Ref. [22] the SNM parameters α and η are fixed by requiring nuclear saturation, e.g. $\epsilon(1/2, n_0) = -16\,\text{MeV}$ and $P(1/2, n_0) = 0$ which results in

$$\alpha = \frac{3\,(4T_0 + 640/3)}{5T_0}, \tag{8.13}$$

$$\eta = \frac{3\,(2T_0 + 160)}{5T_0}, \tag{8.14}$$

for the parameters. The PNM parameters α_L and η_L are then fixed by the symmetry energy S_v and its density derivative L [22]

$$S_v = \frac{1}{8}\frac{\partial^2\epsilon(x,n)}{\partial x^2}\bigg|_{x=1/2,n=n_0}, \tag{8.15}$$

$$L = n_0\frac{3}{8}\frac{\partial^3\epsilon(x,n)}{\partial n\partial x^2}\bigg|_{x=1/2,n=n_0}, \tag{8.16}$$

and are given by

$$\alpha_L = \frac{6L - 24S_v + 3T_0\alpha + 4T_0}{6T_0}, \tag{8.17}$$

$$\eta_L = \frac{6L - 18S_v + 3T_0\eta + 2T_0}{6T_0}. \tag{8.18}$$

By varying S_v and L we can change the properties of neutron rich matter. This is shown in Fig. 8.3 where we use every combination of $L = 20, 40, 60, 80\,\text{MeV}$ and $S_v = 30, 33\,\text{MeV}$ to determine the region where proton drip is possible. We find that proton drip is robust for these variations.

To summarize, we find proton drip for calculations with chiral interactions at N^{3}LO and N^{2}LO and in addition with the functional Eq. (8.12) for a wide range of nuclear matter parameters.

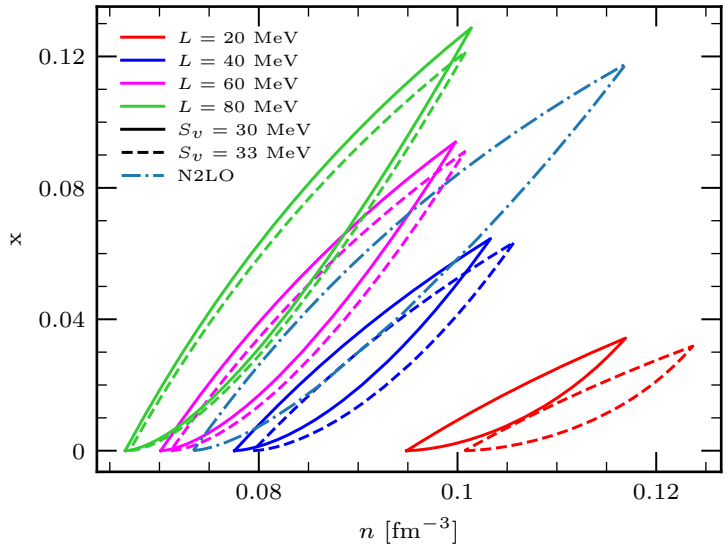

Figure 8.3: Robustness of the density-proton-fraction region where proton drip is possible. In addition to calculations at order N^{2}LO (dash-dotted line), results of the functional Eq. (8.12) for different $L = 20, 40, 60, 80$ MeV (colors) and different symmetry energies $S_v = 30, 33$ MeV (solid and dashed) are shown.

Furthermore, general arguments based on the density dependence of the kinetic energy and a generic potential suggest that proton drip is a general feature of the nuclear EOS [110].

9 Matter in beta equilibrium with muons

This chapter provides a more detailed investigation of the equation of state of matter in beta equilibrium. In contrast to Chapter 6, where only neutrons, protons, and electrons where included as degrees of freedom, this chapter also includes muons. Furthermore the focus is on providing input for astrophysical applications. Therefore, the speed of sound of matter in beta equilibrium is calculated and a additional focus is on providing better uncertainty estimates that include the MBPT uncertainties. The derivation of matter in beta equilibrium with muons follows Ref. [31] (see also supplemental material).

9.1 Composition

Thermodynamic quantities will be parameterized in terms of the total density n, proton fraction x, electron fraction x_e, and muon fraction x_μ defined as

$$n = n_n + n_p \,, \tag{9.1}$$

$$x = \frac{n_p}{n} \,, \tag{9.2}$$

$$x_e = \frac{n_e}{n} \,, \tag{9.3}$$

$$x_\mu = \frac{n_\mu}{n} \,. \tag{9.4}$$

Note that compared to chapter 6, where charge neutrality requires $x = x_e$, here electron fraction and proton fractions are in general different because of the presence of muons.

To determine the composition x, x_e, and x_μ given n we require that processes that convert neutrons into protons and electrons are in equilibrium

$$\mu_n(x, n) = \mu_p(x, n) + \mu_e(n_e) \,, \tag{9.5}$$

that processes that convert muon into electrons are in equilibrium

$$\mu_e(n_e) = \mu_\mu(n_\mu) \,, \tag{9.6}$$

and charge neutrality

$$n_p = n_e + n_\mu \,. \tag{9.7}$$

Given the proton density n_p one can solve Eqs. (9.6) and (9.7) to obtain n_e and n_μ and then solve Eq. (9.5) for n_p given the total density n.

Note that all chemical potentials include the rest mass, e.g., in the zero density limit we have $\mu_i(n_i = 0) = m_i$ where m_i is the rest mass of particle $i = n, p, e, \mu$. Equation (9.6) can only be solve when the electron chemical potential is larger than the muon rest mass. This is not possible at small densities where consequently the system only consists of neutrons, protons and electrons. We ignore Eq. (9.6) in this case and use $n_\mu = 0$.

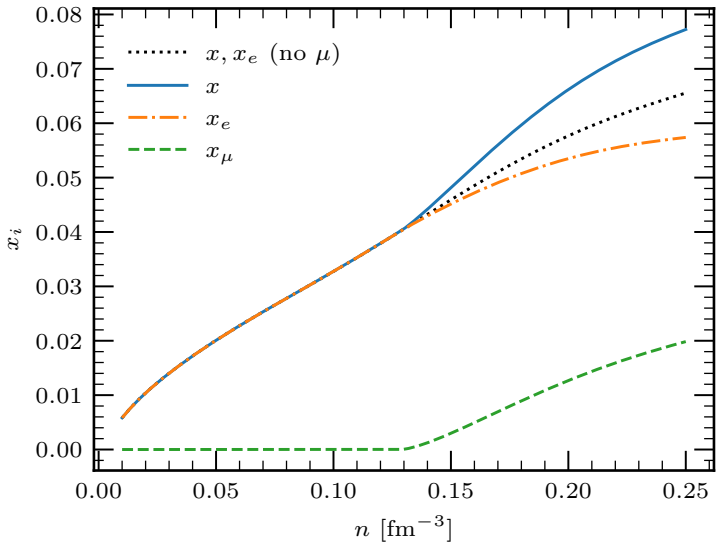

Figure 9.1: Composition of matter in beta equilibrium as a function of number density. The dotted line shows the proton fraction without including muons (with $x_e = x$, see chapter 6). The other lines who the proton fraction (solid), electron fraction (dash dotted), and the muon fraction (dashed).

Figure 9.1 show the composition of matter in beta-equilibrium including muons. The results are based on the 3rd-order MBPT calculations from Chapter 6 for the EMN450 N^{3}LO interaction. Muons start to contribute for $n \gtrsim 0.13\,\mathrm{fm}^{-3}$ where the electron chemical potential is larger than the muon rest mass $\mu_e \geq m_\mu$. As a comparison the composition without muons shown as black dotted line (where $x = x_e$). The non-zero muon concentration is compensated by smaller amount of electrons and a larger proton fraction.

9.2 Energy density and pressure

For astrophysical applications we are interested in the total energy density (including the rest mass)

$$\epsilon(n) = n\left(\frac{E_{\mathrm{nuc}}}{A}(x, n) + m_n\right) + \epsilon_e(n_e) + \epsilon_\mu(n_\mu)\,, \tag{9.8}$$

where E_{nuc}/A is the energy per particle of nucleons, m_n is the neutron rest mass, and $\epsilon_e(n_e)$ and $\epsilon_\mu(n_\mu)$ are the energies per volume of electrons and muons given by [31]

$$\epsilon_i(n_i) = \frac{m_i^4}{8\pi^2}\left(x_r(2x_r^2+1)\sqrt{x_r^2+1} - \ln\left(x_r + \sqrt{x_r^2+1}\right)\right), \tag{9.9}$$

$$x_r = (3\pi^2 n_i)^{1/3}/m_i\,. \tag{9.10}$$

Similarly, we define the total pressure as

$$P(n) = P_{\text{nuc}}(x,n) + P_e(n_e) + P_\mu(n_\mu)\,, \tag{9.11}$$

with nucleon, electron, and muon contributions.

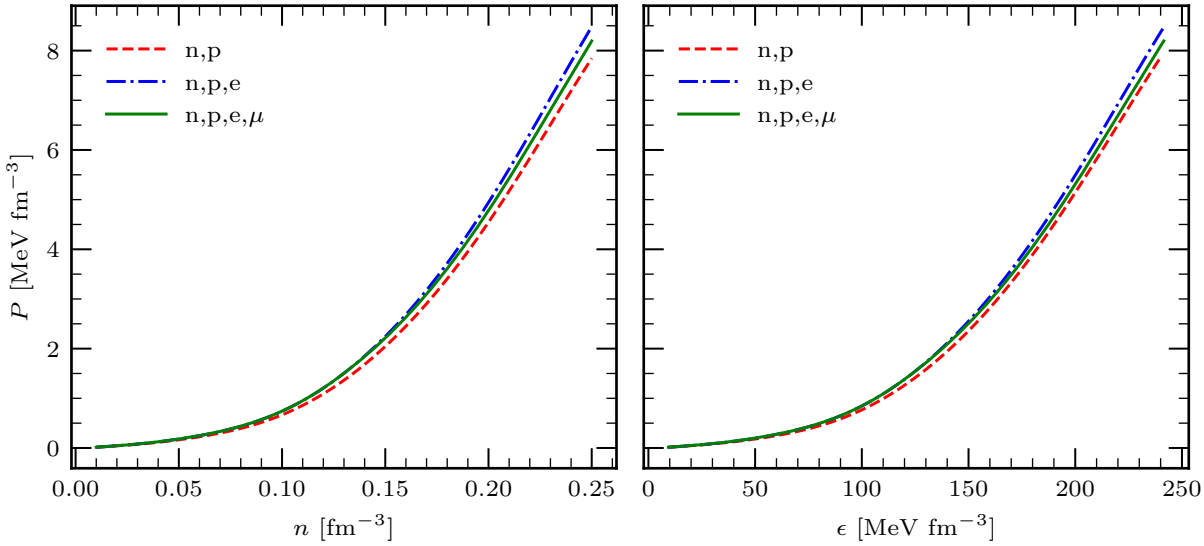

Figure 9.2: Pressure in beta equilibrium as a functions of number density (left) and energy density (right). Different lines show the contribution of the individual particles to the pressure: neutrons (n), protons (p), electrons (e), and muons (μ).

Figure 9.2 shows the total pressure as a function of number density and total pressure as function of total energy density. Different lines show contributions of the different particles. Lines with labels "n,p" and "n,p,e" do not include muons in the composition for all densities, e.g. $x_\mu = 0$. The impact of electrons is generally small. Including muons reduces the pressure contribution of electron, which is, however, compensated by non-zero muon contribution $P\mu$. In total also the contribution of muons is small compared to the nucleons.

9.3 Speed of sound

The speed of sound c_s^2 is defined as the derivative of the total pressure with respect to the total energy density [104]. In Chapter 6, we only looked at neutron matter (at constant proton

fraction) such that the derivative simplifies to (see, e.g. Ref. [104])

$$c_s^2 = \frac{\partial P}{\partial \varepsilon}\Big|_x = \frac{\partial P}{\partial n}\Big|_x \frac{\partial n}{\partial \varepsilon}\Big|_x = \frac{n}{P+\varepsilon}\frac{\partial P}{\partial n}\Big|_x . \tag{9.12}$$

For matter in beta equilibrium we can not assume constant proton fraction but have to use

$$c_s^2 = \frac{\partial P(x_{p,\beta}(\epsilon), x_{e,\beta}(\epsilon), x_{\mu,\beta}(\epsilon), n_\beta(\epsilon))}{\partial \epsilon}, \tag{9.13}$$

$$= \sum_{i=p,e,\mu} \frac{\partial P}{\partial x_i}\Big|_{x_{p,\beta}(\epsilon),x_{e,\beta}(\epsilon),x_{\mu,\beta}(\epsilon),n_\beta(\epsilon)} \frac{\partial x_{i,\beta}(\epsilon)}{\partial \epsilon} + \frac{\partial P}{\partial n}\Big|_{x_{p,\beta}(\epsilon),x_{e,\beta}(\epsilon),x_{\mu,\beta}(\epsilon),n_\beta(\epsilon)} \frac{\partial n_\beta(\epsilon)}{\partial \epsilon}, \tag{9.14}$$

which also contains derivatives with respect to the proton fraction x_p, electron fraction x_e, and muon fraction x_μ.

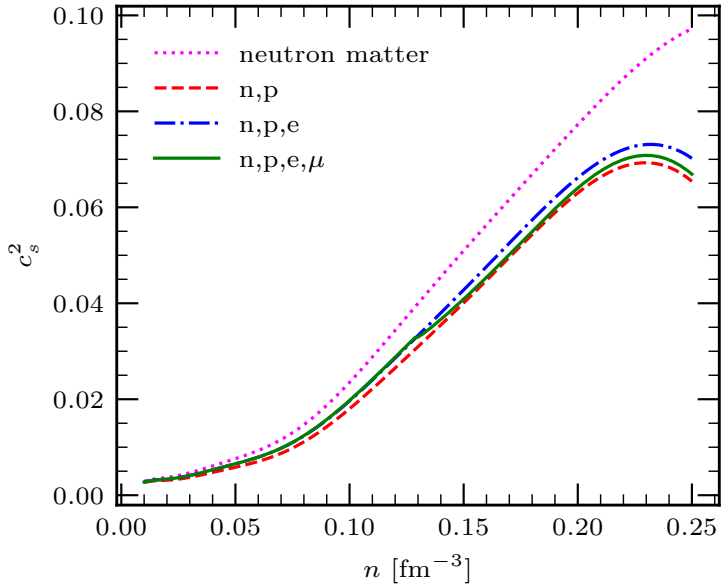

Figure 9.3: Speed of sound in beta equilibrium as function of number density. Lines are the same as in Fig. 9.2. In addition neutron matter is shown (dotted).

Fig. 9.3 shows the speed of sound squared determined from Eq. (9.14). Including the contribution of muons has a minor impact on the speed of sound. As a comparison the speed of sound of neutron matter of chapter 6 is shown in Fig. 9.3. The speed of sound in beta equilibrium decreases at some point resulting in a bump (maximum) around $n \approx 0.23\,\mathrm{fm}^{-3}$. This is in contrast to the results found for neutron matter. Note, however, that the bump is a small effect compared to the theoretical EFT and MBPT uncertainties, see Sec. 9.6.

9.4 Composition dependence

To test the sensitivity to composition x, x_e, x_μ in beta equilibrium we use P and ϵ from chiral EFT and determine the composition using the LS220 EOS (see chapter 6). The comparison of both approaches is shown in Fig. 9.4. Additionally a calculation that uses LS220 for P, ϵ and for

the composition is shown as comparison. The impact of the composition is much smaller than the impact of pressure and energy density on the speed of sound.

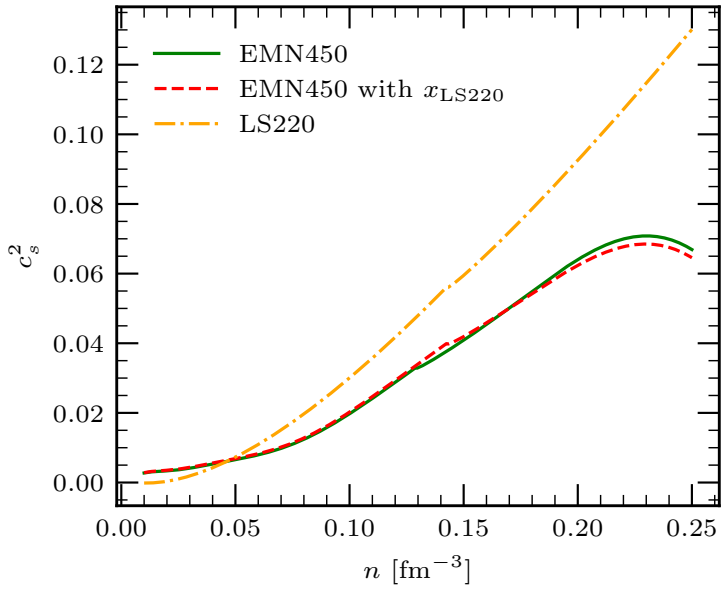

Figure 9.4: Speed of sound in beta equilibrium as function of number density. Shown is the full calculation with chiral EFT interactions (solid), a calculation where the speed of sound is calculated using chiral EFT interactions and the composition in beta equilibrium is taken from the LS220 EOS (dashed), and a calculations that uses the LS220 EOS for the speed of sound and the composition (dash dotted).

9.5 Asymmetry dependence

To test the dependence on the asymmetry we can expand the x dependence of the EOS in the asymmetry $\beta = 1 - 2x$

$$E(x,n) = a_0(n) + a_2(n)(1-2x)^2 + a_4(n)(1-2x)^4 + a_6(n)(1-2x)^6 + \dots\,, \tag{9.15}$$

where all odd terms vanish because we assume isospin symmetry. In a common approximations only the first two terms a_0 and a_2 of the expansion are considered, see e.g. Ref. [9]. They can be fixed by pure neutron matter (PNM) and symmetric nuclear matter (SNM) to obtain

$$E(x,n) = E_{\mathrm{SNM}}(n) + (E_{\mathrm{PNM}}(n) - E_{\mathrm{SNM}}(n))(1-2x)^2\,, \tag{9.16}$$

$$P(x,n) = P_{\mathrm{SNM}}(n) + (P_{\mathrm{PNM}}(n) - P_{\mathrm{SNM}}(n))(1-2x)^2\,, \tag{9.17}$$

$$\mu_p(x,n) - \mu_n(x,n) = \frac{\partial E}{\partial x} = -4(E_{\mathrm{PNM}}(n) - E_{\mathrm{SNM}}(n))(1-2x)\,. \tag{9.18}$$

In this approximation the EOS is quadratically interpolated between neutron matter and symmetric nuclear matter. Figure 9.5 shows a comparison of the full asymmetry dependence (labeled "Ref") and the quadratic interpolation (a_2, a_4).

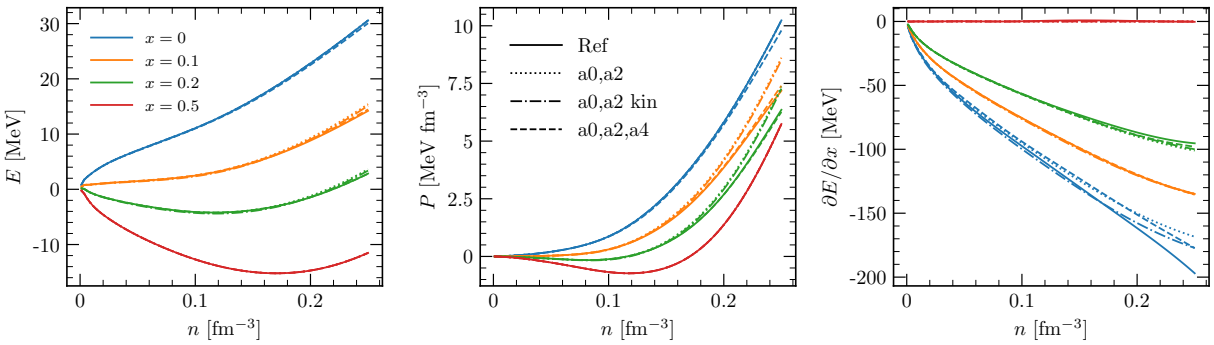

Figure 9.5: Energy per particle (left), pressure (middle), and energy per particle derivative $\partial E/\partial x$ as function of number density. Different colors mark different proton fractions $x = 0, 0.1, 0.2, 0.5$. Different linestyles show different approximations of the asymmetry dependence. The full calculations (Ref) is shown as solid lines. Including asymmetry coefficients up to second order Eq. (9.16) (a_0, a_2) as dotted, additionally treating the kinetic energy analytically Eq. (9.20) $(a_0, a_2$ kin) dash dotted. Finally including coefficients up to fourth order Eq. (9.21) (a_0, a_2, a_4) is shown as dashed lines.

Note that the kinetic energy (see e.g. Ref. [22]) has the asymmetry expansion

$$\frac{E_{FG}(x,n)}{T_0\,(n/n_0)^{2/3}} = \frac{3}{5} + \frac{1}{3}(1-2x)^2 + \frac{1}{81}(1-2x)^4 + \frac{7}{2187}(1-2x)^6 + \frac{26}{19683}(1-2x)^8 + \dots \quad (9.19)$$

where $n_0 = 0.16\,\mathrm{fm}^{-3}$ is the saturation density and $T_0 = \left(3\pi^2 n_0/2\right)/(2m) \approx 36.84\,\mathrm{MeV}$. At saturation density the fourth order coefficient is given by $T_0/81 \approx 454.8\,\mathrm{keV}$. Therefore it might be advantageous to treat the free gas analytically and only quadratically interpolate the interaction energy $E_{\mathrm{int}} = E - E_{\mathrm{FG}}$, e.g.

$$E(x,n) = E_{\mathrm{FG}}(x,n) + E_{\mathrm{SNM,\,int}}(n) + (E_{\mathrm{PNM,\,int}}(n) - E_{\mathrm{SNM,\,int}}(n))(1-2x)^2\,, \quad (9.20)$$

to improve the approximation quality. The approximation with kinetic energy treated analytically is also shown in Fig. 9.5.

Furthermore higher order terms in the asymmetry expansion can be included to test the convergence, e.g. up to forth order

$$E(x,n) = E_{\mathrm{SNM}}(n) + a_2(n)(1-2x)^2 + a_4(n)(1-2x)^4\,, \quad (9.21)$$

$$P(x,n) = P_{\mathrm{SNM}}(n) + n^2 a_2'(n)(1-2x)^2 + n^2 a_4'(n)(1-2x)^4\,, \quad (9.22)$$

$$\mu_p(x,n) - \mu_n(x,n) = \frac{\partial E}{\partial x} = -4a_2(n)(1-2x) - 8a_4(n)(1-2x)^3\,. \quad (9.23)$$

where $a_2(n)$ and $a_4(n)$ have to be determined from the full calculations. They are fitted at fixed density n to our GP emulator by using as least-square procedure.

The extracted coefficients are shown in Fig. 9.6. As a comparison also the asymmetry coefficients of the free gas Eq. (9.19) and the symmetry energy $E_{\mathrm{PNM}} - E_{\mathrm{SNM}}$ are shown. One can see that at higher densities a_2 deviates from the symmetry energy and the fourth order coefficient

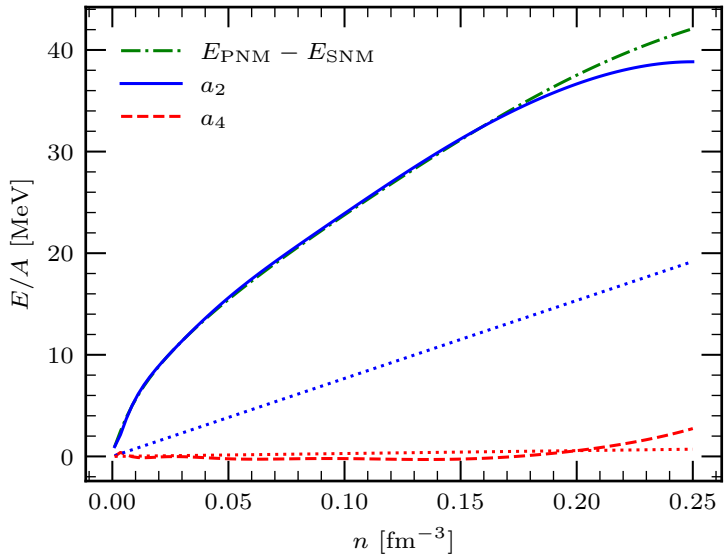

Figure 9.6: Second (solid) and fourth (dashed) asymmetry coefficient as a function of number density. As a comparison, the contributions from the free gas Eq. (9.19) to a_2 and a_4 are shown as dotted lines with the same colors. The symmetry energy (difference of neutron matter to symmetric nuclear matter) is shown as the dash-dotted line.

a_4 becomes sizeable.

The approximation where the fourth coefficient is included is also shown in Fig. 9.5. Notice that while all approximations produce reasonable energies, the approximation quality of the pressure is significantly worse for small non-zero proton fractions, e.g. $x = 0.1$, when a_4 is not included.

Figure 9.7 shows the impact of the second order approximation Eq. (9.16) (denoted by single primes, e.g. EMN450′) together with the fourth order approximation Eq. (9.21) (denoted with double primes, e.g. EMN450″) on the composition of beta equilibrium and the pressure and Fig. 9.8 shown the impact on the speed of sound. The speed of sound in the quadratic approximation Eq. (9.16) is also included for a different cutoff $\Lambda = 500\,\mathrm{MeV}$ as a comparison (EMN500′).

The speed of sound in beta equilibrium depends on $\partial P/\partial x$ (and therefore on $a_2'(n)$ and $a_4'(n)$) and $\partial P/\partial n$ (and therefore even on $a_2'(n)$, $a_4'(n)$, $a_2''(n)$, and $a_4''(n)$) and is more sensitive to the asymmetry approximation. While the impact of different approximations in small on the composition and pressure in beta equilibrium, it can be significant for the speed of sound. One can see that with only including a_2, the speed of sound does not have the bump at higher densities. The bump of the full calculation can only be reproduced by including a_4. Analytically treating the free gas Eq. (9.20) (EMN450′ (+kin)) only has a small effect on the approximation quality.

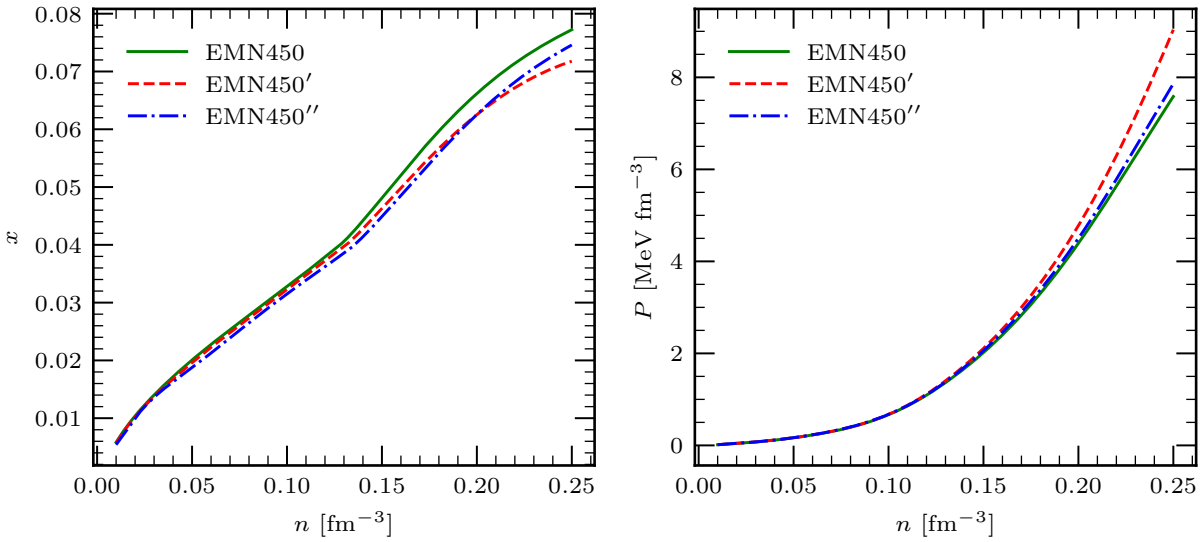

Figure 9.7: Proton fraction and pressure in beta equilibrium as function of the number density. Different linestyles show the full calculations EMN450 (solid) and different approximations EMN450′ given by Eq. (9.16) (dashed), and EMN450″ Eq. (9.21) (dash dotted).

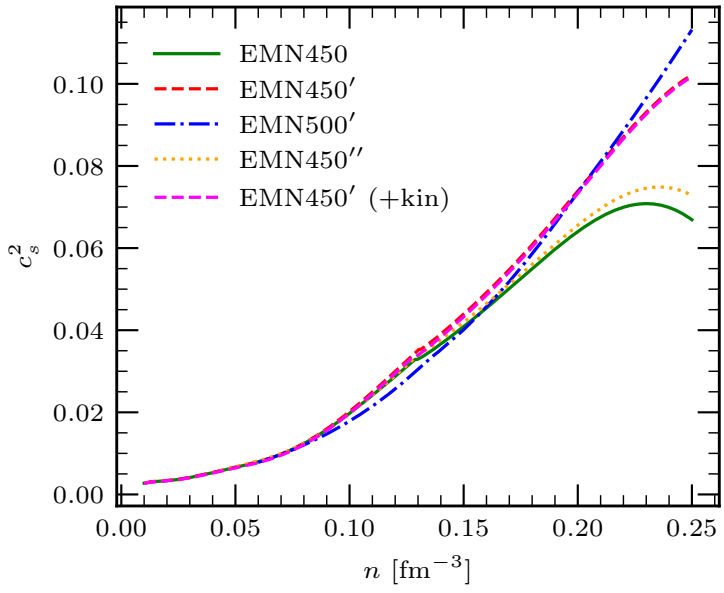

Figure 9.8: Speed of sound in beta equilibrium as function of the number density. In addition to the full calculation (solid) various approximations are shown (see text). Note that the lines labeled "EMN450″" and "EMN450′ (+kin)" overlap. As a comparison also calculations with a cutoff of $\Lambda = 500\,\mathrm{MeV}$ are shown.

9.6 Theoretical uncertainty estimates

9.6.1 EFT uncertainty estimates

EFT uncertainties are estimates as in Chapter 6 based on the EKM prescription [54]

$$\Delta X^{(j)} = Q \cdot \max\left(|X^{(j)} - X^{(j-1)}|, \Delta X^{(j-1)}\right) , \tag{9.24}$$

$$\Delta X^{\mathrm{LO}} = 0 , \tag{9.25}$$

where the momentum scale is determined by highest order composition

$$Q = Q\left(n, x = x^{(j)}_{\beta\text{-eq.}}(n)\right) . \tag{9.26}$$

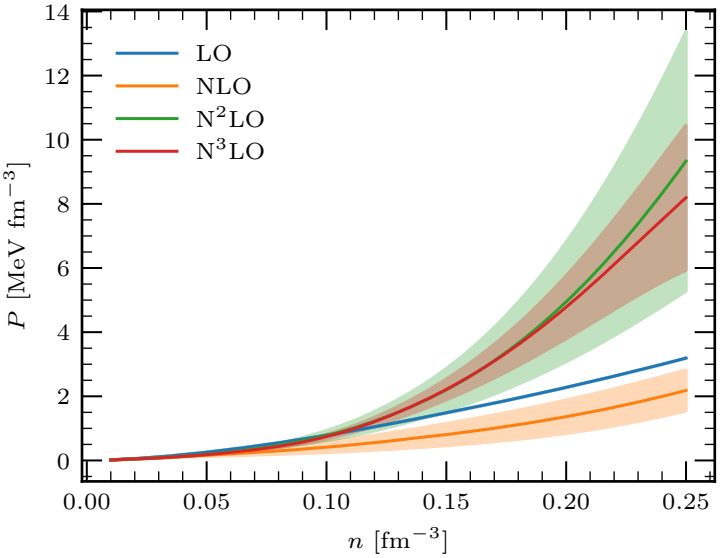

Figure 9.9: Pressure in beta equilibrium as a function of number density. Bands show EFT uncertainty estimates for different EFT orders (colors).

Figures 9.9 and 9.10 show EFT uncertainty estimates for the pressure and speed of sound in beta equilibrium for different EFT orders. Note that the LO error estimates is chosen to be zero (see chapter 5). The NLO uncertainties are underestimated, likely because of the missing LO uncertainties. Furthermore the LO and NLO lines of the speed of sound cross at higher densities, leading to further artifacts for this uncertainty with the EKM method.

The bump of the speed of sound is only visible for N^{3}LO and not for lower EFT orders. Note that at at $n \gtrsim 0.125\,\mathrm{fm}^{-3}$ muons start to appear and cause the sudden change in c_s^2

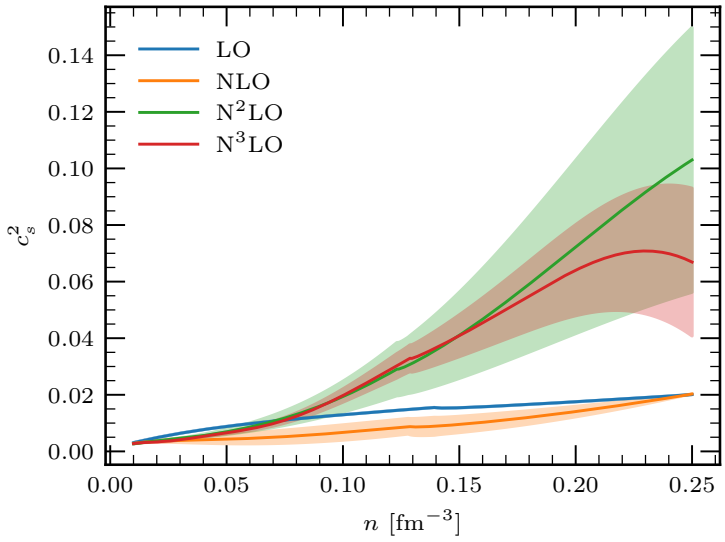

Figure 9.10: Speed of sound in beta equilibrium as a function of number density. Bands show EFT uncertainty estimates for different EFT orders (colors).

9.6.2 Many-body convergence

The next plot shows the MBPT convergence of the total energy per particle and the total pressure in beta equilibrium. The MBPT convergence of the pressure is slower then expected (significantly slower than for the energy).

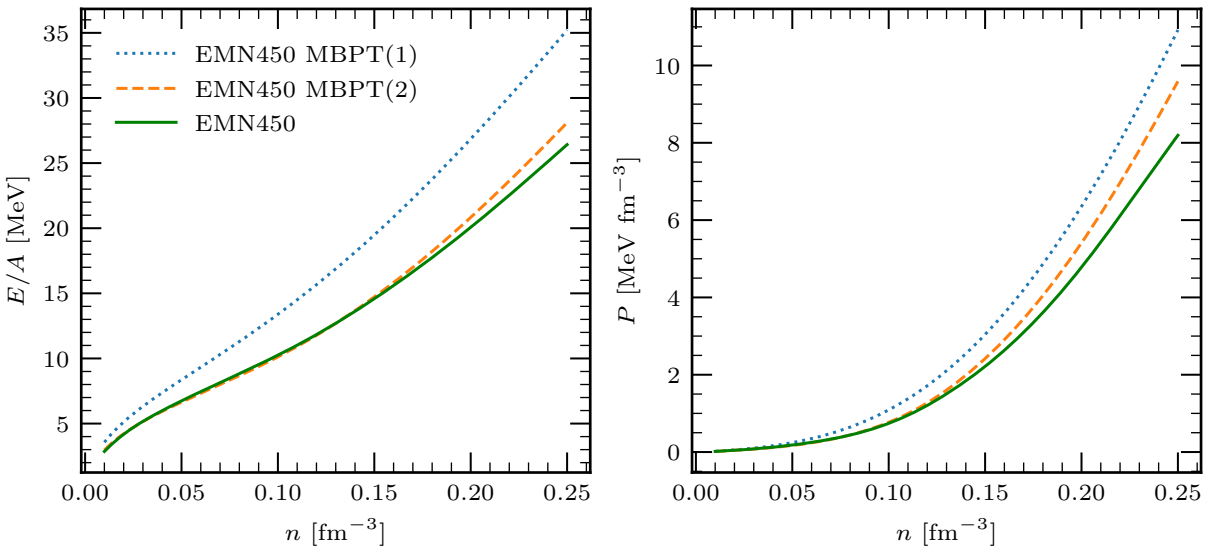

Figure 9.11: Energy per particle (left) and pressure (right) in beta equilibrium as function of number density. Different linestyles show MBPT(3) (solid), MBPT(2) (dashed), and MBPT(1) (dotted).

The following plot shows the MBPT convergence of the speed of sound. The bump is only visible for MBPT(3) and it seems that the MBPT uncertainty is larger than expected at high densities (difference of MBPT(2) and MBPT(3) is larger then difference of MBPT(1) and MBPT(2)). Also note that there are no muon for MBPT(1).

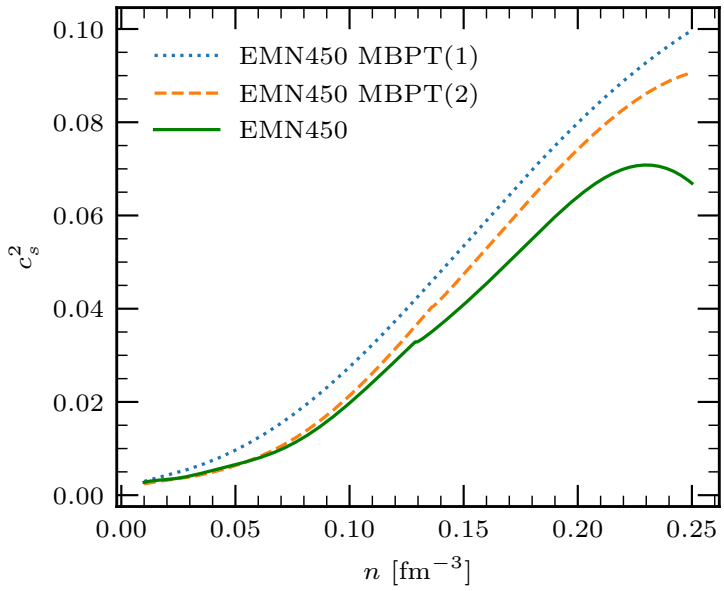

Figure 9.12: Speed of sound in beta equilibrium as function of number density. Linestyles are the same as in Fig. 9.11.

9.6.3 Combined EFT and MBPT errors

We estimate the MBPT uncertainties at order MBPT(3) by using the difference of MBPT(3) and MBPT(2), e.g.

$$\Delta_{\mathrm{MBPT}} c_s^2(n) = \left| c^2_{s,\mathrm{MBPT(3)}}(n) - c^2_{s,\mathrm{MBPT(2)}}(n) \right| . \tag{9.27}$$

This is a conservative estimate of the MBPT uncertainties, e.g. note that the difference of MBPT(2) and MBPT(1) is much larger than the actual MBPT(3) contribution. The combined uncertainty is determined by

$$\Delta_{\mathrm{total}} c_s^2(n) = \Delta_{\mathrm{EFT}} c_s^2(n) + \Delta_{\mathrm{MBPT}} c_s^2(n) \tag{9.28}$$

as the sum of the individual contributions. The resulting uncertainty estimates for the speed of sound are shown in Fig. 9.13. Note, this is again a conservative uncertainty estimate. A statistical treatment that includes MBPT and EFT uncertainties as independent error sources would be desirable in the future.

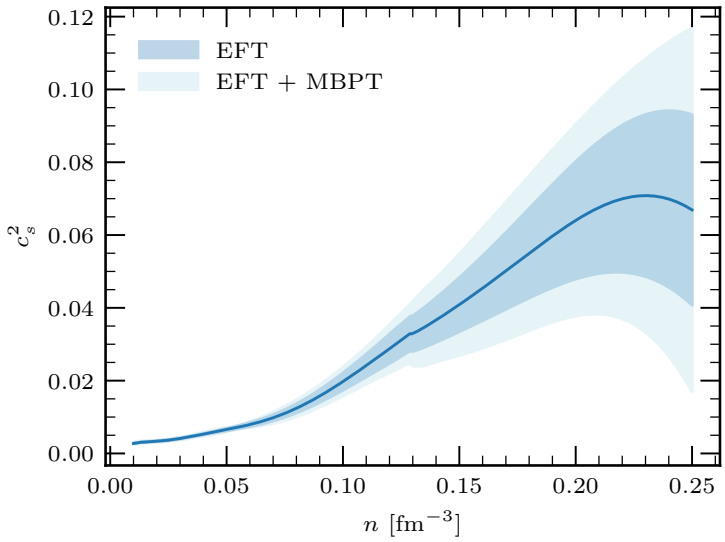

Figure 9.13: Speed of sound in beta equilibrium as function of number density. Error bars show EFT uncertainty estimates (dark blue) and combined EFT and MBPT uncertainty estimates (light blue).

10 Summary and outlook

In this thesis, we studied the nuclear matter EOS at finite temperature and arbitrary proton fraction based on nuclear interactions from chiral effective field theory using many-body perturbation theory and Gaussian processes. Parts of this chapter have already been published in Refs. [1, 59].

We discussed the many-body formalism in Chapter 3 for a general partitioning of the Hamiltonian and the contribution of anomalous diagrams at finite temperature. The many-body expansion simplifies when using a HF partitioning and we performed calculations in this scheme. In contrast to previous MBPT studies, we included the full HF self-energy momentum dependence and do not employ normal-ordering approximations for the 3N interactions. For the practical calculations we employed Monte Carlo integration techniques that allow to evaluate highly dimensional integrals, involved in the MBPT contributions, very efficiently.

We then presented a systematic study of the thermodynamics of neutron matter based on a range of chiral EFT interactions in Chapter 5. This included SRG evolved NN interactions at $\mathrm{N^3LO}$ with unevolved 3N interactions at $\mathrm{N^2LO}$ as well as for the first time consistently SRG-evolved interactions in nuclear matter calculations. In addition, we studied the EMN potentials at $\mathrm{N^2LO}$ and $\mathrm{N^3LO}$ with consistent 3N interactions constraint by nuclear matter saturation. Our results based on the consistently SRG-evolved interactions exhibit a remarkably small SRG scale dependence in neutron matter over the full range of temperatures, which indicates that the effects of induced higher-body forces are very small for these interactions and also that the many-body calculation is well converged. In addition, we studied the theoretical uncertainties due to the truncation of the chiral expansion using the EKM prescription and employing the recently developed Bayesian framework based on Gaussian processes. Our results show that both methods provide very similar error estimates in neutron matter. The temperature dependence of different thermodynamic quantities was studied in detail. We found that the dominant contribution to the temperature dependence originates from the Fermi gas contribution, and that the thermal interaction part is well captured by using a density-dependent effective mass. This was shown by studying the thermal index, which allows to diagnose in a simple way thermal interaction effects.

In Chapter 6 we then presented first microscopic calculations of the EOS at arbitrary proton fractions and finite temperature based on the same chiral NN and 3N interactions to $\mathrm{N^3LO}$, including uncertainty estimates from the many-body calculation and the chiral expansion. For this an emulator of the interaction free energy per particle was constructed using Gaussian processes. We demonstrated that this enables an efficient and accurate evaluation of the EOS and thermodynamic derivatives for arbitrary values of n, x, and T, where we considered the ranges $n \leqslant 0.25\,\mathrm{fm}^{-3}$, $x \leqslant 0.5$, and $T \leqslant 20\,\mathrm{MeV}$. The EFT uncertainties dominate over the

MBPT uncertainties for these nuclear densities. We studied in detail the dependence of the free energy and the pressure on proton fraction and temperature, and found that the pressure at higher densities decreases with increasing temperature, thus exhibiting a negative thermal expansion. The GP emulator allowed us to calculate the EOS in beta equilibrium directly without parametrizations between neutron and symmetric matter. The resulting N^3LO neutron star EOS exhibited a systematic chiral EFT behavior over the full range ($n \leqslant 0.25\,\mathrm{fm}^{-3}$) and significantly improved the uncertainties over previous EOS bands, preferring larger values for the pressure. Moreover, we presented first microscopic results for the speed of sound and the symmetry energy at finite temperature.

We then studied the liquid-gas phase transition in symmetric nuclear matter ($x = 0.5$) in Chapter 7. First preliminary results for the critical temperature and density were determined. By using a Maxwell construction, the physical EOS (in particular pressure, chemical potential, and free energy) could be reconstructed. Finally, we presented the phase diagram for chiral interactions at N^2LO and N^3LO. In the future it would be desirable to determine EFT uncertainties for the phase diagram, the critical density, and the critical temperature. This will require statistical methods for the EFT uncertainties and will allow to determine distributions for those quantities.

In Chapter 8 we investigated phase coexistence at low proton concentrations at $T = 0$. In particular we explored the coexistence of neutron matter with nuclear matter (neutron drip) and the possibility of coexistence of nuclear matter with nuclear matter (proton drip). We find that proton drip is possible for all studied microscopic calculations based on chiral NN and 3N interactions. Furthermore, variations of nuclear matter properties using a phenomenological EOS functional and analytical considerations suggest that our findings of proton drip are robust. The phase diagram as a function of density and proton fraction was presented.

As a last application we extended our calculations of matter in beta equilibrium to also include muons as a degree of freedom in Chapter 9. We determined the pressure, energy density, and speed of sound in beta equilibrium and found only a minor impact of muons. An analysis of the asymmetry dependence was presented. Finally we provided theoretical EFT and MBPT uncertainties for the speed of sound. These new speed of sound error bands can be used as a basis to determine the neutron star EOS.

This thesis lays the foundation for microscopic studies of the thermodynamics of asymmetric nuclear matter based on chiral NN and 3N interactions. It will be interesting to explore the resulting EOSs in astrophysical simulations of core-collapse supernovae and neutron star mergers. In particular, the thermal effects found are very different from phenomenological EOS tables and we provided results for the asymmetry dependence at finite temperatures for the first time.

Bibliography

[1] J. Keller, K. Hebeler, and A. Schwenk, Phys. Rev. Lett. **130**, 072701 (2023).

[2] J. M. Lattimer and Y. Lim, Astrophys. J. **771**, 51 (2013).

[3] K. Hebeler, J. Holt, J. Menéndez, and A. Schwenk, Annu. Rev. Nucl. Part. Sci. **65**, 457 (2015).

[4] J. E. Lynn, I. Tews, S. Gandolfi, and A. Lovato, Annu. Rev. Nucl. Part. Sci. **69**, 279 (2019).

[5] C. Drischler, J. W. Holt, and C. Wellenhofer, Annu. Rev. Nucl. Part. Sci. **71**, 403 (2021).

[6] J. M. Lattimer, Annu. Rev. Nucl. Part. Sci. **71**, 433 (2021).

[7] F. Schwabl, *Statistische Mechanik* (Springer, 2006).

[8] R. K. Pathria and P. D. Beale, *Statistical mechanics* (Elsevier, 2011).

[9] J. M. Lattimer, Journal of Physics: Conference Series **2536**, 012009 (2023).

[10] R. Somasundaram, C. Drischler, I. Tews, and J. Margueron, Phys. Rev. C **103**, 045803 (2021).

[11] C. Wellenhofer, J. W. Holt, and N. Kaiser, Phys. Rev. C **93**, 055802 (2016).

[12] M. Oertel, M. Hempel, T. Klähn, and S. Typel, Rev. Mod. Phys. **89**, 015007 (2017).

[13] J. M. Lattimer, Particles **6**, 30 (2023).

[14] X. Roca-Maza and N. Paar, Prog. Part. Nucl. Phys. **101**, 96 (2018).

[15] I. Vidaña, Eur. Phys. J. Plus **133**, 445 (2018).

[16] C. Drischler, R. J. Furnstahl, J. A. Melendez, and D. R. Phillips, Phys. Rev. Lett. **125**, 202702 (2020).

[17] C. Wellenhofer, J. W. Holt, N. Kaiser, and W. Weise, Phys. Rev. C **89**, 064009 (2014).

[18] G. Baym and C. Pethick, Ann. Rev. Nucl. Part. Sci. **25**, 27 (1975).

[19] C. J. Pethick and D. G. Ravenhall, Ann. Rev. Nucl. Part. Sci. **45**, 429 (1995).

[20] R. C. Tolman, Phys. Rev. **55**, 364 (1939).

[21] J. R. Oppenheimer and G. M. Volkoff, Phys. Rev. **55**, 374 (1939).

[22] K. Hebeler, J. M. Lattimer, C. J. Pethick, and A. Schwenk, Astrophys. J. **773**, 11 (2013).

[23] E. Annala, T. Gorda, A. Kurkela, and A. Vuorinen, Phys. Rev. Lett. **120**, 172703 (2018).

[24] E. R. Most, L. R. Weih, L. Rezzolla, and J. Schaffner-Bielich, Phys. Rev. Lett. **120**, 261103 (2018).

[25] I. Tews, J. Margueron, and S. Reddy, Phys. Rev. C **98**, 045804 (2018).

[26] Y. Lim and J. W. Holt, Phys. Rev. Lett. **121**, 062701 (2018).

[27] C. D. Capano, I. Tews, S. M. Brown, B. Margalit, S. De, S. Kumar, D. A. Brown, B. Krishnan, and S. Reddy, Nature Astron. **4**, 625 (2020).

[28] R. Essick, I. Tews, P. Landry, S. Reddy, and D. E. Holz, Phys. Rev. C **102**, 055803 (2020).

[29] T. Dietrich, M. W. Coughlin, P. T. H. Pang, M. Bulla, J. Heinzel, L. Issa, I. Tews, and S. Antier, Science **370**, 1450 (2020).

[30] G. Raaijmakers, S. K. Greif, K. Hebeler, T. Hinderer, S. Nissanke, A. Schwenk, T. E. Riley, A. L. Watts, J. M. Lattimer, and W. C. G. Ho, Astrophys. J. Lett. **918**, L29 (2021).

[31] R. Essick, I. Tews, P. Landry, and A. Schwenk, Phys. Rev. Lett. **127**, 192701 (2021).

[32] C. Drischler, S. Han, J. M. Lattimer, M. Prakash, S. Reddy, and T. Zhao, Phys. Rev. C **103**, 045808 (2021).

[33] S. Huth, P. T. H. Pang, I. Tews, T. Dietrich, A. Le Fèvre, A. Schwenk, W. Trautmann, K. Agarwal, M. Bulla, M. W. Coughlin, et al., Nature **606**, 276 (2022).

[34] H.-T. Janka, Ann. Rev. Nucl. Part. Sci. **62**, 407 (2012).

[35] S. Bacca, K. Hally, M. Liebendörfer, A. Perego, C. J. Pethick, and A. Schwenk, Astrophys. J. **758**, 34 (2012).

[36] H. Yasin, S. Schäfer, A. Arcones, and A. Schwenk, Phys. Rev. Lett. **124**, 092701 (2020).

[37] M. Jacobi, F. M. Guercilena, S. Huth, G. Ricigliano, A. Arcones, and A. Schwenk (2023), `arXiv:2309.09233`.

[38] A. Kurkela, P. Romatschke, and A. Vuorinen, Phys. Rev. D **81**, 105021 (2010).

[39] E. S. Fraga, A. Kurkela, and A. Vuorinen, Astrophys. J. Lett. **781**, L25 (2014).

[40] E. Epelbaum, H.-W. Hammer, and U.-G. Meißner, Rev. Mod. Phys. **81**, 1773 (2009).

[41] R. Machleidt and D. Entem, Phys. Rep. **503**, 1 (2011).

[42] H.-W. Hammer, S. König, and U. van Kolck, Rev. Mod. Phys. **92**, 025004 (2020).

[43] H.-W. Hammer, A. Nogga, and A. Schwenk, Rev. Mod. Phys. **85**, 197 (2013).

[44] K. Hebeler, Phys. Rept. **890**, 1 (2021).

[45] U. van Kolck, Phys. Rev. C **49**, 2932 (1994).

[46] E. Epelbaum, A. Nogga, W. Gloeckle, H. Kamada, U. G. Meissner, and H. Witala, Phys. Rev. C **66**, 064001 (2002).

[47] T. Krüger, I. Tews, K. Hebeler, and A. Schwenk, Phys. Rev. C **88**, 025802 (2013).

[48] S. Bogner, R. Furnstahl, and R. Perry, Phys. Rev. C **75**, 061001 (2007).

[49] C. Drischler, K. Hebeler, and A. Schwenk, Phys. Rev. Lett. **122**, 042501 (2019).

[50] K. Hebeler, H. Krebs, E. Epelbaum, J. Golak, and R. Skibiński, Phys. Rev. C **91**, 044001 (2015).

[51] K. Hebeler, *private communication* (2019).

[52] D. R. Entem, R. Machleidt, and Y. Nosyk, Phys. Rev. C **96**, 024004 (2017).

[53] R. J. Furnstahl, N. Klco, D. R. Phillips, and S. Wesolowski, Phys. Rev. C **92**, 024005 (2015).

[54] E. Epelbaum, H. Krebs, and U. Meißner, Eur. Phys. J. A **51**, 53 (2015).

[55] J. A. Melendez, R. J. Furnstahl, D. R. Phillips, M. T. Pratola, and S. Wesolowski, Phys. Rev. C **100**, 044001 (2019).

[56] C. Drischler, J. A. Melendez, R. J. Furnstahl, and D. R. Phillips, Phys. Rev. C **102**, 054315 (2020).

[57] A. L. Fetter and J. D. Walecka, *Quantum Theory of Many-Particle Systems* (McGraw-Hill, New York, 1972).

[58] J. W. Negele and H. Orland, *Quantum Many-Particle Systems* (Westview Press, Boulder, 1998).

[59] J. Keller, C. Wellenhofer, K. Hebeler, and A. Schwenk, Phys. Rev. C **103**, 055806 (2021).

[60] C. Wellenhofer, Phys. Rev. C **99**, 065811 (2019).

[61] K. Hebeler and A. Schwenk, Phys. Rev. C **82**, 014314 (2010).

[62] L. Tolos, B. Friman, and A. Schwenk, Nucl. Phys. A **806**, 105 (2008).

[63] W. Kohn and J. M. Luttinger, Phys. Rev. **118**, 41 (1960).

[64] A. Dyhdalo, R. J. Furnstahl, K. Hebeler, and I. Tews, Phys. Rev. C **94**, 034001 (2016).

[65] J. M. Luttinger and J. C. Ward, Phys. Rev. **118**, 1417 (1960).

[66] S. K. Bogner, A. Schwenk, R. J. Furnstahl, and A. Nogga, Nucl. Phys. A **763**, 59 (2005).

[67] A. Tichai, J. Langhammer, S. Binder, and R. Roth, Phys. Lett. B **756**, 283 (2016).

[68] C. E. Rasmussen and C. K. I. Williams, *Gaussian Processes for Machine Learning* (MIT Press, Cambridge, 2005).

[69] D. J. Mackay, *Introduction To Gaussian Processes, Lecture Notes* (1998).

[70] K. Hebeler, S. K. Bogner, R. J. Furnstahl, A. Nogga, and A. Schwenk, Phys. Rev. C **83**, 031301 (2011).

[71] I. Tews, T. Krüger, K. Hebeler, and A. Schwenk, Phys. Rev. Lett. **110**, 032504 (2013).

[72] J. W. Holt, N. Kaiser, and W. Weise, Prog. Part. Nucl. Phys. **73**, 35 (2013).

[73] A. Carbone, A. Polls, and A. Rios, Phys. Rev. C **88**, 044302 (2013).

[74] G. Hagen, T. Papenbrock, A. Ekström, K. Wendt, G. Baardsen, S. Gandolfi, M. Hjorth-Jensen, and C. J. Horowitz, Phys. Rev. C **89**, 014319 (2014).

[75] L. Coraggio, J. W. Holt, N. Itaco, R. Machleidt, L. E. Marcucci, and F. Sammarruca, Phys. Rev. C **89**, 044321 (2014).

[76] J. E. Lynn, I. Tews, J. Carlson, S. Gandolfi, A. Gezerlis, K. E. Schmidt, and A. Schwenk, Phys. Rev. Lett. **116**, 062501 (2016).

[77] C. Drischler, K. Hebeler, and A. Schwenk, Phys. Rev. C **93**, 054314 (2016).

[78] C. Drischler, A. Carbone, K. Hebeler, and A. Schwenk, Phys. Rev. C **94**, 054307 (2016).

[79] A. Ekström, G. Hagen, T. D. Morris, T. Papenbrock, and P. D. Schwartz, Phys. Rev. C **97**, 024332 (2018).

[80] D. Logoteta, Phys. Rev. C **100**, 045803 (2019).

[81] A. S. Schneider, L. F. Roberts, C. D. Ott, and E. O'Connor, Phys. Rev. C **100**, 055802 (2019).

[82] A. Bauswein, H.-T. Janka, and R. Oechslin, Phys. Rev. D **82**, 084043 (2010).

[83] S. Huth, C. Wellenhofer, and A. Schwenk, Phys. Rev. C **103**, 025803 (2021).

[84] W. Zuo, Z. Li, A. Li, and U. Lombardo, Nucl. Phys. A **745**, 34 (2004).

[85] B. Friedman and V. Pandharipande, Nucl. Phys. A **361**, 502 (1981).

[86] S. Fiorilla, N. Kaiser, and W. Weise, Nucl. Phys. A **880**, 65 (2012).

[87] C. Wellenhofer, J. W. Holt, and N. Kaiser, Phys. Rev. C **92**, 015801 (2015).

[88] A. Carbone, A. Polls, and A. Rios, Phys. Rev. C **98**, 025804 (2018).

[89] A. Carbone, Phys. Rev. Res. **2**, 023227 (2020).

[90] A. Rios, Front. Phys. **8**, 387 (2020).

[91] B.-N. Lu, N. Li, S. Elhatisari, D. Lee, J. E. Drut, T. A. Lähde, E. Epelbaum, and U.-G. Meißner, Phys. Rev. Lett. **125**, 192502 (2020).

[92] J. W. Holt, N. Kaiser, and W. Weise, Phys. Rev. C **81**, 024002 (2010).

[93] S. K. Bogner, R. J. Furnstahl, and A. Schwenk, Prog. Part. Nucl. Phys. **65**, 94 (2010).

[94] E. D. Jurgenson, P. Navrátil, and R. J. Furnstahl, Phys. Rev. Lett. **103**, 082501 (2009).

[95] E. D. Jurgenson, P. Navrátil, and R. J. Furnstahl, Phys. Rev. C **83**, 034301 (2011).

[96] R. Roth, J. Langhammer, A. Calci, S. Binder, and P. Navrátil, Phys. Rev. Lett. **107**, 072501 (2011).

[97] R. Roth, A. Calci, J. Langhammer, and S. Binder, Phys. Rev. C **90**, 024325 (2014).

[98] D. R. Entem and R. Machleidt, Phys. Rev. C **68**, 041001 (2003).

[99] K. Hebeler, Phys. Rev. C **85**, 021002(R) (2012).

[100] G. P. Lepage, J. Comp. Phys. **27**, 192 (1978).

[101] T. Hahn, Comp. Phys. Comm. **168**, 78 (2005).

[102] A. Carbone and A. Schwenk, Phys. Rev. C **100**, 025805 (2019).

[103] C. Drischler, J. A. Melendez, R. J. Furnstahl, and D. R. Phillips, `https://github.com/buqeye/nuclear-matter-convergence/` (2020).

[104] C. Constantinou, B. Muccioli, M. Prakash, and J. M. Lattimer, Phys. Rev. C **92**, 025801 (2015).

[105] A. Mignone and J. C. McKinney, Mon. Not. Roy. Astron. Soc. **378**, 1118 (2007).

[106] C. J. Horowitz and A. Schwenk, Phys. Lett. B **638**, 153 (2006).

[107] C. J. Horowitz and A. Schwenk, Nucl. Phys. A **776**, 55 (2006).

[108] M. A. Chilenski, M. Greenwald, Y. Marzouk, N. T. Howard, A. E. White, J. E. Rice, and J. R. Walk, Nucl. Fusion **55**, 023012 (2015).

[109] J. M. Lattimer and F. D. Swesty, Nucl. Phys. A **535**, 331 (1991).

[110] C. Pethick, *private communication* (2023).

Acknowledgment

At the end of this thesis I want to thank everybody that supported me during my time at TU Darmstadt. First of all, I want to thank my thesis advisor Achim Schwenk for giving me the opportunity to do research on this interesting topic, for the many useful discussions we had and for providing the encouragement to finish this thesis. I want to thank my co-advisor Kai Hebeler for all the (sometimes very technical) discussions we had. I want to thank Achim Schwenk and Kai Hebeler for providing feedback on this thesis. I want to thank Almudena Arcones for agreeing on short notice to be an examiner for this thesis. I want to thank Max Jacobi and all the people of the STRONGINT group for creating a nice environment to work in. This work is supported in part by the Deutsche Forschungsgemeinschaft (DFG, German Research Foundation) – Project-Id 279384907 – SFB 1245.

Erklärungen laut Promotionsordnung

§8 Abs. 1 lit. c PromO
Ich versichere hiermit, dass die elektronische Version meiner Dissertation mit der schriftlichen Version übereinstimmt.

§8 Abs. 1 lit. d PromO
Ich versichere hiermit, dass zu einem vorherigen Zeitpunkt noch keine Promotion versucht wurde. In diesem Fall sind nähere Angaben über Zeitpunkt, Hochschule, Dissertationsthema und Ergebnis dieses Versuchs mitzuteilen.

§9 Abs. 1 PromO
Ich versichere hiermit, dass die vorliegende Dissertation selbstständig und nur unter Verwendung der angegebenen Quellen verfasst wurde.

§9 Abs. 2 PromO
Die Arbeit hat bisher noch nicht zu Prüfungszwecken gedient.

Darmstadt, den 16.10.2023

Jonas Keller